Plasma Cascade in Kerr Black Hole Magnetospheres

By

Alexander L. Ford

Submitted to the Department of Physics and Astronomy and the
Faculty of the Graduate School of the University of Kansas
in partial fulfillment of the requirements for the degree of
Doctor of Philosophy

Mikhail V. Medvedev, Chairperson

Thomas E. Cravens

Committee members

Hume A. Feldman

Sergei F. Shandarin

David E. Lerner

Date defended: 06/15/2017

The Dissertation Committee for Alexander L. Ford certifies
that this is the approved version of the following dissertation :

Plasma Cascade in Kerr Black Hole Magnetospheres

Mikhail V. Medvedev, Chairperson

Date approved: 06/15/2017

Abstract

Electromagnetic, radiative, and plasma processes around black holes in active galaxies determine how relativistic jets are launched and the efficiency at which the black hole energy is extracted via the Blandford-Znajek mechanism, which converts the black hole rotational energy into Poynting flux. The crucial assumption is the force-free condition, which is the presence of plasma with a density at or above the Goldreich-Julian density. Unlike neutron stars, which in principle can supply electrons from their surface, black holes cannot supply plasma at all, they are only a sink. Therefore, the plasma needed must be generated *in situ*.

The essential process is the plasma production via an electron-position cascade in the so-called "gap" region in the force-free magnetosphere around the black hole. This multi-stage process, involving particle acceleration, photon Compton up-scattering, and production of electron-positron secondaries, is explored numerically by computing the radial development of the entire cascade.

It is shown how the electron-positron plasma production depends on the black hole mass and spin, the energy density of the ambient photons, and seed magnetic field strength. Presented is the full, two-dimensional structure of the gap, along with empirical scaling relations for the two-dimensional gap structure. Observational predictions for X-ray and γ-ray fluxes and spectra, which can be compared with observations of the inner regions near jets and

estimations of the structure of the gaps in several galaxies, e.g., Messier 87, using the empirical scaling relations are discussed.

Acknowledgements

This is the culmination of the better part of a decade of work. I would not have been able to do this without the support of so many people; too many to name here. I would first like to acknowledge my research advisor, Misha Medvedev. I cannot thank him enough for his guidance and patience throughout my time as a graduate student. Under his direction I have been fortunate enough to work on several incredibly interesting projects. I also want to thank my committee for their time and for their cooperation. I truly appreciate all of their help. My education at the University of Kansas was enriched by my fellow graduate students. Notably Brett Keenan, who deserves my gratitude for being a great colleague and a true friend. Serendipitously our intellectual interests aligned, both inside and outside of physics. Studying and working alongside him made me a better physicist. Of course, I am thankful for the astronomical amount of encouragement my entire family has given me, even though I'm sure they've questioned what exactly it is I do. I was born privileged with the unconditional support my parents, Dean and Donna Ford, give me. I am eternally grateful for their faith in me. Finally, a big thank you to all of my friends. Without them, I may not have kept my sanity. The friends I have made in graduate school have become my adopted family. Being able to lean on them for solace, encouragement, and humor enabled me to make it this far. At times, I have questioned the decision to pursue my doctorate, but I regret nothing. The personal growth, the lifelong friendships, and the stimulating academic research have all made this pilgrimage worthwhile.

Contents

List of Figures

List of Tables

Chapter 1

Introduction

A brief history of extragalactic astronomy begins in 1750 when Thomas Wright speculated that some nebulae were not part of the Milky Way galaxy, but independent galaxies (Wright, 1750). Wright's work was expanded upon by Kant five years later (Kant, 1755) and then ignored for the better part of a century. In 1842, François Arago brought Kant's work to astronomer's attention and the extragalactic hypothesis gained momentum in the scientific community (Beckmann & Shrader, 2012). In 1913, the first observational evidence supporting a nebula outside of the Milky Way was reported by Vesto Slipher. He observed redshifted lines moving relative to our galaxy at velocities exceeding the Milky Way's escape velocity (Slipher, 1913). Soon after more observations supporting extragalactic objects were published (Curtis, 1920; Hubble, 1926). Carl Seyfert discovered the first evidence for active nuclei in galaxies. He found spectra of six galaxies, showing high-excitation nuclear emission lines superposed on a star-like spectrum (Seyfert, 1943). He observed that a subset of galaxies showed broad emission lines, while another subset only had narrow emission lines. An early hypothesis was that a large number of stars would explain Seyfert's data. Over a decade later, Woltjer showed that the observed emissions concentred within the central 100 pc of the galaxy would require a mass on the order of $10^8 M_\odot$(Woltjer, 1959). Which led to the idea that at center of these galaxies there

is a very large mass onto which the surrounding disk of gas accretes; and further, the accretion is then what is primarily emitting (Hoyle & Fowler, 1963). Finally, in 1964, the idea of a black hole at the center of an AGN was proposed (Zel'dovich & Novikov, 1964; Salpeter, 1964).

1.1 Terms and Constants

Unless otherwise stated, all equations and expressions with be in cgs units. Here, a list of relevant physical quantities and definitions is provided for reference.

1.1.1 Lengths

- 1 AU $\approx 1.5\times10^{13}$cm = an astronomical unit, which is the distance between the earth and the sun.
- 1 pc = 2.06×10^{5}AU = 3.1×10^{18}cm = a parsec, which is the distance to a star with a parallax equal to one arc-second.

1.1.2 Time

- 1 year = 3×10^{7}s
- $H_0^{-1} \approx 1.4\times10^{10}$years = Hubble time, which is the approximate age of the universe.

1.1.3 Solar Units

- $M_\odot = 1.988\times10^{33}$g = mass of the sun.
- $L_\odot = 3.848\times10^{33}$ergs/s = luminosity of the sun.

1.1.4 Constants

Symbol	Numerical Value	Name
c	2.99792×10^{10}cm/s	speed of light
G	6.673×10^{-8} dyne cm^2/g^2	gravitational constant
h	6.62607×10^{-27}ergs s	Planck constant
e	4.803×10^{-10}g$^{1/2}$cm$^{3/2}$/s^2	elementary charge
m_e	9.109×10^{-28}g	mass of an electron (or positron)
m_p	1.3806×10^{-24}g	mass of a proton
σ_T	6.652×10^{-25}cm^2	Thomson cross-section
σ	5.67×10^{-5}ergs/(cm$^2K^4$s)	Stefan-Boltzman constant
k	1.3806×10^{-16}ergs/K	Boltzman constant
1eV	1.602×10^{-12}ergs	electron Volts

Table 1.1: A list of relevant and useful physical constants.

1.2 Research Overview

I think it is helpful to have a picture of the the destination before starting. There are a substantial amount of models to fit the observational data of active galactic nuclei (AGN). Of these models, the Blandford-Znajek mechanism to extract rotational energy from the black hole is ubiquitous. One assumption the Blandford-Znajek mechanism uses is that the environment near the black hole is plasma rich and force-free. This work examines a plasma cascade process, illustrated in Figure 1.1, that allows the environment around the black hole to become force-free. It is a natural outcome of the general relativistic environment of the magnetosphere around a spinning (Kerr) black hole.

There is a surface in the magnetosphere around a Kerr black hole that has the plasma

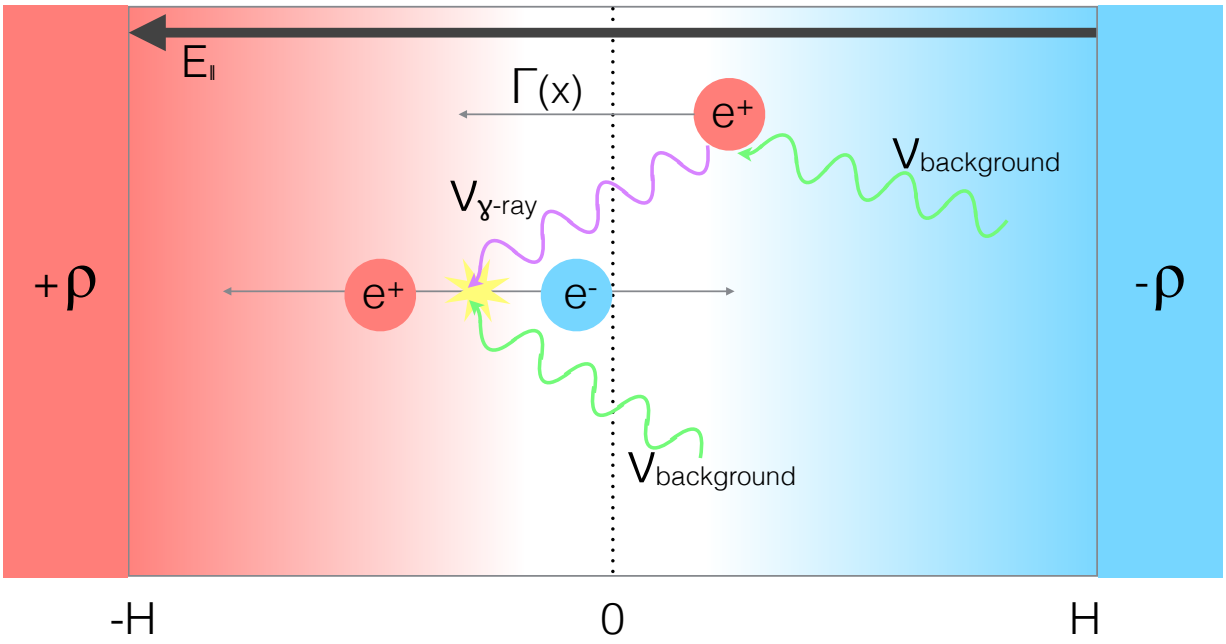

Figure 1.1: A toy model used to illustrate the cascade process inside of the gap region. In this example, a seed positron is accelerated by the electric field. The positron then inverse Compton scatters with a background photon. The up-scattered photon then pair produces with another background photon. This process continues until the magnetosphere is filled with plasma.

density needed for the magnetosphere to be force-free go to zero. This allows for an under-dense region (gap) to form. This gap will continue to grow unless a plasma production process inside of the gap stops its growth.

Once the gap forms, it has an electric field that is parallel to the magnetic field. Let there be only one charge in the gap, and it will be accelerated by the electric field. The charge then inverse Compton scatters with a background photon, possibly from the accretion disk. If enough energy was imparted to the up-scattered photon, it can pair produce with another background photon. This has taken the amount of charge in the gap from one to three, and these three charges are accelerated and continue the process until there is a sufficient amount of plasma for the electric field to be zero. At this point the plasma density is sufficient for the magnetosphere to be force-free.

Understanding the structure of the gap (electric field profile, outgoing photon flux,

peak Lorentz factor, etc.) allows for insight into how the interplay between the available background energy, black hole spin and mass, and ambient magnetic field effects the efficiency of energy extraction from the rotation of the black hole. The outgoing current density and photon flux also can be used with leptonic jet models and observations to put constraints on the environment around the black hole.

Chapter 2

Active Galactic Nuclei

Black holes are in the center of galaxies and, in particular, active galaxies. AGN turn gravitational energy (via accretion) and rotational energy (via the Blandford-Znajek process) into mechanical energy and Poynting flux. The emission from the accretion disk can be observed in some AGN; an example is the "Big Blue Bump" that is peaked in the UV and comes from thermal emission from the disk (Czerny & Elvis, 1987; Koratkar & Blaes, 1999). A model for the accretion disks around AGNs was developed by Shakura and Sunyaev in 1973. The model consists of a geometrically thin, optically thick disk (Shakura & Sunyaev, 1973) (for a detailed treatment of the accretion disk see Section 2.4). As observation capabilities has improved across the electromagnetic spectrum, many different objects have been observed that appear to have an active nucleus.

2.1 AGN Taxonomy

Radio galaxy is a all-encompassing term for bright radio sources. They are usually giant elliptical galaxies that are viewed edge on. The dusty torus may screen-out blackbody emission from the accretion disk, but is a strong synchrotron emitter (Peterson, 1997; Matsuda et al., 2011). The difference between subclasses of radio loud AGN, Fanaroff

Figure 2.1: NGC 4258 is a spiral galaxy approximately $2.5 \times 10^7 ly$ from Earth, it is also known as M106. This is a composite photo. The visible light is shown in gold, the infrared light is shown in red, the radio light is shown in purple, and X-ray is shown in blue. (Credit: X-ray: NASA/CXC/Univ. of Maryland/A.S. Wilson et al. Optical: Pal.Obs. DSS; IR: NASA/JPL-Caltech; VLA: NRAO/AUI/NSF).

and Riley Class I (FRI) and Fanaroff and Riley Class II (FRII), is that FRIs are low powered and FRII are high powered. FRI radio galaxies have radio emission that is concentrated at the core, i.e., brightness decreasing with distance from core. FRIs are core-dominated because the jet is slower and less powerful than FRII, and interacts more readily with the environment (Beckmann & Shrader, 2012). FRII radio galaxies are less abundant than than FRIs, but more luminous. FRII's jets are thousands of times more powerful than FRI's jets, so they travel through the surrounding medium and form giant radio lobes (Beckmann & Shrader, 2012). Their primary emission comes from hot spots and radio lobes (Rusinek et al., 2017). For FRI the X-ray emission from the kpc-jets can be explained as synchrotron emissions (Krawczynski & Treister, 2013). X-ray bright spots imply particle acceleration in the jet. FRII have a radio to X-ray spectrum that cannot be characterized with a single synchrotron component. Instead a synchrotron self-Compton model is needed.

Seyferts are spiral galaxies with strong nuclear emission. They look like a normal, distant spiral galaxies with a star superimposed in the center. Seyferts are distinguished spectroscopically by the presence of strong, high-ionization emission lines. Seyferts are usually less luminous and at lower redshift than quasars. The 'type' I or II classification used to distinguish low and high powered Fanaroff and Riley AGN is not the same as the 'type' applied to Seyfert galaxies. Type I AGN have broad-line emission, whereas Type II AGN have narrow-line emission (Peterson, 1997).

Quasi-stellar object (QSO) is a bright, distant AGN. They differ observationally from Seyferts in that the host galaxy is visually obscured. They have similar spectra to Seyferts, but the stellar absorption features are weak and the narrow-lines are weaker relative to the broad-lines (Peterson, 1997; Beckmann & Shrader, 2012).

Blazars are the most energetic class of AGN. They are AGN with relativistic jets pointed towards Earth, producing both synchrotron and inverse Compton γ-rays. They are extremely variable over short timescales (Aleksić et al., 2012). Blazars are sometimes sepa-

rated into two subtypes based on the strength of their emission lines, FSRQs (Flat Spectrum Radio Quasars) and BL Lac (BL Lacertae) objects. FRI and FRII jets can be are classified as blazars. FRIs are correlated with BL Lac objects and FRIIs with FSRQs (Fanaroff & Riley, 1974; Hogan et al., 2011). I found astrobites (`https://astrobites.org/guides/galaxy-and-agn-types/`) helpful in understanding the different AGN classifications.

2.1.1 Radio Loudness

AGN can be split into two distinct categories based on the radio emissions: radio loud and radio quiet. Radio loud AGN can produce jets. One question is what are the physical differences between radio loud and radio quiet AGN, and can this difference provide a mechanism for the launching of jets. Stawarz in 2010 studied difference in accretion rate and black hole mass between radio loud and radio quiet AGN. The results from the study are shown in Figures 2.2 and 2.3. The radio "loudness" parameter for both figures is

$$R \equiv L_{\nu R}/L_{\nu B} \simeq 10^5 (L_R/L_B) \tag{2.1}$$

where the 4400Å nuclear B-band luminosities are $L_B \equiv \nu_B L_{\nu B}$, assuming that the bolometric disk luminosities are on average related to the accretion luminosities by $L_{\rm acc} \simeq 10 \times L_B$ and $L_R \equiv \nu_R L_{\nu R}$ is the 5GHz total luminosities. The accretion rate parameter is

$$\lambda \equiv L_{\rm acc}/L_{\rm Edd} \tag{2.2}$$

where $L_{\rm Edd} \simeq 10^{38} (M_{\rm bh}/M_\odot)$ erg/s is the Eddington luminosity.

Figure 2.2 shows how radio "loudness" is related to accretion rates. One can see that the "loudness" increases with decreasing λ. There also seems to be a saturation at low accretion rates, $\lambda < 10^{-3}$. This anti-correlation with accretion rate trend is followed by both the radio loud and radio quiet sources. Figure 2.3 shows the radio "loudness" depen-

dence on black hole mass. It can be easily recognized that AGN with $M_{\rm bh} > 10^8 M_\odot$ reach values of " loudness" up to > 1000 times higher than AGN with $M_{bh} < 10^8 M_\odot$. This result seems to be in agreement with some previous studies (McLure & Jarvis, 2004); however, others report conflicting results (Ho, 2002; Urry & Woo, 2002).

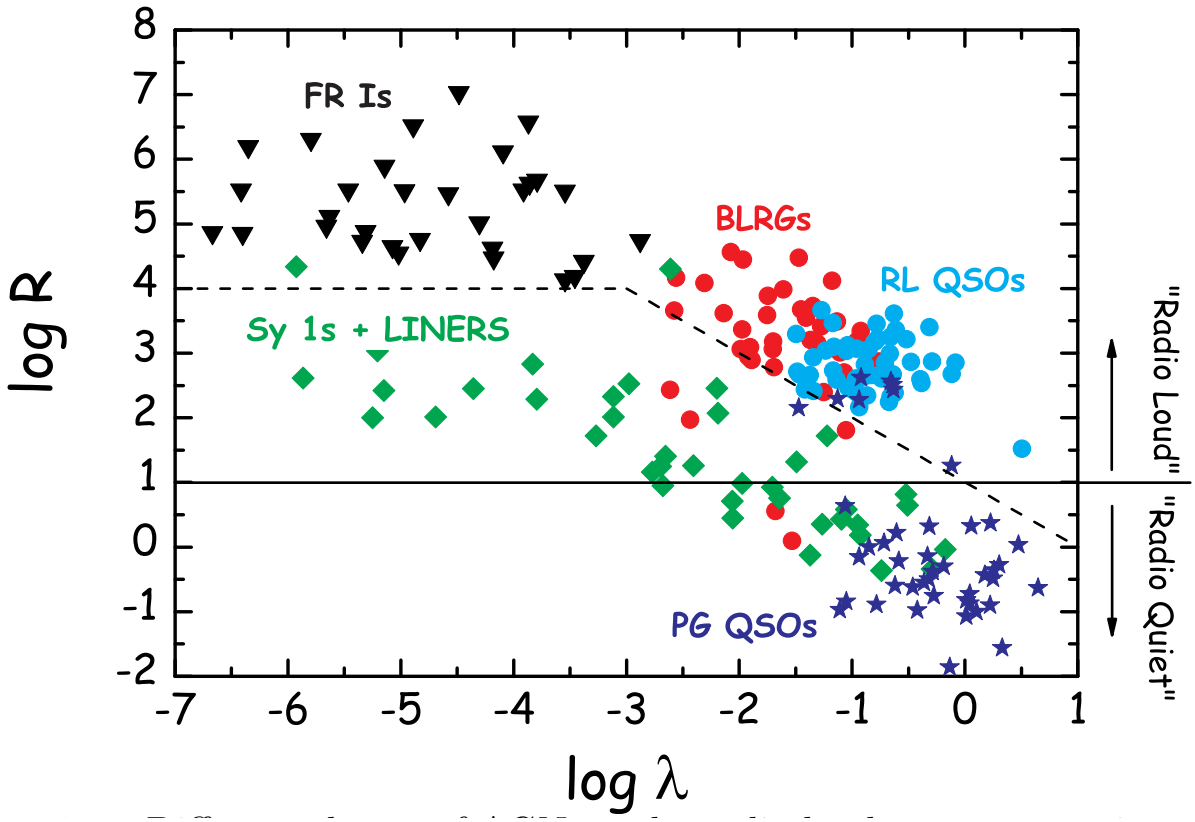

Figure 2.2: The dependance of the radio "loudness" parameter on the accretion rate. The dashed line indicates the separation between radio loud and radio quiet sources. This figure is from (Stawarz, 2010).

As will be shown in Chapter 7, large black hole masses will have a more efficient plasma cascade, thus allowing the Blandford-Znajek mechanism to extract energy from the rotation of the black hole. In the "spin paradigm," the black holes in AGN with "loudness," $R < 10$, are assumed to spin slowly ($a \leq 0.1$). In the AGN with $R > 10$, the black holes are assumed to spin rapidly ($a \simeq 1$) (Wilson & Colbert, 1995; Hughes & Blandford, 2003).

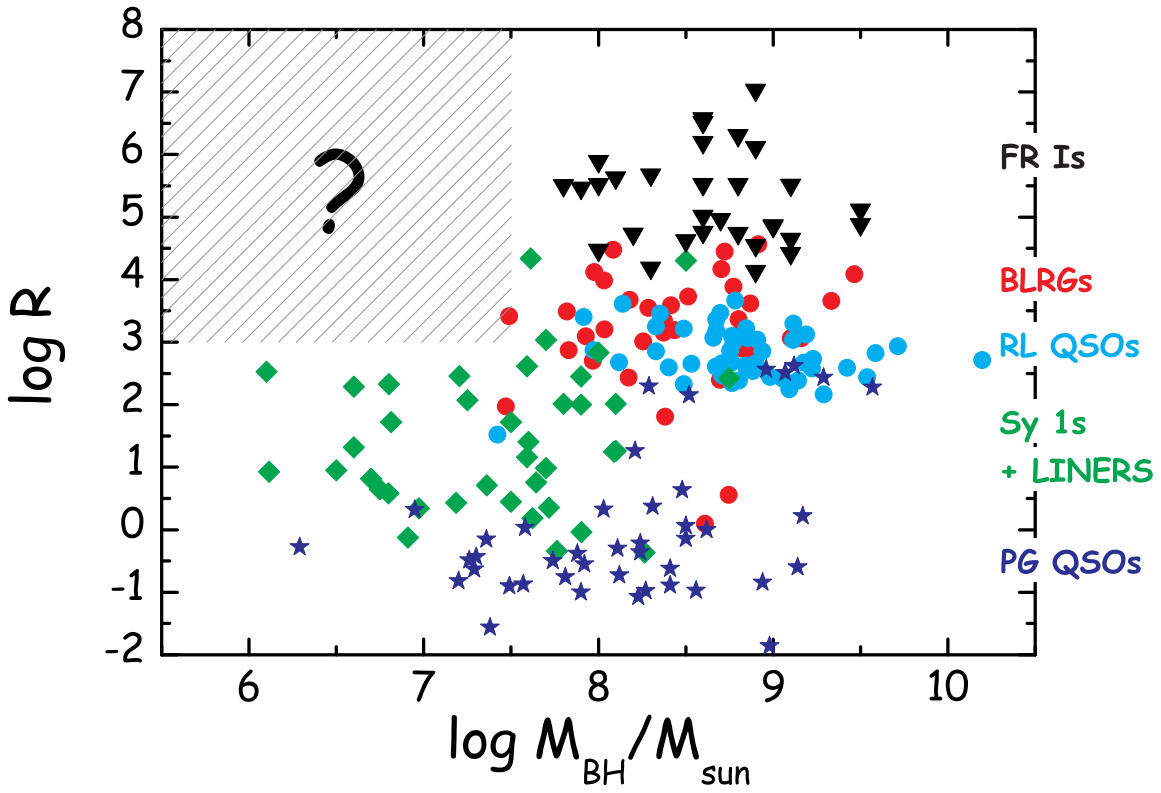

Figure 2.3: The dependance of the radio "loudness" parameter on the black hole mass. Where $M_{\rm sun} \equiv M_{\odot} = 1.988 \times 10^{33}$ g. This figure is from (Stawarz, 2010).

2.2 Emission from the Accretion Disk

AGN identification is done through piecing together their spectral energy distributions across the electromagnetic spectrum. One type of emission directly from the accretion disk is blackbody that forms the "Big Blue Bump" and it is peaked in the UV (Czerny & Elvis, 1987; Koratkar & Blaes, 1999). The accretion disk can be partially covered by a corona of hot, thermal material. Comptonization occurs in the hot corona and produces emissions that extend into the hard X-rays. There are alternative models for the observed X-ray emission. One is the "lamp-post model" where an X-ray source is illuminating the disk from above (Henri & Petrucci, 1997; Malzac et al., 1998). Other alternative models are hot inner disk flow (Ichimaru, 1977; Narayan et al., 2002) and a structured multilayer corona (Galeev et al., 1979). In the X-ray spectra of some AGN, there is a broad emission

line around ~ 6.4 keV (in the AGN frame). This line is from fluorescence Fe K-α emission of iron in the inner accretion disk. The iron is excited by hard X-rays (Fabian et al., 1989; Reynolds & Nowak, 2003; Ross & Fabian, 2007). The shape of the line is from gravitational redshift combined with a kinetic blue shift from the rotation of the disk. Analysis of the Fe K-α line in MCG 06-30-15 indicates a spin per unit mass of the black hole of $a > 0.987$ (Brenneman & Reynolds, 2006).

A representation of spectrum seen in different types of AGN is shown in Figure 2.2. Figure 2.5 shows a typical spectrum from a jet-disk model. Both of these figures can be compared to an actual spectrum shown of 3C 273 in Figure 2.6. 3C 273 is a great example of a double hump spectrum from the synchrotron emission at lower energies and inverse Compton at higher energies (see Figures 2.6 & 2.9).

AGN have narrow and broad emission from clouds of interstellar material orbiting the black hole at different distances (Véron-Cetty & Véron, 2000). In low-density regions around AGN, $n_e \sim 10^3$ cm^{-3}, the emission-line spectra have narrow-lines. These narrow-lines have Doppler widths around 500 km/s and an ionization parameter on the order $U(H) \sim 10^{-2}$. The NLR can be optically thin for the hydrogen Lyman continuum. Some prominent optical emission lines are [O III] and Hα+[N II]. The NLR are located at distances on the order of 100 parsecs ($\sim 300ly$) from the black hole. The BRL are at distances on the order of $10ly$ ($\sim$ 3 parsecs) from the black hole. In high-density regions around AGN, $n_e > 10^9$ cm^{-3}, the emission-line spectra have broad-lines. These broad-lines have Doppler widths from 1000 km/s to 25000 km/s, and the ionization parameter is similar to the NRL. There are strong lines of [H I], [Mg II], and [Fe II]. Observations of the BRL emission combined with the emission for the disk can be used to estimate the mass of the black hole based on reverberation mapping (Peterson, 2007; Kaspi et al., 2007). Reverberation mapping uses the widths of the BLR lines to find a constraint on the orbital velocities of the clouds near the black hole. This information is then combined with measured lag times between variation of the continuum flux from the accretion disk and the

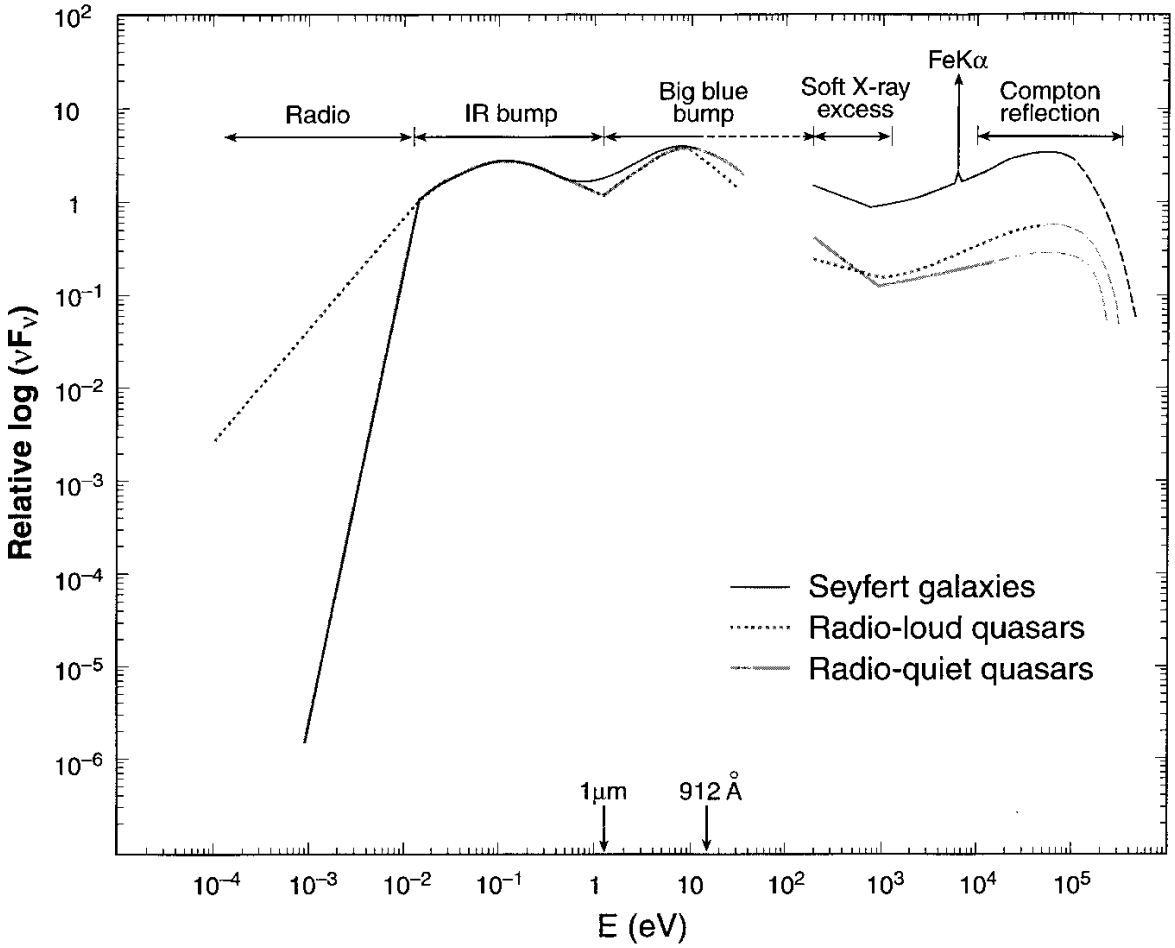

Figure 2.4: Representation of the broadband continuum spectral energy distribution seen in the different types of AGN. The radio quiet spectrum can be divided into three major components: the infrared bump, which comes from reprocessing of the UV emission by dust; the Big Blue Bump, which is due to the accretion disk; and the X-ray region, which is a Comptonized power law. This figure is from (Koratkar & Blaes, 1999)

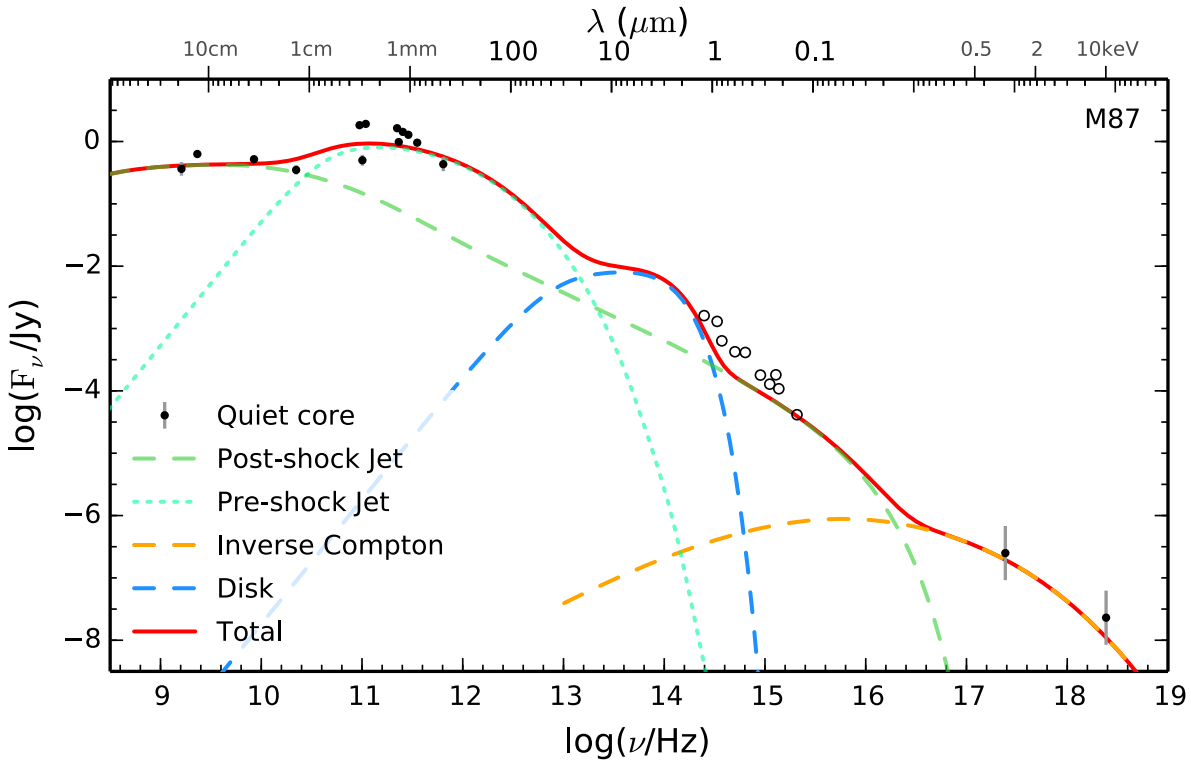

Figure 2.5: A jet–disk model for spectral energy distributions that is a fit of the Chandra data. For illustrative purposes, the ALMA (Atacama Large Millimeter/submillimeter Array) data is added. This shows that the emission from the highest ALMA frequencies reaches similar levels as the VLBI (Very-long-baseline interferometry) data at 1.2 mm, illustrating the transition from the optically thin to the optically thick region in the jet. This figure is from (Prieto & Fernández-Ontiveros, 2016).

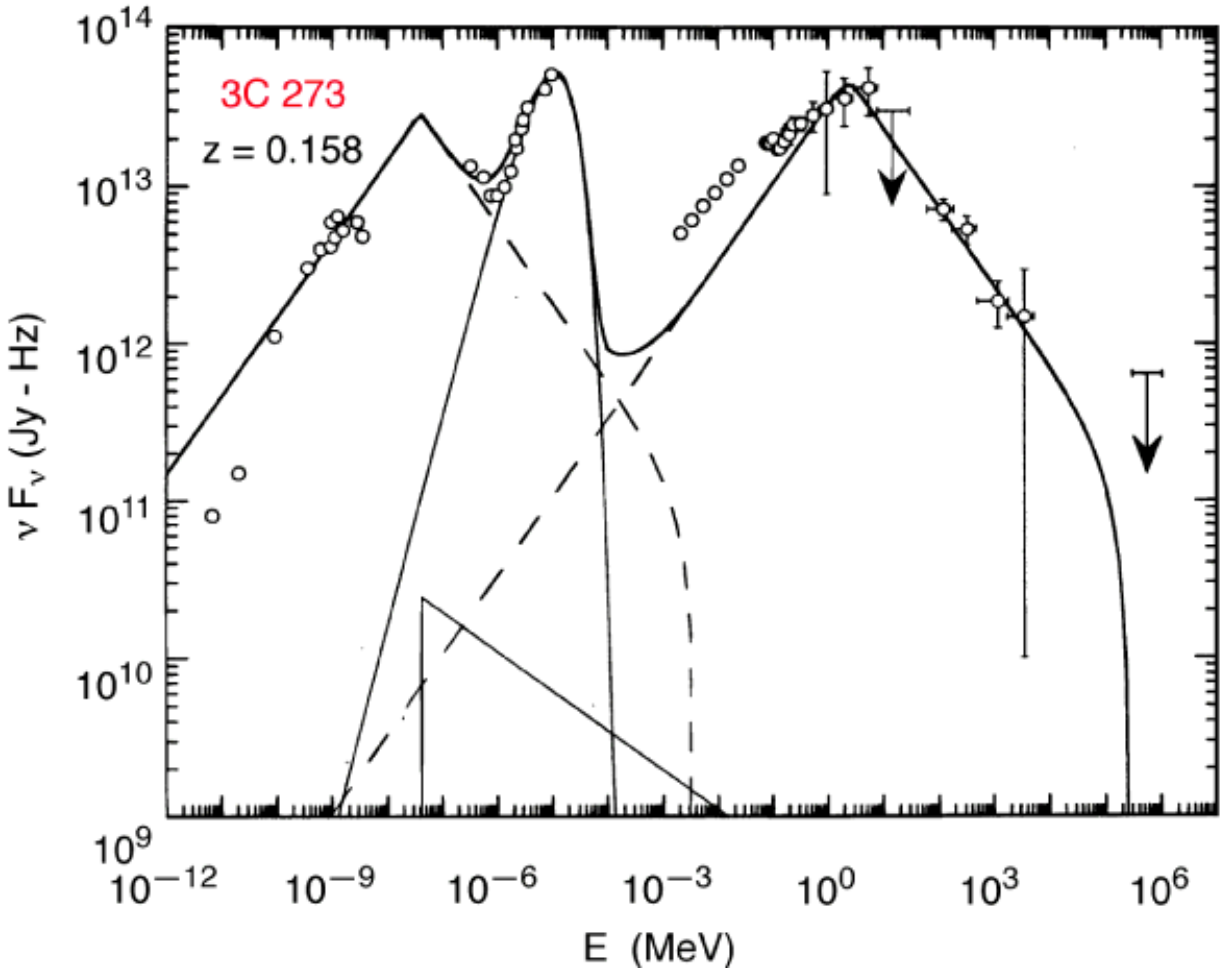

Figure 2.6: The spectrum from 3C 273. One can see synchrotron emission at lower energies and inverse Compton at higher energies. Credit: NASA via M.A. Catanese (Iowa State University).

BLR flux. The BLR emission comes from reprocessing the continuum flux from the disk; therefore the lag time can be used to estimate the distance of the BLR clouds from the black hole. The distance from the black hole and the orbital velocity of the clouds that make up the BLR are used to estimate the black hole mass.

2.3 Jets

The term jet was first applied to an astronomical object in 1954 (Baade & Minkowski, 1954) to the "protrusion" out of the core of the nearby galaxy M87. Astrophysical jets are collimated, supersonic flows of plasma accelerated by compact objects. When astrophysical jets have ionized matter moving close to c, they are called relativistic jets. Jets are observed perpendicular to some AGN. The composition of jets is uncertain due to the dominance of non-thermal continuum emission from the jets which leads to a lack of detectable lines. The energy and momentum of jets is initially dominated by Poynting flux. At larger distances the electromagnetic energy is transferred to the particles. The environment directly around the black hole at the center of AGNs is highly magnetized. Therefore, unless the plasma is highly collisional, the plasma supply to the inner jet cannot come from the accretion disk. The energy fueling the jet and the initial plasma supply for the jet have to be powered by the supermassive black hole. Electrons inside of the jet emit low-energy synchrotron emission and high-energy inverse-Compton emission. The high-energy emission can come from synchrotron self-Compton or external inverse Compton emission. The photons for the eternal inverse Compton process can come from the BLR, thermal photons from the disk, or even the cosmic microwave background.

The jet is launched by the combined effect of thermal pressure, centrifugal forces, and the Blandford-Znajek process. The Blandford-Znajek process involves the conversion

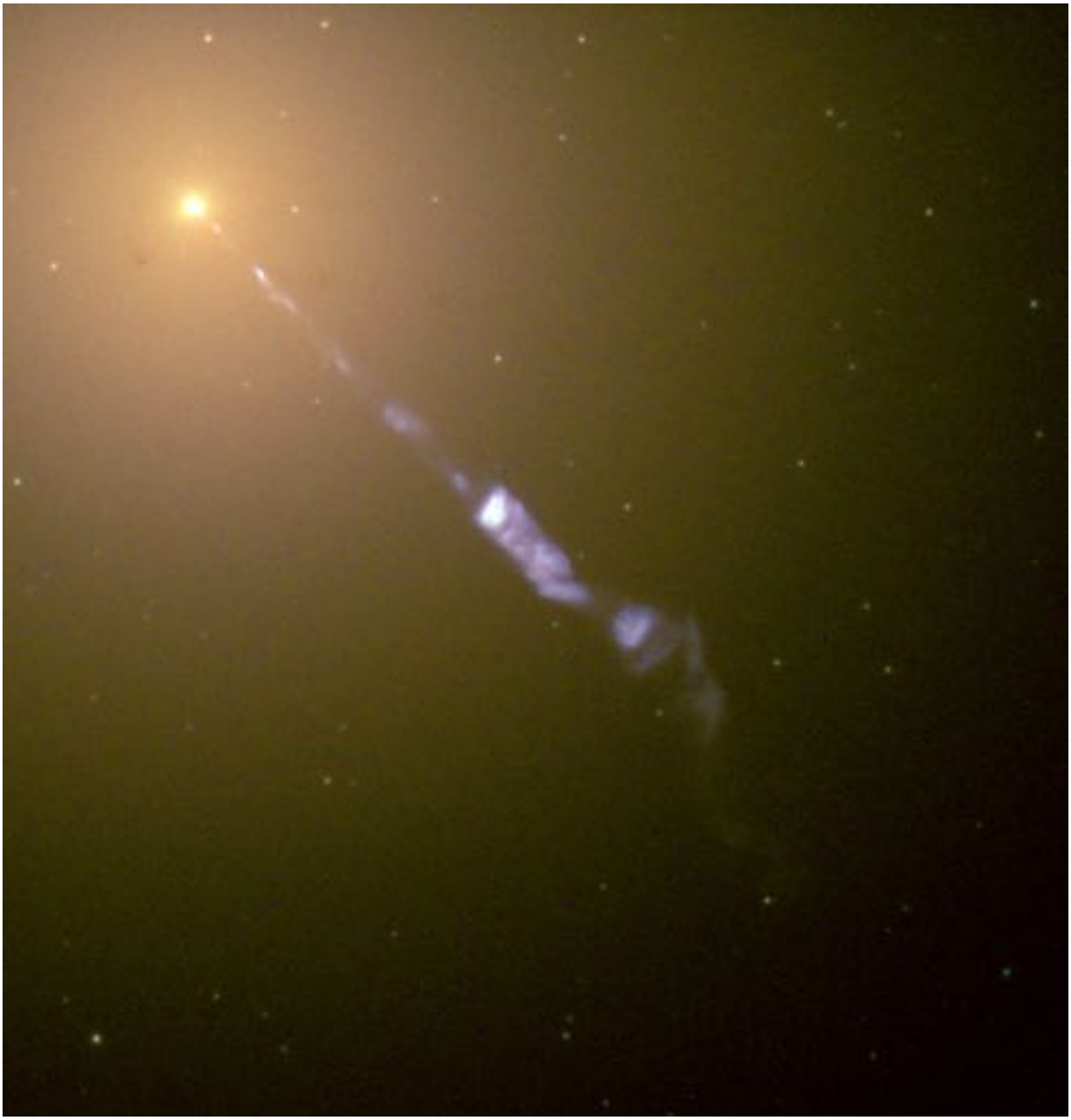

Figure 2.7: M87: An elliptical galaxy about $6\times10^7 ly$ from Earth, also known as NGC 4486. M87 is one of the nearest and is the most well studied relativistic jets. This figure is from NASA and The Hubble Heritage Team (STScI/AURA).

of rotational energy (Blandford & Znajek, 1977). Blandford and Payne in 1982 proposed a jet launching model that showed a jet can be launched magneto-centrifugally from the surface of an accretion disk (Blandford & Payne, 1982). In some jets, "knots" can be observed. The origin of the knots is not fully understood, but many believe they arise from MHD instabilities and shocks. The appearance of "superluminal motion" of knots is a consequence of the jet being relativistic. The knots, of course, are not moving with a velocity greater than c; they appear to due to geometrical effects, see Figure 2.8. The knots in the jet emit light via synchrotron and inverse-Compton so one can think of the knot as a source of light at location A and at location B. The knot is moving with velocity $v_{\circledast}$ at an angle $\theta_{\circledast}$ with respect to the observer. Let the time it takes for the knot to travel between A and B be unity and $\beta_{\circledast} \equiv v_{\circledast}/c$. Then the transverse speed of the knot that is observed is

$$v_{\text{observer}} = \frac{v_{\circledast} \sin\theta_{\circledast}}{1 - \beta_{\circledast} \cos\theta_{\circledast}} \tag{2.3}$$

As an example, letting $\theta_{\circledast} = \pi/12$ yields a $v_{\text{observer}} = c$ for $v_{\circledast} \approx 0.82c$.

There are different jet models to explain observations of variable high-energy (TeV) emissions. These models can be split into two different categories: leptonic models and hadronic jet models. One model for producing TeV emission in jets is via synchrotron self-Compton radiation from relativistically moving plasma blobs (Georganopoulos & Kazanas, 2003). This model has the upstream energetic electrons interact with the synchrotron seed photons produced in the deceleration of blobs (Levinson, 2007). This occurs when multiple emission zones with changing line-of-sight directions mini-blob models. Another model is the jets-in-a-jet or jet-to-counterjet for the TeV flares (Giannios et al., 2010; Kovalev et al., 2007). This occurs when there is radial jet stratification and a fast inner core and slower outer layer. The final leptonic model that I will discuss has many similarities to the first hadronic model that will be discussed. This leptonic model has synchrotron emission from electrons produced in the inner regions of the jet that provide photons to produce inverse Compton emission from the fastest electrons

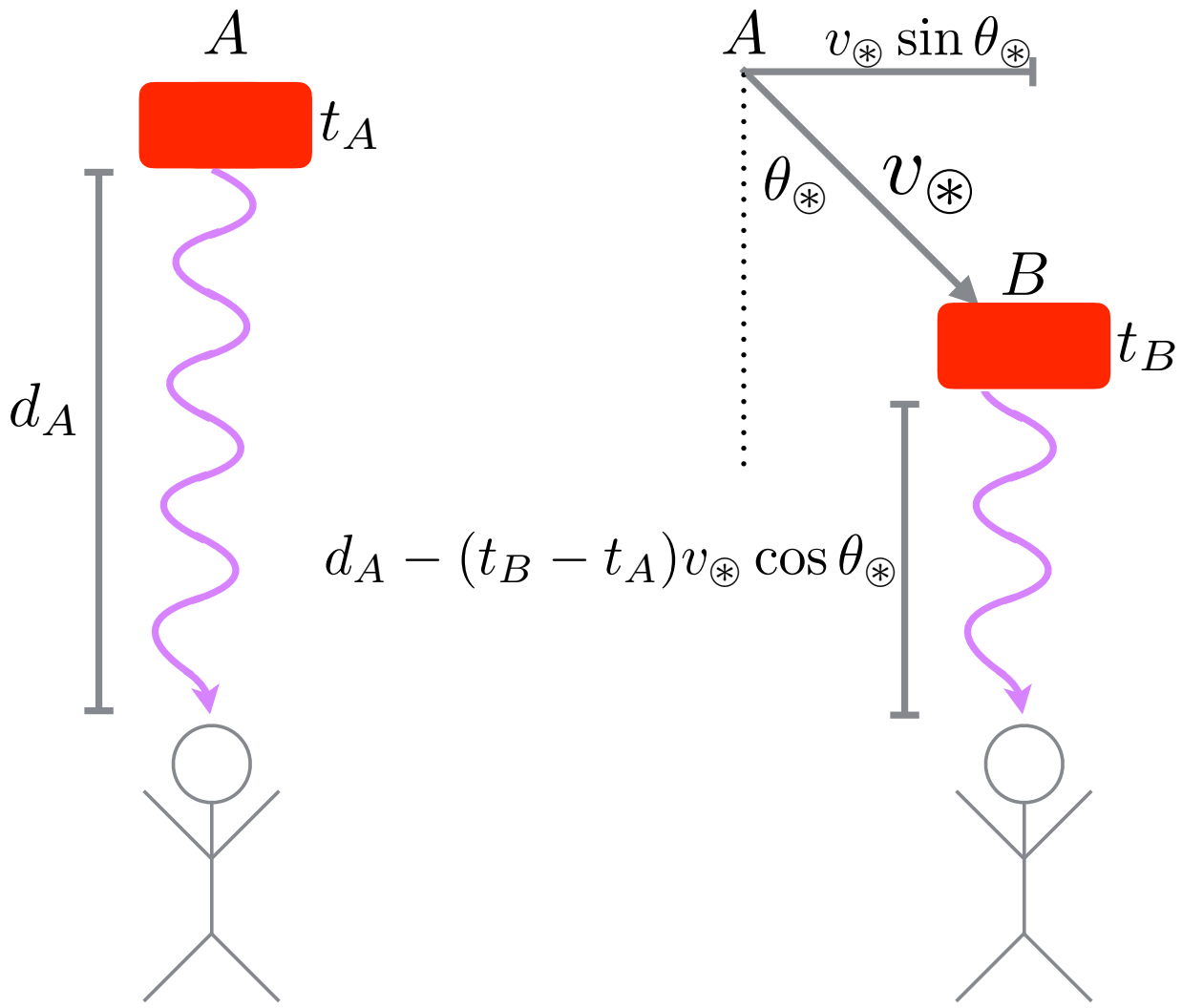

$$\Delta t_{\text{observer}} = 1 - (t_B - t_A)\beta_\circledast \cos\theta_\circledast$$

Figure 2.8: The red rectangle represents the knot inside at the jet moving at a velocity $v_\circledast$ at an angle $\theta_\circledast$ with respect to the observer who is represented by the stick figure. The knot is at position A at time t_A in the knot's reference frame and then the knot is at the position B at time t_B in the knot's reference frame.

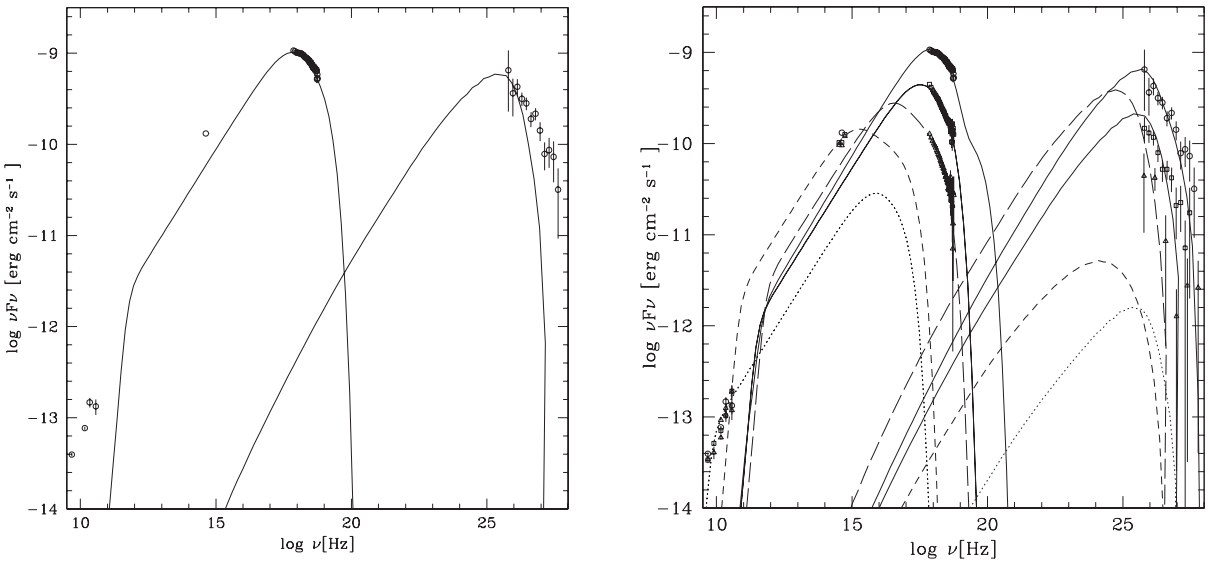

Figure 2.9:
Left: Spectral energy distribution of Mrk 421. The solid line shows the best fit to the data with a one-zone synchrotron self-Compton model.
Right: Spectral energy distributions of Mrk 421 at different X-ray fluxes: low (triangles), medium (squares), and high (circles). Fits to the SEDs with a multizone synchrotron self-Compton model are also shown, with a long-dashed line for the low-flux group and a solid line for both the medium-flux and high-flux groups. This figure is from (Błażejowski et al., 2005).

in the jet. The electrons of the upstream (faster flow) upscatter the low-energy photons produced in the slower, downstream part of the flow, i.e. the TeV emission in the jet is inverse Compton emission from the base of the jet (Perlman & Kazanas, 2005). One hadronic jet model uses proton synchrotron emission to dominate the photon supply for inverse Compton emission. These models are sometimes referred to as synchrotron-proton blazar models (Reimer et al., 2004). Another jet model that involves hadrons uses emissions from proton-proton collisions (Barkov et al., 2010). In order to have the needed proton density, a star or dense gas cloud needs to penetrate the jet on the scale of tens of black hole radii (Rieger & Aharonian, 2012). Protons are approximately 2000 times heavier than electron; therefore their magnetic deflection is minimal along with their synchrotron losses. Protons can interact with the background photon field and produce pions.

$$\begin{aligned} p + \gamma &\rightarrow p + \pi^0 \\ p + \gamma &\rightarrow p + \pi^{\pm} \end{aligned} \tag{2.4}$$

The neutral pions decay into γ-rays; and the charged pions produce electron-positron pairs.

$$\pi^{\pm} \rightarrow \mu^{\pm} \rightarrow e^{\pm} \tag{2.5}$$

At very large energies, there is a cutoff that can be attributed to several different mechanisms. There could be absorption near the γ-ray source; or there could be absorption in intergalactic space by background IR radiation fields (Dermer & Schlickeiser, 1994; Mucke & Protheroe, 2001). Figure 2.10 is an example of these cutoff energies for Markarian 421.

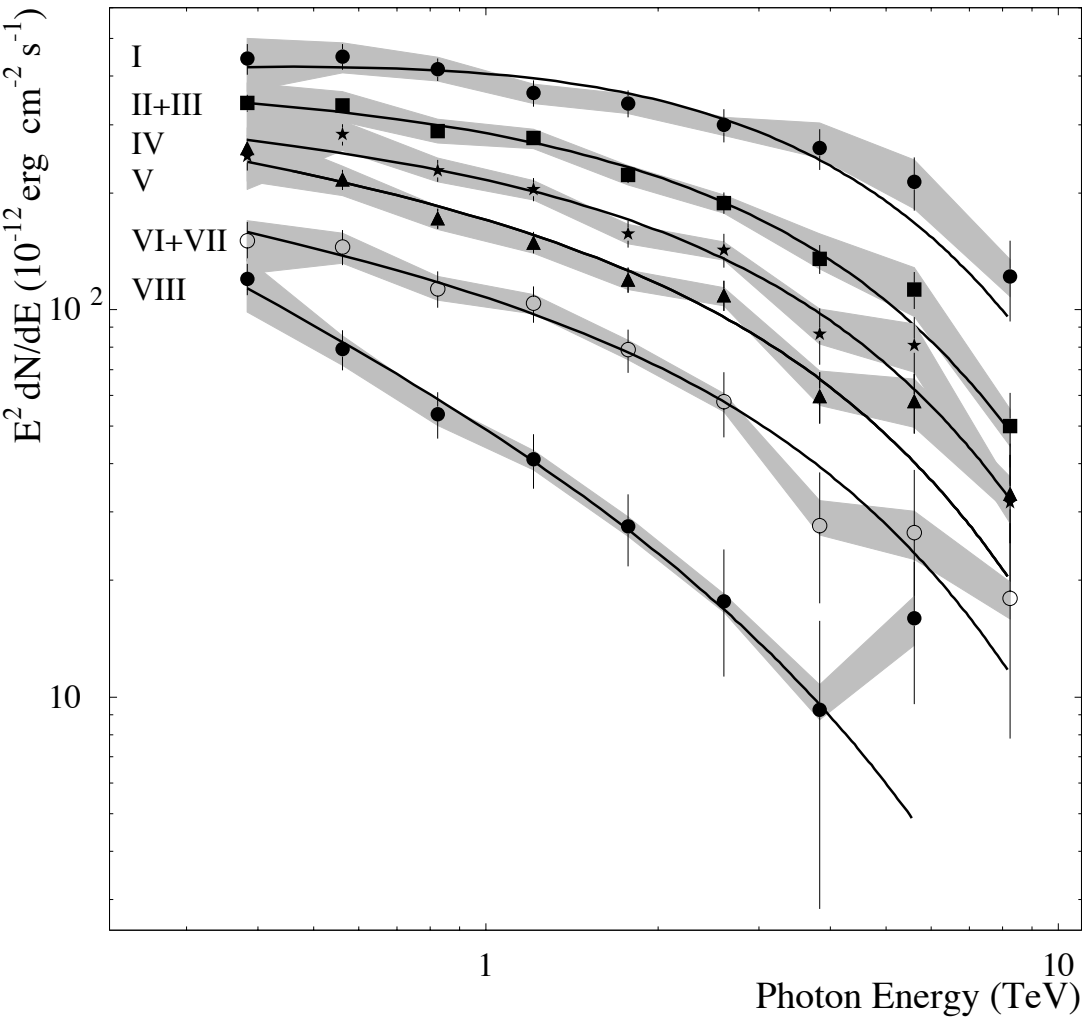

Figure 2.10: Mrk 421 spectra at different flux levels averaged for data from 2000-2001. The spectra have been fit by a power law with a fixed exponential cutoff at 4.3 TeV. The shaded areas indicate the systematic errors on the flux measurements. This figure is from (Krennrich et al., 2002).

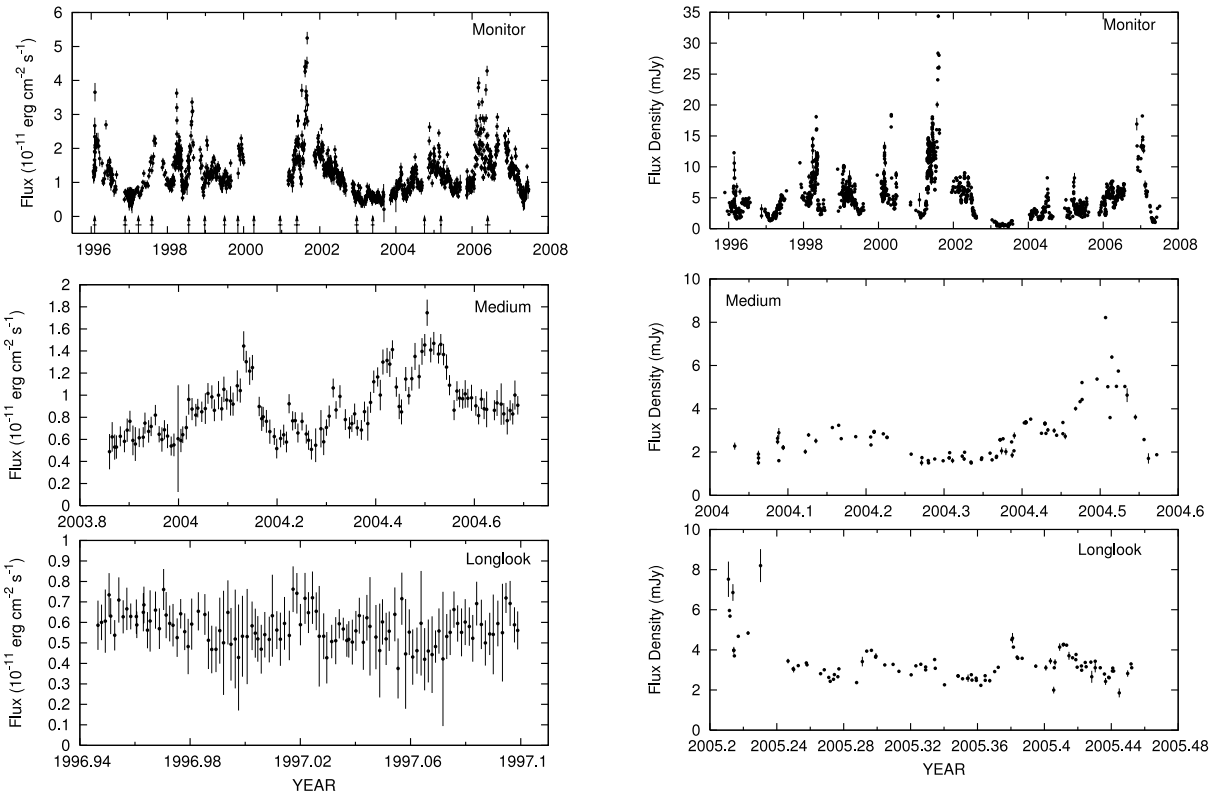

Figure 2.11: Left: X-ray data on different timescales for 3C 279. In the top panel, the arrows show the times of superluminal ejections, and the line segments perpendicular to the arrows show the uncertainties in the times of ejection.
Right: Optical (R-band) data on different timescales for 3C 279. This figure is from (Chatterjee et al., 2008).

Variability in jet emission is useful to constrain the size of the emitting region. Let R be the size of the emitting region and the minimum variability time-scale be $t_{\rm min}$.

$$R < ct_{\rm min}(\Gamma(1-\beta\cos\theta)(1+z))^{-1} \tag{2.6}$$

where z is redshift, Γ is the bulk Lorentz factor in the jet, and θ the angle of the jet with respect to the line of sight. Calculating the size of the emitting region allows one to evaluate at which distance from the central black hole the jet originates. Figures 2.11 and 2.12 show the variability of 3C 279 which has an estimated emitting region of light days and > 0.1 pc from the black hole (Hayashida et al., 2015).

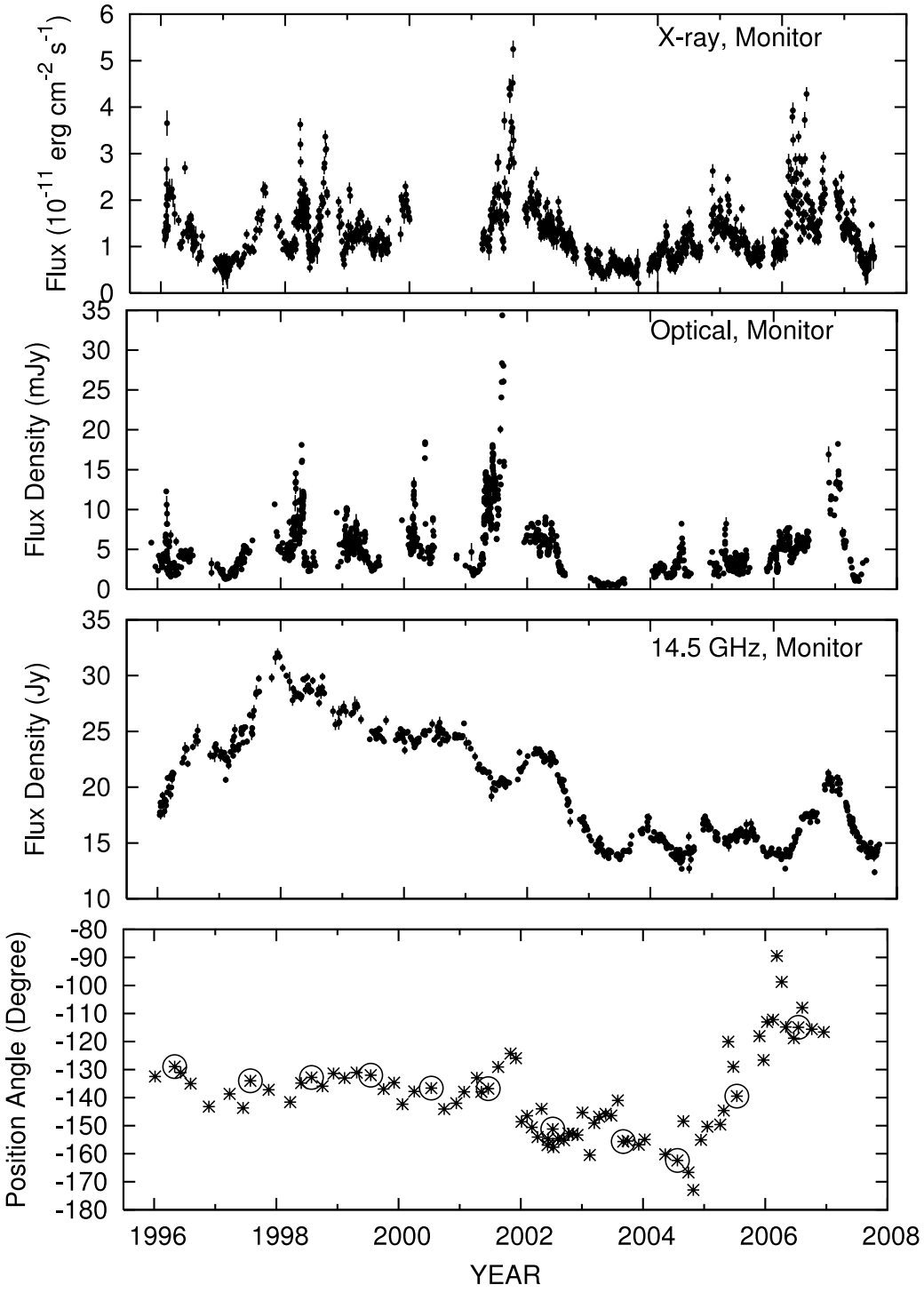

Figure 2.12: Variation of X-ray flux, optical flux, radio flux, and position angle of the jet from 1996 to 2008 for 3C 279. The circled data points in the bottom panel are the epochs shown. This figure is from (Chatterjee et al., 2008).

2.3.1 Synchrotron Radiation

Charged particles accelerated by a magnetic field will radiate. If those particles are moving non-relativisticly the radiation is cyclotron radiation and if they are moving relativisticly it is synchrotron radiation. Charge particles gyrate around the magnetic field lines with a frequency

$$\omega_B = \frac{qB}{\Gamma mc}, \tag{2.7}$$

where Γ is the Lorentz factor of the charge. The acceleration is perpendicular to the velocity, so the total emitted radiation is (Rybicki & Lightman, 1979)

$$\begin{aligned} P &= \frac{2q^2}{3c^3}\Gamma^4 \frac{q^2B^2}{\Gamma^2 m^2 c^2} v_\perp^2 \\ &= \frac{2}{3} r_e^2 c \beta_\perp^2 \Gamma^2 B^2, \end{aligned} \tag{2.8}$$

where $r_e = q^2/(m_e c^2)$ is the classical electron radius. Let α be the angle between the field lines and the velocity of the charge, which is called the pitch angle. Now averaging over all angles for a given β

$$\langle \beta_\perp^2 \rangle = \frac{\beta^2}{4\pi} \int \sin^2\alpha \, d\Omega = \frac{2\beta^2}{3}. \tag{2.9}$$

The power radiated can be expressed as

$$P = \frac{4}{3}\sigma_T c \beta^2 \Gamma^2 \mathscr{B}, \tag{2.10}$$

where the Thomson cross section, $\sigma_T = 8\pi r_e^2/3$ and the magnetic energy density is $\mathscr{B} = B^2/(8\pi)$.

2.4 Accretion Disk

At the most basic level, active galactic nuclei are systems defined by black hole accretion. In order to understand the different aspects of AGN, it is necessary to understand the physics of the accretion disk.

Assume a Newtonian accretion disk around a black hole of mass M with a constant accretion rate of $\dot{M}$. The angular momentum, l, of a ring orbiting the black hole at radius r with a mass m is

$$l = mrv_\phi. \tag{2.11}$$

The azimuthal velocity of the ring, v_ϕ, is related to the angular velocity, Ω, by

$$v_\phi = r\Omega = \sqrt{\frac{GM}{r}}. \tag{2.12}$$

Assume the disk thickness is $2h$ and define the surface mass density Σ to be

$$\Sigma = \int_{-h}^{h} \rho dz = 2h\rho, \tag{2.13}$$

where z is the height perpendicular to the disk and ρ is the density measured at $z = 0$. The rate at which the angular momentum is removed from the disk is

$$\dot{J} = \dot{M}\sqrt{GMr}. \tag{2.14}$$

This is the torque between two adjacent rings. For steady-state, $\dot{J} = \dot{M}\sqrt{GMr_{\text{disk}}}$, where r_{disk} is the radius of the disk. Likewise, the accretion rate for a steady-state is

$$\dot{M} = 2\pi r\Sigma v_r. \tag{2.15}$$

Now defining f_ϕ to be the viscous stress in the ϕ direction by a ring at r on a ring at $r\,dr$,

$$f_\phi = 3\eta\Omega/2 = \frac{3\eta}{2}\sqrt{\frac{GM}{r^3}}, \tag{2.16}$$

where η is the coefficient of dynamic viscosity. Turning our attention to conservation of angular momentum. Let $\dot{J}^-$ be the rate at which the black hole takes in angular momentum and $\dot{J}^+$ be the rate of angular momentum transport across radius r.

$$\begin{aligned} \dot{J}^+ &= \dot{M}\sqrt{GMr}, \\ \dot{J}^- &= \dot{M}\sqrt{GMr_{\text{inner}}}, \end{aligned} \tag{2.17}$$

where r_{inner} is the innermost orbital of the disk (Section 11.1 provides a discussion on the innermost stable circular orbit for Kerr black holes). Angular momentum conservation requires that the net torque exerted equal the net rate of change of angular momentum. The viscous stress, f_ϕ, is the force per area, which can be easily expressed as torque.

$$4\pi f_\phi r^2 h = \dot{M}\sqrt{GM(r - r_{\text{inner}})}. \tag{2.18}$$

Equation 2.18 assumes the black hole perfectly consumes the angular momentum. For the non-ideal situation, $\dot{J}^- = \beta\dot{M}\sqrt{GMr_{\text{inner}}}$, where $\beta \leq 1$. The coefficient of dynamic viscosity in turbulent motion is

$$\eta \sim \rho v_{\text{turb}} \iota_{\text{turb}}, \tag{2.19}$$

where v_{turb} is the characteristic velocity of the turbulence and ι_{turb} is the characteristic size of the turbulence. Assume $v_{\text{turb}} < c_s$ and $\iota_{\text{turb}} < h$, where c_s is the speed of sound. Rewriting f_ϕ (Netzer, 2006),

$$f_\phi = 3\rho v_{\text{turb}} \iota_{\text{turb}} \Omega/2 < 3\rho c_s h \Omega/2. \tag{2.20}$$

Now expressing the viscous stress in terms of pressure P

$$f_\phi = \alpha P, \tag{2.21}$$

where α is a nondimensional viscosity parameter and $0 \leq \alpha \leq 1$. This definition of f_ϕ is referred to as "α-disk models".

2.4.1 Energy Conservation

Now turning to energy conservation. The energy released is determined by the work done by the torque and the loss of gravitational energy. This energy loss is radiated away. The change in energy due to torque is

$$d(L_j) = d(\dot{J}\Omega) = d(GM\dot{M}/r), \tag{2.22}$$

and the change in energy due to gravitational loss is

$$d(L_{\text{grav}}) = d(GM\dot{M}/(2r). \tag{2.23}$$

Combining Equations 2.22 and 2.23 and differentiating yields

$$\frac{dL}{dr} = \frac{3GM\dot{M}}{2r^2}\left\{1 - \sqrt{\frac{r_{\text{inner}}}{r}}\right\}. \tag{2.24}$$

The non-relativistic limit of the total power radiated is

$$L = \frac{GM\dot{M}}{2r_{\text{inner}}}. \tag{2.25}$$

The emissivity per unit area from the top and bottom faces of the disk is

$$F(r) = \frac{3GM\dot{M}}{8\pi r^3}\left\{1-\sqrt{\frac{r_{\text{inner}}}{r}}\right\}. \tag{2.26}$$

Now assuming the disk is a blackbody, $F(r) = \sigma T^4$, where

$$T(r) = \left(\frac{3GM\dot{M}}{8\sigma\pi r^3}\left\{1-\sqrt{\frac{r_{\text{inner}}}{r}}\right\}\right)^{1/4}, \tag{2.27}$$

σ is the Stephan-Boltzmann constant, and T is temperature. Each ring emits its own blackbody leading to a multicolor blackbody spectrum.

2.4.2 Disk Geometry

Assume that in the accretion disk there is no net motion in the vertical direction. This allows one to equate the vertical gravitational force and the vertical pressure gradient, i.e., vertical momentum conservation.

$$\frac{dP}{dz} = -\frac{\rho GMz}{r^3} = -\rho\Omega^2 z. \tag{2.28}$$

Now assume the pressure is dominated by the gas pressure, $P_{\text{gas}} = \rho c_s^2$, then

$$\frac{dP}{dz} = c_s^2\frac{d\rho}{dz} = -\rho\Omega^2 z. \tag{2.29}$$

A solution for ρ is

$$\rho = \rho_0 e^{-z^2/h^2}, \tag{2.30}$$

where ρ_0 is the value of ρ at $z = 0$.

$$\frac{dP}{dz} = -\frac{2c_s^2\rho_0 z}{h^2}e^{-z^2/h^2} = -\frac{2c_s^2\rho z}{h^2} = -\rho\Omega^2 z. \tag{2.31}$$

Therefore, for a thin disk,

$$h \simeq \frac{c_s}{\Omega} = \frac{c_s}{v_\phi / r}, \qquad \frac{h}{r} \simeq \frac{c_s}{v_\phi} \ll 1. \tag{2.32}$$

This sets the scale for which disk thicknesses this thin disk model is applicable.

2.4.3 Radiation Transport

A source of photon absorption in the disk is bremsstrahlung (or "free-free" transitions). Other sources may be "bound-bound" line transitions and photoionization (or "bound-free" transitions). Take the frequency-averaged, Rosseland mean absorption opacity to be $\bar{\kappa}_{\rm abs}$. The Rosseland mean opacity is (Shapiro & Teukolsky, 1983),

$$\frac{1}{\kappa} \equiv \frac{\int_0^\infty \kappa_\nu^{-1} (d\epsilon_\nu^P / dT) d\nu}{\int_0^\infty (d\epsilon_\nu^P / dT) d\nu}, \qquad \epsilon_\nu^P = \frac{8\pi h \nu^3}{c^3} \left[e^{\frac{h\nu}{kT}} - 1 \right]^{-1}, \tag{2.33}$$

where ν is the frequency, κ_ν is the absorption opacity at a particular frequency, and T is temperature. ϵ_ν^P is the specific energy density, and the P signifies the Planck function. The Rosseland mean opacity for "free-free" absorption is

$$\bar{\kappa}_{\rm ff} = (6.45 \times 10^{22}) \frac{f_e f_i Z^2}{A} \bar{g}_{\rm ff} \rho T^{-3.5} [cm^2/g], \tag{2.34}$$

where A is the atomic weight, Z is the charge of the ions, $\bar{g}_{\rm ff}$ is the frequency averaged Gaunt factor for free-free transitions, and f_e and f_i are the fraction of electrons and ions, respectively (Shapiro & Teukolsky, 1983). The Rosseland mean opacity for "bound-free"

absorption is

$$\bar{\kappa}_{\rm bf} = (4.34\times10^{25})\bar{g}_{\rm bf}H(1+X)\rho T^{-3.5}[cm^2/g], \tag{2.35}$$

where X represents the mass fraction of hydrogen, H represents the mass fraction of heavy elements (Li and heavier), and $\bar{g}_{\rm bf}$ is the frequency averaged Gaunt factor for bound-free transitions (Shapiro & Teukolsky, 1983).

The main source of photon scattering is Thomson scattering,

$$\begin{aligned} \bar{\kappa}_{\rm scat} &= \frac{\sigma_T n_e}{\rho} = 0.4 f_e [cm^2/g], \\ \sigma_T &= \frac{8\pi}{3}\left(\frac{e^2}{m_e c^2}\right)^2, \end{aligned} \tag{2.36}$$

where σ_T is the Thomson cross-section, n_e is the free electron density, and f_e (as stated above) is the number of electrons per baryon. The total Rosseland mean opacity is

$$\bar{\kappa}^{-1}(\rho, T) = \bar{\kappa}^{-1}_{\rm scat} + \bar{\kappa}^{-1}_{\rm abs}. \tag{2.37}$$

Using this opacity, we can express the optical depth as

$$\tau = \int_0^h \bar{\kappa}\rho dz \approx \bar{\kappa}(\rho, T)\Sigma, \tag{2.38}$$

where Σ maintains its definition from Equation 2.13. For the vertical photon flux,

$$F(r, z) = -\frac{c}{3}\frac{d(aT^4)}{d\tau}, \tag{2.39}$$

where $a = 4\sigma/c$, and σ is the Stephan-Boltzmann constant. Using finite differences for the differential,

$$F(r) \approx \frac{acT^4}{\bar{\kappa}\Sigma}. \tag{2.40}$$

Equation 2.40 yields the surface photon flux for $\tau > 1$, optically thick disks. For optically

thin disks, the function for the photon flux becomes

$$F(r) \approx h\Lambda(\rho, T), \tag{2.41}$$

where Λ is the emissivity in the disk. The thin disk region of the disk is dominated by thermal bremsstrahlung and Comptonization.

2.5 Spectrum of a Thin Disk Model

The accretion disk can be divided into three regions of varying r: inner, middle, and outer (Shapiro & Teukolsky, 1983). In the outer region gas pressure dominates, and the opacity is determined by the free-free absorption. In the middle region the gas pressure still dominates the radiation pressure, but the opacity is due to Thomson scattering. In the inner region the radiation pressure dominates, and Thomson scattering determines the opacity. For the outer region the optical depth is $\bar{\tau}_{\text{ff}}$. Photons of a particular energy are created at a depth of δz with $\tau_{\text{ff}}^{\nu} \sim 1$ where ν signifies the frequency of the photon

$$\tau_{\text{ff}}^{\nu} \sim \kappa_{\text{ff}}^{\nu} \rho \delta z \sim 1. \tag{2.42}$$

The intensity of the radiation is

$$I_{\nu} \sim j_{\text{ff}}^{\nu} \delta z \sim \frac{j_{\text{ff}}^{\nu}}{\kappa_{\text{ff}}^{\nu} \rho} = B_{\nu}(T_s), \tag{2.43}$$

where B_{ν} is the Plank function, T_s is the temperature at the disk surface, and j_{ff}^{ν} is the free-free emissivity (Netzer, 2006). Defining further,

$$\begin{aligned} B_{\nu}(T) &= \frac{2h\nu^3}{c^2} \left[e^{\frac{h\nu}{kT}} - 1 \right]^{-1}, \\ B_{\nu}(T) &= \frac{j_{\nu}}{\kappa_{\nu} \rho} \longrightarrow \text{Kirchhoff's law.} \end{aligned} \tag{2.44}$$

The outward photon flux through the disk surface is

$$F_\nu = \int_0^{\pi/2} I_\nu \cos\theta d\Omega_{\text{solid}} \sim 2\pi B_\nu(T_s). \tag{2.45}$$

$$F = \int_0^{\infty} F_\nu d\nu \sim a T_s^4. \tag{2.46}$$

This yields a blackbody spectrum for $\bar{\kappa}_{\text{ff}} \gg \kappa_{\text{scat}}$. Having investigated the absorption dominated outer region, the leaves the middle and inner (Thomson scattering) regions to be explored. For the scattering dominated region, let $\delta z^\natural$ be the depth were the photon was created from free-free emission and δs be the path length of the random-walk the photon takes during scattering

$$\tau_{\text{ff}}^\nu \sim \kappa_{\text{ff}}^\nu \rho \delta s \sim 1. \tag{2.47}$$

The intensity of the radiation is

$$I_\nu \sim j_\nu \delta z^\natural. \tag{2.48}$$

If $N_{\nu s}$ is the number of scatterings and λ_{scat} is the mean free path for scattering,

$$N_{\nu s} = \delta s / \lambda_{scat}. \tag{2.49}$$

Therefore the net vertical distance traveled is

$$\delta z^\natural = \lambda_{scat} \sqrt{N_{\nu s}}. \tag{2.50}$$

Rewriting δz,

$$\delta z^\natural \sim (\kappa_{\text{scat}} \kappa_{\text{ff}}^\nu \rho^2)^{-1/2}. \tag{2.51}$$

Re-expressing in terms of δz for comparison to Equation 2.43

$$\delta z^{\natural} \sim \delta z \sqrt{\kappa_{\rm ff}^{\nu}/\kappa_{\rm scat}^{\nu}}. \tag{2.52}$$

Substituting the result into Equation 2.48

$$I_{\nu} \sim \frac{j_{\rm ff}^{\nu}}{\kappa_{\rm ff}^{\nu}} \sqrt{\frac{\kappa_{\rm ff}^{\nu}}{\kappa_{\rm scat}}} \sim B_{\nu}(T_s) \sqrt{\frac{\kappa_{\rm ff}^{\nu}}{\kappa_{\rm scat}}}. \tag{2.53}$$

The outward photon flux is

$$F_{\nu} = \int_0^{\pi/2} I_{\nu} \cos\theta d\Omega_{\rm solid} \sim 2\pi B_{\nu}(T_s) \sqrt{\frac{\kappa_{\rm ff}^{\nu}}{\kappa_{\rm scat}}} \propto \left(\frac{h\nu}{kT_s}\right)^{3/2} e^{-\frac{h\nu}{2kT_s}} \left(e^{\frac{h\nu}{kT_s}} - 1\right)^{-1/2}, \tag{2.54}$$

for $\kappa_{\rm ff}^{\nu} \ll \kappa_{\rm scat}$. This yields a modified blackbody spectral distribution. The effective temperature of the modified blackbody is higher than a normal blackbody, i.e., the energy of the outgoing photons is higher in the scattering dominated region than in the absorption dominated region.

Photoionization equilibrium occurs when the rate of photoionization is equal to the rate of recombination. The ionization parameter quantifies this balance:

$$\begin{aligned} U &= \frac{Q_{\rm ion}(H)}{4\pi r^2 c n_e}. \\ Q_{\rm ion}(H) &= \int \frac{L_{\nu}}{h\nu} d\nu. \end{aligned} \tag{2.55}$$

Here $Q_{\rm ion}(H)$ is the number of H ionizing photon created per second and n_e is the number density of electrons (Shapiro & Teukolsky, 1983).

2.5.1 Other Accretion Models

At luminosities less than a few percent of the Eddington limit, black holes can accrete via an advection-dominated accretion flow (ADAF) (Ichimaru, 1977; Rees et al., 1982).

ADAF can be convectively unstable and become convection-dominated accretion flows (CDAF) (Begelman & Meier, 1982; Narayan & Yi, 1994). CDAFs have a very different structure than ADAFs (Stone et al., 1999). In the numerical simulations, the Reynolds stress due to convection is negative, which means convection moves angular momentum inward rather than outward (Ryu & Goodman, 1992; Stone & Balbus, 1996; Narayan et al., 2000). In the case of a CDAF, convection is so strong that the angular momentum transport inwards is nearly equal to the outward transport by viscosity (Igumenshchev et al., 2000; Quataert & Gruzinov, 2000). This leads to an almost static accretion flow; therefore some of the gas forms convective eddies and does not accrete onto the black hole. Consequently, the mass accretion rate in a CDAF is smaller than in an ADAF.

The spectral models of CDAFs that Ball et al. presented in 2001 are similar to the advection-dominated inflow/outflows solution (ADIOS) models (see Figure 2.13). The high amount of bremsstrahlung emission in the X-ray and the low amount of synchrotron emission in the radio are characteristic of density profiles flatter than the ADAF scaling of $\rho \propto r^{-3/2}$ (could be either CDAF or ADIOS). The similarities in the spectra of ADIOS and CDAF models implies that direct observation of outflowing gas would be needed to confirm the ADIOS or CDAF model, one way or the other (Ball et al., 2001). The primary difference between the CDAF and ADIOS models is that the CDAF models have a unique radial density profile ($\rho \propto r^{-1/2}$), instead of a family of profiles ($\rho \propto r^{-3/2+p}$ with $0 < p < 1$) as in an ADIOS (Ball et al., 2001).

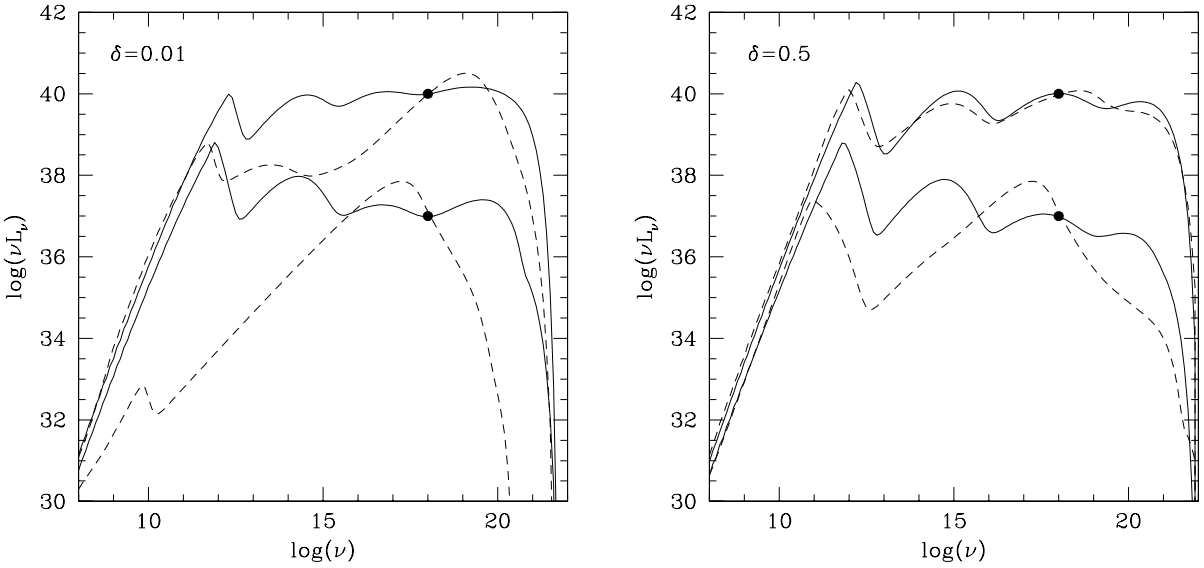

Figure 2.13: Comparison of ADAF and CDAF model spectra. The accretion rates in the models have been adjusted so that the 1 keV luminosities are equal to either 10^{37} ergs/s or 10^{40} ergs/s (solid circles). The ADAF models are the solid curves, and the CDAF models are the dashed curves. δ is the fraction of the viscous dissipation goes directly into heating the electrons, which impacts synchrotron radiation and Compton scattering. This figure is from (Ball et al., 2001).

2.6 AGN Unification

There are attempts to unify all AGN as a single type of astrophysical object. The differences in AGN type 1 and type 2 can be explained by geometrical obscuration of the center of the galaxy viewed at different inclination angles (Antonucci, 1993). Likewise, differences in accretion rate can account for different emission spectra and power outputs. In other words, the differing observations of AGN power output and spectra is due to each galaxy having a unique combination of black hole mass, spin, and accretion rates and the line of sight being fixed at Earth. The unified model consists of a black hole with an accretion disk that radiates. The disk is surrounded by BRLs and NRLs consisting of high and lower velocity gas, respectively. A dusty torus may obscure parts of the accretion disk and BLR. At large viewing angles the torus obscures the inner regions, and it looks like Type 2 Seyferts, narrow-line FRI, and FRII. Closer to line of sight, the torus does not

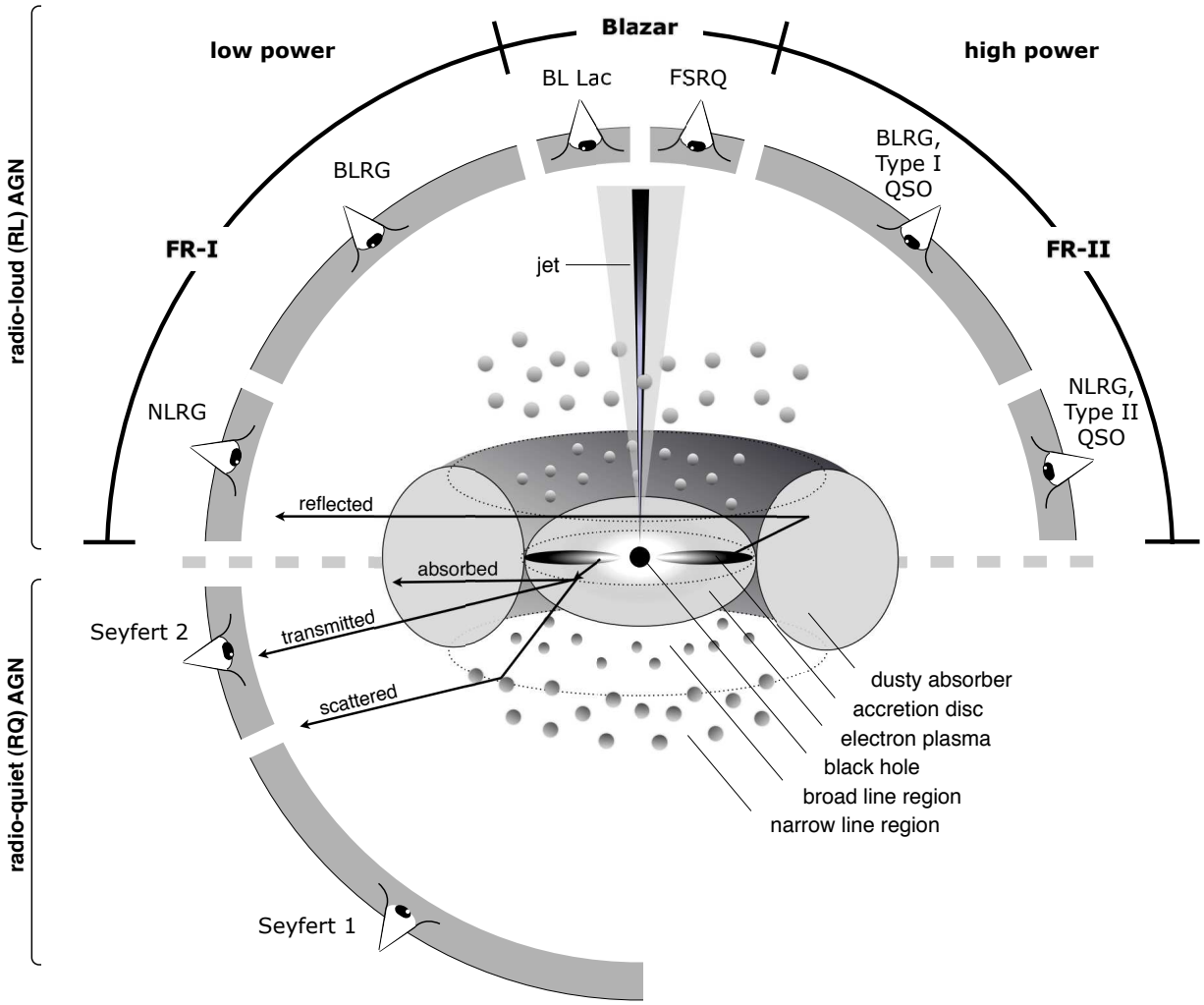

Figure 2.14: A representation of the unified AGN theory (Beckmann & Shrader, 2012). The type of AGN we observe depends on the viewing angle, on the presence of a jet, and on the power of the central engine.

obscure the BLR, and it looks like Type 1 Seyferts, radio quiet QSOs, radio quasars, and FRSQs. For viewing angles looking directly at the nucleus, the relativistically beamed non-thermal continuum emission for the jet dominates, and it's a blazar with BL Lac objects being a subclass of blazars (see Figure 2.14).

Chapter 3

Theoretical Background

3.1 Blandford-Znajek Mechanism

In 1977, Blandford and Znajek proposed that the energy needed to power relativistic jets could be supplied by rotating black holes. The energy stored in the mass of a black hole can only be transformed into electromagnetic energy via Hawking radiation, which is ineffective for powering jets. The rotational energy of a black hole can be transformed into electromagnetic energy if the black hole is in a magnetic field and the magnetosphere is force-free. In the Blanford-Znajek mechanism a rotating black hole in a force-free magnetosphere acts like a unipolar inductor; extracting rotational energy from the black hole and converting it into Poynting flux. The minimum charge density needed for the magnetosphere to be force-free is the Goldreich-Julian charge density.
The sections below will cover theory that is relevant to the Blanford- Znajek process.

3.1.1 Unipolar Inductor

The Blanford-Znajek process treats the black hole like a conductor spinning in a magnetic field, e.g., a unipolar inductor. This section will describe the physics of a unipolar inductor so one can have a better understanding of how energy is extracted from the

black hole. Beginning with Faraday's Law of Induction:

$$\nabla \times \mathbf{E} = -\frac{\partial \mathbf{B}}{\partial t}, \tag{3.1}$$

the physics of a unipolar inductor is very similar to a Faraday disk or a magnetic break. The difference is that for the unipolar inductor, the moving conductor is also magnetic. For a moving conductor, $\mathbf{E} + \mathbf{v} \times \mathbf{B}/c$ acts as an effective electric field and thus drives current. The EMF ($\mathscr{E}$) in a closed loop ($\circlearrowleft$) is (Landau & Lifshitz, 1960),

$$\mathscr{E} = \oint_{\circlearrowleft} (\mathbf{E} + \mathbf{v} \times \mathbf{B}/c) \cdot d\mathbf{l}. \tag{3.2}$$

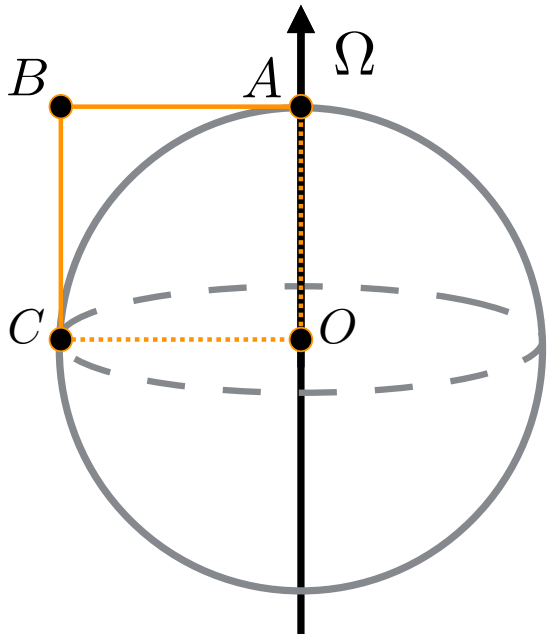

Figure 3.1: The wires (solid orange lines) are stationary, A and C can slide around the magnetized, conducting sphere to keep the circuit stationary. The dotted lines are for reference only, the entire sphere is a conductor and has a radius r_h.

An illustrative toy problem (see Figure 3.1) is when the axes of the dipolar magnetic field and rotation are aligned. Solving for the EMF between the pole and equator and

making a substitution, Equation 3.2 becomes

$$\mathscr{E} = \frac{1}{c}\int_{ABC} (\Omega \times \mathbf{r}) \times \mathbf{B} \cdot d\mathbf{l}. \tag{3.3}$$

Since $\mathscr{E}$ is independent of the path of integration, one can instead integrate along AOC. Along the segment AO, $\Omega \parallel \mathbf{r}$, therefore the cross product is zero, which leaves only the segment OC:

$$\mathscr{E} = \frac{1}{c}\int_0^{r_h} B\Omega r\, dr = \frac{B\Omega {r_h}^2}{2c}. \tag{3.4}$$

The Poynting vector is

$$\mathbf{S} = \frac{c}{4\pi}\mathbf{E} \times \mathbf{B}, \tag{3.5}$$

where, $\mathbf{E} = \mathbf{v} \times \mathbf{B}/c$.

$$\mathbf{S} = \frac{1}{4\pi}(\mathbf{v} \times \mathbf{B}) \times c\mathbf{B} \tag{3.6}$$

$$= \frac{1}{4\pi}\left[c(\mathbf{v} \cdot \mathbf{B})\mathbf{B} - c(\mathbf{B} \cdot \mathbf{B})\mathbf{v}\right]. \tag{3.7}$$

Substituting $\mathbf{v} = \Omega \times \mathbf{r}$

$$= \frac{1}{4\pi}\left[c\mathbf{r} \cdot (\mathbf{B} \times \Omega)\mathbf{B} - B^2(\Omega \times \mathbf{r})\right], \tag{3.8}$$

Since $\Omega \parallel \mathbf{B}$, the cross product is zero, and

$$\mathbf{S} = \frac{-cB^2(\Omega \times \mathbf{r})}{4\pi} = \frac{-cB^2\Omega_F r \sin\theta}{4\pi}\hat{\phi}. \tag{3.9}$$

3.2 Force-Free

A plasma is force-free when the Lorentz force is zero:

$$\rho\mathbf{E} + \mathbf{J} \times \mathbf{B} = 0. \tag{3.10}$$

One solution to this is trivial, $\mathbf{E} = 0$ and $\mathbf{J} = 0$. Another solution is when $\mathbf{E} = 0$ and the magnetic pressure gradient part of $\mathbf{J}\times\mathbf{B}$ exactly counter-balances the tension part of $\mathbf{J}\times\mathbf{B}$ (Cravens, 1997). This can be seen using Ampère's law,

$$\mathbf{J}\times\mathbf{B} = \frac{1}{4\pi}(\nabla\times\mathbf{B})\times\mathbf{B} = -\nabla\left(\frac{B^2}{8\pi}\right) + \frac{1}{4\pi}\mathbf{B}\cdot\nabla\mathbf{B} = 0, \tag{3.11}$$

where $B^2/8\pi$ is the magnetic pressure and $\mathbf{B}\cdot\nabla\mathbf{B}/4\pi$ is the magnetic tension force. This formulation gives one a good physical picture. Another way to expresses the force-free condition is

$$(\rho\mathbf{E} + \mathbf{J}\times\mathbf{B} = 0)\cdot\mathbf{B} \longrightarrow \mathbf{E}\cdot\mathbf{B} = 0. \tag{3.12}$$

The quantity $\mathbf{E}\cdot\mathbf{B}$ is invariant, which is convenient when dealing with black holes.

3.2.1 Goldreich Julian Charge Density

In 1969, Goldreich and Julian were investigating pulsars. They started with the assumption that the magnetosphere around a spinning neutron star was a vacuum; they go on to show that this is physically impossible. Their argument is as follows: the neutron star has an aligned dipole magnetic field,

$$\mathbf{B}^{\text{outside}} = BR^3\left(\frac{\cos\theta}{r^3}\hat{\mathbf{r}} + \frac{\sin\theta}{2r^3}\hat{\theta}\right), \tag{3.13}$$

where I use "outside" and "inside" to signify if the electric or magnetic field is inside or outside of of the neutron star. The magnetic field at the surface of the star is

$$\mathbf{B_r}^{\text{inside}} = B\left(\cos\theta\hat{\mathbf{r}} + \frac{\sin\theta}{2}\hat{\theta}\right). \tag{3.14}$$

Since the magnetic dipole and axis of rotation are aligned, $\mathbf{v} = \Omega_\mathbf{F} \times \mathbf{r}$. The star is assumed to be a perfect conductor, so $\mathbf{E} + \mathbf{v} \times \mathbf{B}/c = 0$. After taking the cross-product,

$$\mathbf{E}^{\text{inside}} = \frac{R\Omega_F B \sin\theta}{c}\left(\frac{sin\theta}{2}\hat{\mathbf{r}} - \cos\theta\hat{\theta}\right). \tag{3.15}$$

The tangential electric field should be continuous across the surface of the neutron star.

$$\mathbf{E}_\theta{}^{\text{outside}} = \frac{\partial}{\partial\theta}\left[-\frac{R\Omega_F B \sin^2\theta}{2c}\right], \tag{3.16}$$

which can be simplified using a Legendre polynomial.

$$\mathbf{E}_\theta{}^{\text{outside}} = \frac{\partial}{\partial\theta}\left[\frac{R\Omega_F B}{3c}P_2(\cos\theta)\right]. \tag{3.17}$$

Now going back to the assumption that outside of the neutron star is vacuum, $\mathbf{E}^{\text{outside}} = -\nabla\phi$, where $\nabla^\mathbf{2}\phi = \mathbf{0}$. Using this and Equation 3.17,

$$\phi = -\frac{R^5\Omega_F B}{3cr^3}P_2(\cos\theta), \tag{3.18}$$

where the $1/r^3$ comes from the radial component. Using Equations 3.13, 3.17, and 3.18,

$$\mathbf{E}\cdot\mathbf{B} = -\frac{\Omega_F R}{c}\left(\frac{R}{r}\right)^7 B^2\cos^3\theta. \tag{3.19}$$

Recal that inside of the pulsar, $\mathbf{E}\cdot\mathbf{B} = 0$. This discrepancy leads to a huge electric field at the surface of the neutron star. The electric field outside of the star at the surface is

$$\mathbf{Er}(R) = -\nabla_r\phi = \frac{R\Omega_F B}{c}P_2(\cos\theta). \tag{3.20}$$

Solving for the electric field at the surface ($r = R$) and at $\theta = \pi$, gives $3R\Omega B/(2c)$. Doing a quick approximation to compare the electric force to the gravitational force shows that

the electric force is strong enough to overcome gravity and rip charges from the surface of the neutron star.

$$\frac{eR\Omega_F B/c}{GMm/R^2} \gg 1. \tag{3.21}$$

After showing a vacuum solution doesn't work, Goldreich and Julian found a steady state solution for the charge density in a highly conductive, corotating magnetosphere.

$$\mathbf{E} = -\frac{\mathbf{v}\times\mathbf{B}}{c} = -\frac{(\Omega_\mathbf{F}\times\mathbf{r})\times\mathbf{B}}{c} = -\frac{\Omega_F r\sin\theta}{c}\hat{\phi}\times\mathbf{B}, \tag{3.22}$$

where θ is the angle between $\Omega_\mathbf{F}$ and $\mathbf{r}$ and $\hat{\phi}$ is the azimuthal unit vector. For a steady state solution, $\partial\mathbf{E}/\partial t = 0$. Plugging the current density, $\mathbf{J} = \rho\mathbf{v}$, and $\mathbf{v} = \hat{\phi}\Omega_F r\sin\theta$ into Ampère's law,

$$\nabla\times\mathbf{B} = 4\pi\rho\frac{\Omega_F r\sin\theta}{c}\hat{\phi} = \nabla\cdot\mathbf{E}\frac{\Omega_F r\sin\theta}{c}\hat{\phi}. \tag{3.23}$$

Now taking the divergence of Equation 3.22,

$$\nabla\cdot\mathbf{E} = -\nabla\cdot\left(\frac{\Omega_F r\sin\theta}{c}\hat{\phi}\times\mathbf{B}\right) = -\left[\mathbf{B}\cdot\left(\nabla\times\frac{\Omega_F r\sin\theta}{c}\hat{\phi}\right) - \frac{\Omega_F r\sin\theta}{c}\hat{\phi}\cdot(\nabla\times\mathbf{B})\right]. \tag{3.24}$$

Substituting Equation 3.23 into Equation 3.24 yields

$$\nabla\cdot\mathbf{E} = -\left[\mathbf{B}\cdot\left(\nabla\times\frac{\Omega_F r\sin\theta}{c}\hat{\phi}\right) - \frac{\Omega_F r\sin\theta}{c}\hat{\phi}\cdot\left(\nabla\cdot\mathbf{E}\frac{\Omega_F r\sin\theta}{c}\hat{\phi}\right)\right] \tag{3.25}$$

$$= -\left[\mathbf{B}\cdot\left(\nabla\times\frac{\Omega_F r\sin\theta}{c}\hat{\phi}\right) - \nabla\cdot\mathbf{E}\left(\frac{\Omega_F r\sin\theta}{c}\right)^2\right]. \tag{3.26}$$

Further simplification gives

$$\nabla\cdot\mathbf{E} = -\mathbf{B}\cdot\left(\nabla\times\frac{\Omega_F r\sin\theta}{c}\hat{\phi}\right)\left[\frac{1}{1-(\Omega_F r\sin\theta/c)^2}\right]. \tag{3.27}$$

Since

$$\mathbf{B}\cdot\left(\nabla\times\Omega_F r\sin\theta\hat{\phi}\right)=\mathbf{B}\cdot(\nabla\times\mathbf{v})=\mathbf{B}\cdot(2\Omega_\mathbf{F}), \tag{3.28}$$

one can write

$$\nabla\cdot\mathbf{E}=-2\frac{\Omega_\mathbf{F}\cdot\mathbf{B}}{c}\left[\frac{1}{1-(\Omega_F r\sin\theta/c)^2}\right], \tag{3.29}$$

with the Goldreich-Julian charge density taking the form to first order

$$\rho_{GJ}\simeq-\frac{\Omega_\mathbf{F}\cdot\mathbf{B}}{2\pi c}. \tag{3.30}$$

Examining a dipole magnetic field, $\mathbf{B}=BR^3(2\cos\theta\hat{\mathbf{r}}+\sin\theta\hat{\theta})/r^3$, yields

$$\rho_{GJ}=\frac{BR^3\Omega_F}{2\pi r^3 c}(1-3\cos^2\theta). \tag{3.31}$$

3.2.2 The Black Hole Magnetosphere

A black hole is a fully general relativistic object. In order to find the charge density in the magnetosphere around a black hole, one may express **E** and **B** in a 3+1 spacetime formulation. Again, this model assumes a stationary, axisymmetric, force-free magnetosphere around a Kerr black hole with mass M and angular momentum J. The Boyer-Lindquist coordinates (t, r, θ, ϕ) with the two scalar functions α and ω are (Thorne et al., 1986):

$$ds^2=\left(\varpi^2\omega^2-\alpha^2\right)dt^2-2\omega\varpi^2 d\phi dt+\frac{\rho^2}{\Delta}dr^2+\rho^2 d\theta^2+\varpi^2 d\phi^2, \tag{3.32}$$

$$\alpha=\frac{\rho}{\Sigma}\sqrt{\Delta}, \tag{3.33}$$

$$\omega=\frac{2aGMr}{c\Sigma^2}. \tag{3.34}$$

where

$$\rho^2=r^2+a^2\cos^2\theta, \tag{3.35}$$

$$\Delta = r^2 + a^2 - 2Mr/c^2, \tag{3.36}$$

$$\Sigma^2 = (r^2 + a^2)^2 - a^2\Delta\sin^2\theta, \tag{3.37}$$

$$\varpi = \frac{\Sigma}{\rho}\sin\theta. \tag{3.38}$$

Here the spin parameter of the black hole is $a \equiv J/Mc$ and the black hole radius is $r_H = GM/c^2 + \left[\left(GM/c^2\right)^2 - a^2\right]^{1/2}$. The redshift factor or the lapse function is α and ω is the angular velocity of the zero angular momentum observers (ZAMO), which coincides with uniform rotation of the black hole and vanishes at infinity. α is called the lapse function because it is the amount of time that elapses for the ZAMO during the passage of global time equal to unity.

The exact solution for **B** for a Kerr black hole in a uniform magnetic field is (Thorne & MacDonald, 1982),

$$\mathbf{B} = \frac{B}{2\Sigma\sin\theta}\left[\frac{\partial}{\partial\theta}\frac{(\Sigma^2 - 4a^2Mr)\sin^2\theta}{\rho^2}\hat{r} - \sqrt{\Delta}\frac{\partial}{\partial r}\frac{(\Sigma^2 - 4a^2Mr)\sin^2\theta}{\rho^2}\hat{\theta}\right]. \tag{3.39}$$

The poloidal magnetic field can be written (Macdonald, 1984) in terms of the magnetic flux function, Ψ,

$$\mathbf{B_p} = \frac{\nabla\Psi\times\hat{\phi}}{2\pi\varpi}. \tag{3.40}$$

Then using the force-free condition to find the poloidal electric field,

$$\mathbf{E_p} = \frac{\Omega_F - \omega}{2\pi\alpha c}\nabla\Psi, \tag{3.41}$$

where the velocity of the magnetic field lines from the ZAMO's reference frame is

$$\mathbf{v_F} = \frac{(\Omega_F - \omega)\varpi}{\alpha}\hat{\phi}. \tag{3.42}$$

Finally expressing the Goldreich-Julian charge density around black hole,

$$\rho_{GJ} = \frac{1}{4\pi}\nabla\cdot\mathbf{E_p} = -\frac{1}{4\pi}\nabla\cdot\left(\frac{\Omega_F-\omega}{2\pi\alpha c}\nabla\Psi\right). \tag{3.43}$$

Chapter 4

Plasma Cascade

As shown in the previous chapter, the charge density needed for the magnetosphere to be force-free is:

$$\rho_{GJ} = -\frac{1}{4\pi}\nabla\cdot\left(\frac{\Omega_F-\omega}{2\pi\alpha c}\nabla\Psi\right). \tag{4.1}$$

There exists a surface where $\rho_{GJ}=0$, see Figure 4.1. In a force-free magnetosphere, this "null surface" has the potential to create a region with a strong electric field, $E_\parallel$, that is parallel to the magnetic field. The charge deficit around the "null surface" allows $E_\parallel$ to emerge. This region will be simply referred to as the gap. Inside of the gap, the Poisson equation is:

$$\nabla\cdot E_\parallel = 4\pi(\rho_e-\rho_{GJ}), \tag{4.2}$$

where the charge density, $\rho_e \equiv e(n^+-n^-)$, is viewed in the corotating frame of the magnetic field and is the difference between positive (n^+) and negative (n^-) charges. As originally suggested in (Blandford & Znajek, 1977), an electron-positron cascade is needed to maintain a force-free magnetosphere around the black hole. Charged particles are accelerated by $E_\parallel$ inside of the gap. These accelerated particles can inverse Compton scatter with background photons, e.g., from the accretion disk. This interaction may produce γ-rays, which can then collide with additional background photons and potentially pro-

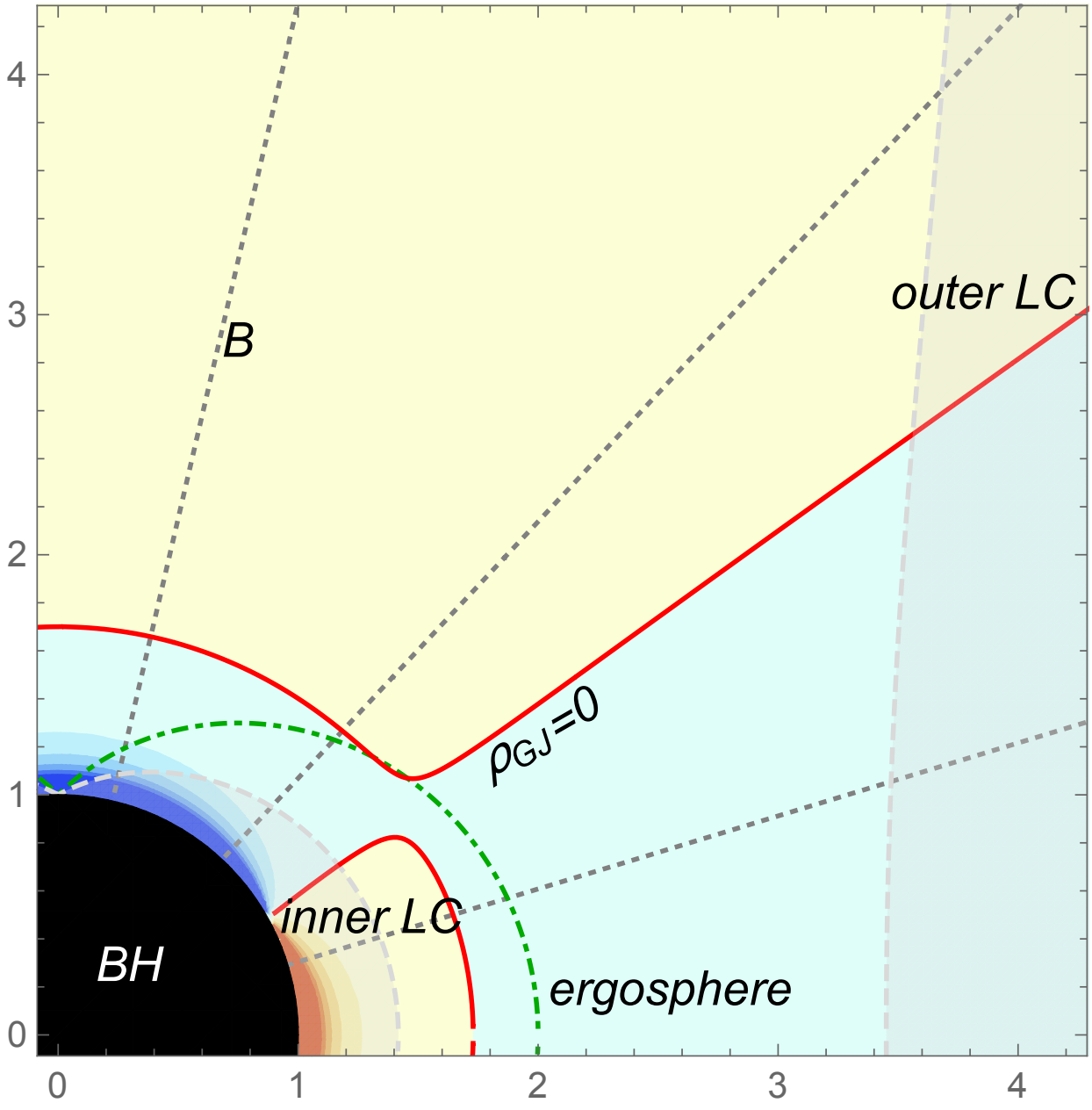

Figure 4.1: The black hole radius is set to one. The blue regions and the red/yellow regions signify the plasma densities. The red, solid line is the surface where ρ_{GJ} goes to zero. The green, dash-dotted line is the ergoshphere. The light gray, long-dashed lines represent the inner and outer light cylinder. And finally, the dark gray, short-dashed lines display the geometry of the magnetic field lines.

duce electron-positron pairs. The pairs that are produced in turn are accelerated and repeat the process until the magnetosphere is filled.

4.1 Electric Field and Charge Acceleration

In the gap, there is insufficient plasma to screen out an electric field, which leads to the emergence of $E_{\|}$. Consider the case where B_p is perpendicular to the surface of the black hole. This is the most efficient geometry for the cascade.

$$\nabla \cdot E_{\|} = 4\pi \left\{ e\left[n^{+}(x,\theta) - n^{-}(x,\theta)\right] - \rho_{GJ}(x,\theta) \right\}, \tag{4.3}$$

where x is perpendicular to the null surface and zero at the center of the gap, i.e., $x = (r - r_0)$, with r_0 being the null surface. As will be shown, the gap is considerably smaller than r_H; therefore, one can expand $\rho_{GJ}(x,\theta)$ around $x = 0$, the center of the gap. The expansion coefficient, $A(\theta) = \partial_r(\rho_{GJ}(x,\theta))$ at $x = 0$, can be solved analytically for a given θ. For simplicity, the geometry is reduced to one dimension and the Poisson equation is rewritten,

$$\frac{dE_{\|}}{dx} = 4\pi \left(e\left[n^{+}(x) - n^{-}(x)\right] - A_{\theta} x \right), \tag{4.4}$$

where A_{θ} is the plasma expansion coefficient at a particular angle.

Inside of the gap, the electrons-positrons will be accelerated by the $E_{\|}$ field. The motion of a single charge can be determined by:

$$m_e c^2 \frac{d\Gamma}{dx} = eE_{\|}(x) - \left(\Gamma^2(x) - 1\right) \sigma_T U_b, \tag{4.5}$$

where Γ, σ_T, and U_b are the Lorentz factor of the $e^{\pm}$, the Thomson cross section, and the energy density of the background photon field, respectively. These accelerated charges can produce γ-ray photons via inverse Compton scattering with background photons

(Beskin et al., 1992; Hirotani & Okamoto, 1998). The newly created γ-rays can now pair produce by colliding with another background photon, and the process continues until the charge density inside of the gap reaches ρ_{GJ}, i.e., the electric field goes to zero.

4.2 Radiation

Electromagnetic radiation can be produced and interact with the environment in many different ways. For the region inside of the gap, the radiation processes that are of importance are inverse Compton scattering and pair production.

4.2.1 Compton Scattering

Compton scattering describes the interaction between photons and charged particles. The photon imparts energy to the charged particle. The energy loss of the photon is $\Delta E = hc/\Delta\lambda$ with $\Delta\lambda = h/(mc)(1-\cos\theta)$ where θ is the angle between the photon and charged particle and m is the mass of the charge particle. The energy of the photon after interaction is therefore,

$$E_f = \frac{E_i}{1+E_i/(mc^2)(1-\cos\theta)}, \tag{4.6}$$

with E_i and E_f are the photon's incoming and outgoing energy, respectively.

The cross-section for a high energy system is characterized by the Klein-Nishina formula derived by using quantum electrodynamics. For the following equations the energy of incoming photon is expressed in units of the rest mass energy of the charged particle, $\epsilon = E_i/(mc^2)$. Using the classical electron radius, $r_e = q^2/(mc^2)$, the associated differential cross-section is

$$\frac{d\sigma}{d\Omega} = \frac{1}{2}r_e^2 f(\epsilon,\theta)\left(f(\epsilon,\theta)^2 + f(\epsilon,\theta)^{-1} - \sin^2\theta\right), \tag{4.7}$$

with

$$f(\epsilon,\theta) = \frac{1}{1+\epsilon(1+\cos\theta)}. \tag{4.8}$$

The total Klein-Nishina cross-section is (e.g., Rybicki & Lightman 1979)

$$\sigma_{KN} = \frac{3\sigma_T}{4}\left\{\frac{1+\epsilon}{\epsilon^3}\left[\frac{2\epsilon(1+\epsilon)}{1+2\epsilon} - \ln(1+2\epsilon)\right] + \frac{\ln(1+2\epsilon)}{2\epsilon} - \frac{1+3\epsilon}{(1+2\epsilon)^2}\right\}, \tag{4.9}$$

where σ_T is the Thomson cross-section:

$$\sigma_T = 2\pi\int_o^\pi \frac{d\sigma}{d\Omega}\sin\theta d\theta = \frac{8\pi}{3}r_e^2 = \frac{8\pi}{3}\left(\frac{q^2}{mc^2}\right)^2. \tag{4.10}$$

For an electron, $\sigma_T \simeq 6.653\times10^{-25}\text{cm}^2$.

4.2.2 Inverse Compton Scattering

In Compton scattering a charged particle gains energy from interacting with a photon. The reverse of this process is simply called inverse Compton scattering. The Compton redistribution function is

$$\eta_c = \int_{\epsilon_{\min}}^{\epsilon_{\max}} \sigma_{KN}(\epsilon_s\Gamma)\frac{dN_s}{d\epsilon_s}\delta(\epsilon_\gamma - \Gamma^2\epsilon_s)d\epsilon_s. \tag{4.11}$$

The model of the gap assumes a power law representation of the background spectral number density per $d\epsilon$.

$$\frac{dN_s}{d\epsilon_s} = \frac{2-\alpha}{\epsilon_{\max}^{2-\alpha} - \epsilon_{\min}^{2-\alpha}}\frac{U_b}{m_e c^2}\epsilon_s^{-\alpha}, \tag{4.12}$$

where $\epsilon_{\max} = 0.2$ and $\epsilon_{\min} = 8\times10^{-6}$, which correspond to 102 keV and 4.1 eV, respectively. This gives a range of background photons from hard X-rays to microwave for the accelerated charges with which to inverse Compton scatter. The background energy density, U_b, can be estimated in terms of the Eddington luminosity, L_{edd} (Hirotani & Okamoto, 1998),

$$U_b \simeq \frac{L_b}{4\pi c(5r_H)^2} = 1.5\times10^6\left(\frac{10^8 M_\odot}{M}\right)\left(\frac{L_b}{L_{\text{edd}}}\right)\frac{\text{ergs}}{\text{cm}^3}. \tag{4.13}$$

The Eddington luminosity is the luminosity when there is balance between the force of radiation acting outward and the gravitational force acting inward. The maximum luminosity that the black hole can have without ejecting ionized hydrogen via radiation pressure is

$$L_{\rm edd} = \frac{4\pi cGMm_H}{\sigma_T} \simeq 1.25\times10^{46}\left(\frac{M}{10^8 M_\odot}\right)\frac{\rm ergs}{\rm s}. \tag{4.14}$$

4.2.3 Pair Production

When the energy of two photons exceeds the rest mass energy of a particle and its anti-particle, then pair production can occur. Conservation laws must be maintained; therefore energy, momentum, angular momentum, electric charge, and lepton number must be conserved. Since photons are not leptons and are neutral, total charge and lepton number for the pair must be zero. The pairs that can be produced via photon collisions are electron-positron ($e^{\pm}$), muon and anti-muon, and tau and anti-tau. The minimum energy needed to produce $e^{\pm}$ is 1022 keV. If a γ-ray with energy $m_e c^2\epsilon_\gamma$ collides with a background photon with an energy $m_e c^2\epsilon_s$, then to produce an $e^{\pm}$ pair the energies must satisfy:

$$\epsilon_\gamma\epsilon_s \geq 2/(1-\mu), \tag{4.15}$$

where μ is the cosine of the angle between the colliding photons. The cross-section for electron-photon interactions expressed in terms of kinematic invariants is (Berestetskiĭ et al., 1971)

$$\frac{d\sigma}{dt} = \frac{8\pi r_e^2 m^2}{(s-m^2)^2}\left[\left(\frac{m^2}{s-m^2}+\frac{m^2}{u-m^2}\right)^2+\left(\frac{m^2}{s-m^2}+\frac{m^2}{u-m^2}\right)-\frac{1}{4}\left(\frac{s-m^2}{u-m^2}+\frac{u-m^2}{s-m^2}\right)\right], \tag{4.16}$$

where the kinematic invariants in units $c = 1$ are

$$\begin{aligned} s = (p+k)^2 = (p'+k')^2 = m^2 + 2pk = m^2 + 2p'k' \\ t = (p-p')^2 = (k'-k)^2 = 2(m^2 - pp') = -2kk' \\ u = (p-k')^2 = p'-k)^2 = m^2 - 2pk' = m^2 - 2p'k \\ s+t+u = 2m^2. \end{aligned} \tag{4.17}$$

Here p and k are the 4-momentum of the electron and photon before the collision and p' and k' are their 4-momentum after the collision (Berestetskiĭ et al., 1971). Applying Equation 4.16 to a photon-photon collision,

$$\sigma_p = \frac{\pi r_e^2}{2}(1-v^2)\left[(3-v^4)\ln\left(\frac{1+v}{1-v}\right) - 2v(2-v^2)\right], \tag{4.18}$$

where

$$v(\mu, \epsilon_\gamma, \epsilon_s) = \sqrt{1 - \frac{2}{1-\mu}\frac{1}{\epsilon_\gamma \epsilon_s}}. \tag{4.19}$$

Expressed in terms of the Thompson cross-section,

$$\sigma_p = \frac{3}{16}\sigma_T(1-v^2)\left[(3-v^4)\ln\left(\frac{1+v}{1-v}\right) - 2v(2-v^2)\right]. \tag{4.20}$$

The angle-averaged pair production redistribution function is (Berestetskiĭ et al., 1971),

$$\eta_p(\epsilon_\gamma) = \frac{1}{2}\int_{-1}^{1} d\mu \int_{2/(\epsilon_\gamma - \epsilon_\gamma \mu)}^{\epsilon_{\max}} \sigma_p \frac{dN_s}{d\epsilon_s} d\epsilon_s. \tag{4.21}$$

4.3 Current Density and γ-ray Production

Now contemplating the continuity equations for $e^{\pm}$, consider the case where positrons flow outward along the equator and current flows toward the black hole at the axis of

rotation. The continuity equations are:

$$\pm \frac{d}{dx}\left\{ n^{\pm}(x)\sqrt{1-\frac{1}{\Gamma^2(x)}} \right\} = \int_0^{\infty} \eta_p(\epsilon_\gamma)\left[F^{+}(x,\epsilon_\gamma)+F^{-}(x,\epsilon_\gamma)\right] d\epsilon_\gamma, \tag{4.22}$$

where η_p is the angle-averaged pair production redistribution function and $F^{\pm}$ are the number densities of the γ-rays traveling in the $\pm$x direction. At the boundary of the gap, $E_{\|}$ must go to zero. This only happens when $j_0 = j_{\rm critical}$, where j_0 is defined by:

$$j_0 \equiv e\left[n^{+}(x)+n^{-}(x)\right]\sqrt{1-1/\Gamma^2(x)}. \tag{4.23}$$

The critical current density is the constant outflow from the gap. The γ-ray distribution functions, $F^{\pm}$, obey:

$$\pm \frac{\partial}{\partial x}F^{\pm}(x,\epsilon_\gamma) = \eta_c(\epsilon_\gamma,\Gamma(x))n^{\pm}(x)\sqrt{1+\frac{1}{\Gamma^2(x)}} - \eta_p(\epsilon_\gamma)F^{\pm}(x,\epsilon_\gamma), \tag{4.24}$$

where η_c is the Compton redistribution function (Hirotani & Okamoto, 1998). In order to numerically solve for the γ-ray distribution, ϵ_γ needs to be split into energy bins. Let ξ_i and ξ_{i-1} be the upper and lower limits of the $i^{\rm th}$ normalized energy bin. This allows one to rewrite the integral in Equation 4.22 as a summation of

$$\int_{\xi_{i-1}}^{\xi_i} \eta_p(\epsilon_\gamma)F^{\pm}(x,\epsilon_\gamma)d\epsilon_\gamma. \tag{4.25}$$

Defining

$$\eta_{p,i} \equiv \eta_p(\frac{\xi_i+\xi_{i-1}}{2}), \tag{4.26}$$

and

$$f_i^{\pm}(x) \equiv \int_{\xi_{i-1}}^{\xi_i} F^{\pm}(x,\epsilon_\gamma)d\epsilon_\gamma, \tag{4.27}$$

re-expressing Equation 4.22 as

$$\pm \frac{d}{dx}\left\{ n^{\pm}(x)\sqrt{1-\frac{1}{\Gamma^2(x)}} \right\} = \sum_{i=1}^{m} \eta_{p,i}\left[f_i^{+}(x) + f_i^{-}(x) \right], \tag{4.28}$$

where m is the number of normalized energy bins. Making a similar approximation as in Equation 4.27 for η_c,

$$\eta_{c,i}\left(\Gamma(x)\right) \equiv \int_{\xi_{i-1}}^{\xi_i} \eta_c\left(\epsilon_\gamma, \Gamma(x)\right) d\epsilon_\gamma, \tag{4.29}$$

allows one to express Equation 4.24 as

$$\pm \frac{d}{dx} f_i^{\pm}(x) = \eta_{c,i}(\Gamma(x)) n^{\pm}(x) \sqrt{1+\frac{1}{\Gamma^2(x)}} - \eta_{p,i} f^{\pm}(x). \tag{4.30}$$

Splitting ϵ_γ into m discrete energy bins leaves one with 2m+3 ordinary differential equations (ODEs). Exploiting the symmetry in the gap and determining appropriate boundary conditions will allow one to examine the structure of the gap.

4.4 Boundary Conditions

The assumptions of symmetry that are used are as follows:

$$\begin{aligned} E_{\parallel}(x) &= E_{\parallel}(-x) \\ \Gamma(x) &= \Gamma(-x) \\ n^{+}(x) &= n^{-}(-x) \\ F^{+}(x) &= F^{-}(-x). \end{aligned} \tag{4.31}$$

These assumptions are appropriate as long as the gap width stays small, $< 1\%$, of the black hole radius. Using these symmetries allows one to set the boundary conditions at the center of the gap and the edge of the gap, which allows one to only integrate over half

of the gap and to obtain a full solution. Using Eq. 4.5 with $E_{\|}(x) = E_{\|}(-x)$ and $\Gamma(x) = \Gamma(-x)$ at $x = 0$ gives a boundary condition on $E_{\|}$:

$$E_{\|} = \frac{\sigma_T U_b}{e}(\Gamma^2 - 1). \tag{4.32}$$

Using Eq. 4.23 with $n^+(x) = n^-(-x)$ at $x = 0$ gives another boundary condition.

$$2n^+\sqrt{1-\frac{1}{\Gamma^2}} = \frac{j_0}{e}. \tag{4.33}$$

Using $F^+(x) = F^-(-x)$ at $x = 0$ gives another boundary condition.

$$f_i^+ = f_i^-. \tag{4.34}$$

The boundary of the gap is defined as the position when the plasma density in the gap is equal to ρ_{GJ}. Using Equation 4.3 at $x = H$ gives a boundary condition on $E_{\|}$.

$$E_{\|} = 0. \tag{4.35}$$

$E_{\|}$ should go to zero smoothly at the boundary; therefore, $dE_{\|}/dx = 0$ at $x = H$. Using this condition and Equation 4.23 at $x = H$ gives another boundary condition.

$$j_0\left(1-\frac{1}{\Gamma^2}\right)^{-1/2} - A_\theta x = 0. \tag{4.36}$$

All of the charged particles are created inside of the gap; therefore, no charges should enter into the gap. Using $n^- = 0$ and Equation 4.23 at $x = H$ gives another boundary condition.

$$n^+\sqrt{1-\frac{1}{\Gamma^2}} = \frac{j_0}{e}. \tag{4.37}$$

Boundary Condition	Equation Used	Assumptions	Boundary
$E_{\parallel} = (\Gamma^2 - 1)\sigma_T U_b / e$	$m_e c^2 d\Gamma/dx = eE_{\parallel} - \left(\Gamma^2 - 1\right)\sigma_T U_b$	$E_{\parallel}(x) = E_{\parallel}(-x)$ & $\Gamma(x) = \Gamma(-x)$	$x = 0$
$2n^+\sqrt{1-1/\Gamma^2} = j_0/e$	$j_0 = e\left[n^+(x) + n^-(x)\right]\sqrt{1-1/\Gamma^2(x)}$	$n^+(x) = n^-(-x)$	$x = 0$
$f_i^+ = f_i^-$	$f_i^{\pm}(x) \equiv \int_{\xi_{i-1}}^{\xi_i} F^{\pm}(x, \epsilon_\gamma) d\epsilon_\gamma$	$F^+(x) = F^-(-x)$	$x = 0$
$E_{\parallel} = 0$	$dE_{\parallel}/dx = 4\pi\left[e\left(n^+ - n^-\right) - \rho_{GJ}\right]$	$\rho_{\rm gap} = \rho_{GJ}$	$x = H$
$n + \sqrt{1-1/\Gamma^2} = j_0/e$	$j_0 = e\left[n^+(x) + n^-(x)\right]\sqrt{1-1/\Gamma^2(x)}$	$n^-(x) = 0$	$x = H$
$j_0\left(1-1/\Gamma^2\right)^{-1/2} - Ax = 0$	$j_0 = e\left[n^+(x) + n^-(x)\right]\sqrt{1-1/\Gamma^2(x)}$	$dE_{\parallel}/dx = 0$	$x = H$
$f_i^- = 0$	$f_i^-(x) \equiv \int_{\xi_{i-1}}^{\xi_i} F^-(x, \epsilon_\gamma) d\epsilon_\gamma$	$F^-(x) = 0$	$x = H$

Table 4.1: A complete overview of the boundary conditions and assumptions used to arrive at them.

All up-scatered photons are created inside of the gap. Assuming none will be coming into the gap gives another boundary condition.

$$f_i^- = 0. \tag{4.38}$$

This provides 2m+5 boundary conditions for 2m+3 ODEs and 2 constants: j_0 and H. These boundary conditions have be summarized in Table 4.1 for reference and clarity.

Chapter 5

Computational Methods

This chapter covers the numerical methods used to solve the coupled ODEs, as well as any issues that arose and preliminary results.

5.1 Expressing Equations in terms of Current Density

The ability to arrive at a solution to the system of ODE's has a strong dependence on j_0. Figure 5.1 shows the numerical convergence's dependence on j_0. In order to easily adjust j_0 to find convergence, re-expressing the equations in terms of current density instead of number density is useful. Restating the definition from Equation 4.23 and defining a new function for the difference between the inward and outward current densities.

$$j_0 \equiv e\left[n^+(x) + n^-(x)\right]\sqrt{1-1/\Gamma^2(x)}. \tag{5.1}$$

$$j_{\text{diff}}(x) \equiv e\left[n^+(x) - n^-(x)\right]\sqrt{1-1/\Gamma^2(x)}. \tag{5.2}$$

Using these definitions allows one to write Equations 4.28 as,

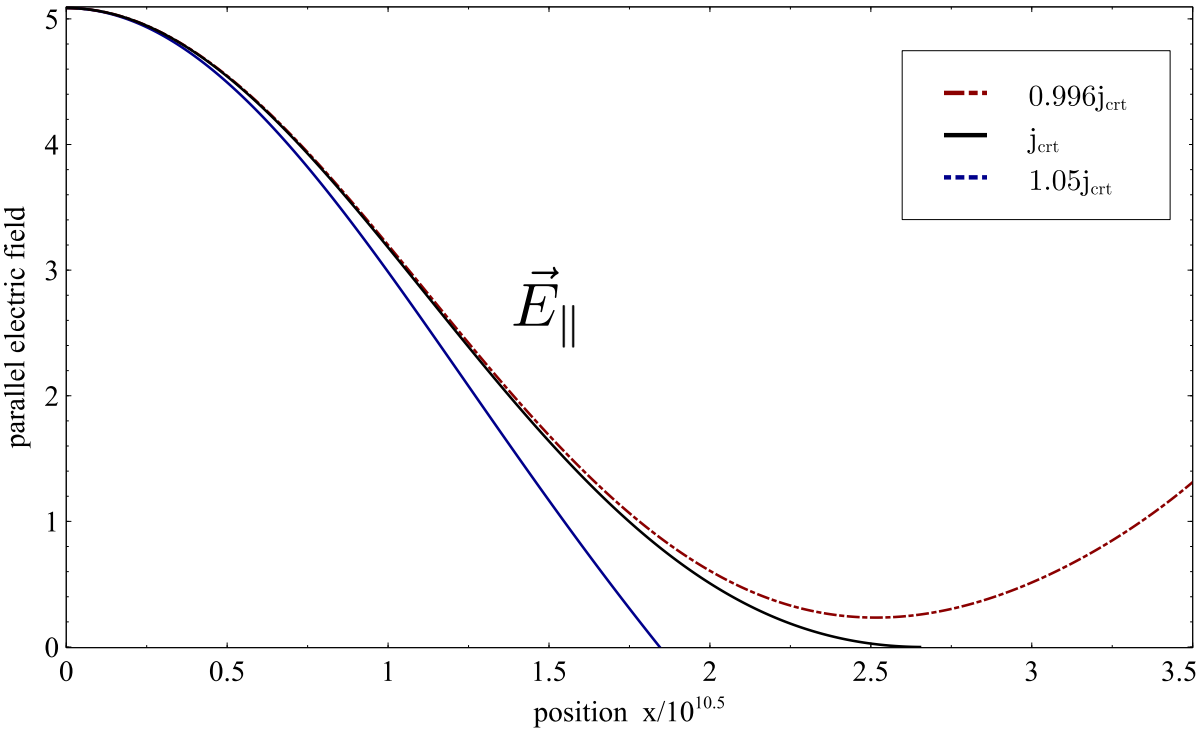

Figure 5.1: The $j_0 = j_{\mathrm{crt}}$ dependence of the solution to $E_{\|}$. This shows $E_{\|}$ as a function of the position along the field line for an arbitrary A_θ. The center of the gap is at zero.

$$\frac{d}{dx}\left\{\left[n^+ - n^-\right]\sqrt{1-1/\Gamma^2(x)}\right\} = \frac{d}{dx}\frac{j_{\text{diff}}(x)}{e} = 2\sum_{i=1}^{m}\eta_{p,i}\left[f_i^+(x) + f_i^-(x)\right], \tag{5.3}$$

$$\frac{d}{dx}\left\{\left[n^+ + n^-\right]\sqrt{1-1/\Gamma^2(x)}\right\} = \frac{d}{dx}\frac{j_0}{e} = 0. \tag{5.4}$$

This shows, as stated previously, that j_0 is a constant. The two boundary conditions that were dependent on n^+ (Equations 4.33 & 4.37) can be reworked and take the form

$$j_{\text{diff}}(0) = 0, \tag{5.5}$$

$$j_{\text{diff}}(H) = j_0. \tag{5.6}$$

Now instead of having to adjust $n^\pm$ separately at each boundary, one just has to adjust j_{diff} to satisfy the boundary conditions.

Similarly, Equations 4.30 can be reformulated in terms of current density.

$$\frac{df_i^+}{dx} - \frac{df_i^-}{dx} = \eta_{c,i}(\Gamma(x))\frac{j_0}{e} - \eta_{p,i}\left[f_i^+(x) + f_i^-(x)\right], \tag{5.7}$$

$$\frac{df_i^+}{dx} + \frac{df_i^-}{dx} = \eta_{c,i}(\Gamma(x))\frac{j_{\text{diff}}(x)}{e} - \eta_{p,i}\left[f_i^+(x) - f_i^-(x)\right]. \tag{5.8}$$

The two boundary conditions that are dependent on $f^\pm$ (Equations 4.34 & 4.38) can be rewritten as,

$$f_i^+ - f_i^- = 0 \tag{5.9}$$

$$f_i^+ - f_i^- = f_i^+ + f_i^-. \tag{5.10}$$

After integration, one wants $f_i^\pm$ and not $f_i^+ \pm f_i^-$, which can be easily found,

$$f_i^+ = \frac{(f_i^+ + f_i^-) + (f_i^+ - f_i^-)}{2} \tag{5.11}$$

$$f_i^- = \frac{(f_i^+ + f_i^-) - (f_i^+ - f_i^-)}{2}. \tag{5.12}$$

And Equation 4.4 becomes

$$\frac{dE_{\parallel}}{dx} = 4\pi \left[j_{\rm diff}(x) \left(1 - 1/\Gamma^2(x)\right)^{-1/2} - A_\theta x \right]. \tag{5.13}$$

The new Equation 5.13 does not require rewritten boundary conditions because $E_{\parallel}$ at $x = 0$ does not have a $n^{\pm}$ dependence and $E_{\parallel}$ at $x = H$ was already expressed in terms of j_0. Numerically solving the equations expressed in terms of current density makes adjusting j_0 to arrive at a solution straight forward.

5.2 Determining the Energy Bins for the γ-rays

In pair production, for γ-ray photons to be produced,

$$\epsilon_\gamma > \frac{2}{\epsilon_s(1-\mu)}, \tag{5.14}$$

where, as a reminder, μ is the cosine of the angle between ϵ_γ and ϵ_s. The minimum value for a pair producing γ-ray is, therefore, $1/\epsilon_{\rm max}$. This is intuitive: the most energetic background photon is able to pair produce with the least energetic γ-ray. Using this to set the lower limit of the lowest energy bin yields,

$$\xi_0 m_e c^2 = \frac{m_e c^2}{\epsilon_{\rm max}} \simeq 2.56 \text{ MeV}. \tag{5.15}$$

The range of energy bins for ϵ_γ that is used is determined to be large enough so long as $\xi_m > \Gamma^2_{\rm max}\epsilon_{\rm max}$, which is the largest value for ϵ_γ that will satisfy the Dirac delta function in Equation 4.11. Due to the power law nature of the spectrum, a power law spacing for the energy bins is used,

$$\xi_i = \frac{2^{i/2}}{\epsilon_{\rm max}}. \tag{5.16}$$

Typically, the number of energy bins needed is less that 50.

5.3 Numerical Integration

The system of ODEs are not completely defined at one boundary, instead their boundary conditions are split over two boundaries. One method is to begin by setting the mass, spin, magnetic field strength, and background energy density. Then choose what angle (θ) to integrate along and set the initial guess for $\Gamma(0)$ and $f_i^-(0)$. Integration was done using the 4^{th} order Runge-Kutta method (RK4) and using a shooting method to satisfy the boundary conditions.

5.3.1 Runge-Kutta Method

The form of a generic 1D differential equation is,

$$\frac{dy}{dx} = f(x, y), \quad y(0) = y_0. \tag{5.17}$$

One can numerically solve Equation 5.17 using a RK4. The Runge-Kutta fourth order method has the form,

$$y_{i+1} = y_i + (a_1 k_1 + a_2 k_2 + a_3 k_3 + a_4 k_4), \tag{5.18}$$

where

$$\begin{aligned} k_1 &= hf(x_i, y_i) \\ k_2 &= hf(x_i + \alpha_2 h, y_i + \beta_2 k_1) \\ k_3 &= hf(x_i + \alpha_3 h, y_i + \beta_3 k_2) \\ k_4 &= hf(x_i + \alpha_4 h, y_i + \beta_4 k_3). \end{aligned} \tag{5.19}$$

One needs to solve for 10 unknowns (a_1, a_2, a_3, a_4, α_2, α_3, α_4, β_2, β_3, and β_4). Begin looking for the unknowns by taking a Taylor expansion of $y_{i+1} = y(x_i + h)$. The Taylor expansion

yields,

$$y(x_i + h) = y(x_i) + hy'(x_i) + \frac{1}{2!}h^2 y''(x_i) + \frac{1}{3!}h^3 y'''(x_i) + \frac{1}{4!}h^4 y''''(x_i) + O(h^5). \tag{5.20}$$

Substituting, $f(x, y)$ for y',

$$y_{i+1} = y_i + hf(x_i, y_i) + \frac{h^2}{2}f'(x_i, y_i) + \frac{h^3}{6}f''(x_i, y_i) + \frac{h^4}{24}f'''(x_i, y_i) + O(h^5). \tag{5.21}$$

Next Taylor expand Equation 5.18 and compare to Equation 5.21. Match terms and solve for the 10 unknowns. A common solution and the one used is,

$$y_{i+1} = y_i + (k_1 + 2k_2 + 2k_3 + k_4)/6 + O(h^5). \tag{5.22}$$

5.3.2 Shooting Method

Insure the boundary conditions are met by using RK4 to integrate from the center of the gap ($x = 0$) to the boundary of the gap ($x = H$) and checking that $E_\parallel$ goes to zero. Then one checks to see if $dE_\parallel/dx$ also goes to zero. If not, $\Gamma(0)$ is adjusted, and the integration from the center of the gap is done again. This is repeated until $dE_\parallel/dx$ is zero. Once the conditions of $E_\parallel = 0$ and $dE_\parallel/dx = 0$ at $x = H$ are met, one checks that the $f_i^-(H)$ are zero. If not, adjust $f_i^-(0)$ and integrate again while checking that $dE_\parallel/dx$ still goes to zero after each integration. This is repeated until $f_i^-(H) = 0$ is satisfied for all $f_i^-(H)$. The pseudo-code illustrating this loop structure follows below.

while $f_i^-(0) \neq 0$ **do**
  while $dE_{\|}/dx \neq 0$ **do**
    while $E > 0$ and $E < E_{\text{prev}}$ **do**
      RK4
    end while
    if $E < 0$ **then**
      Increase $\Gamma(0)$
    else
      Decrease $\Gamma(0)$
    end if
  end while
  if $f_i^- > 0$ **then**
    Decrease $f_i^-(0)$
  else
    Increase $f_i^-(0)$
  end if
end while

5.4 1D Results

After writing the code, it is always necessary to check and make sure the results for a run work and to optimize accordingly. The structure of the gap for a preliminary run shown in Figure 5.2 is for a single 1D solution for an arbitrary A_θ. And an example of the solution's sensitivity on the value of j_0 is shown in Figure 5.1.

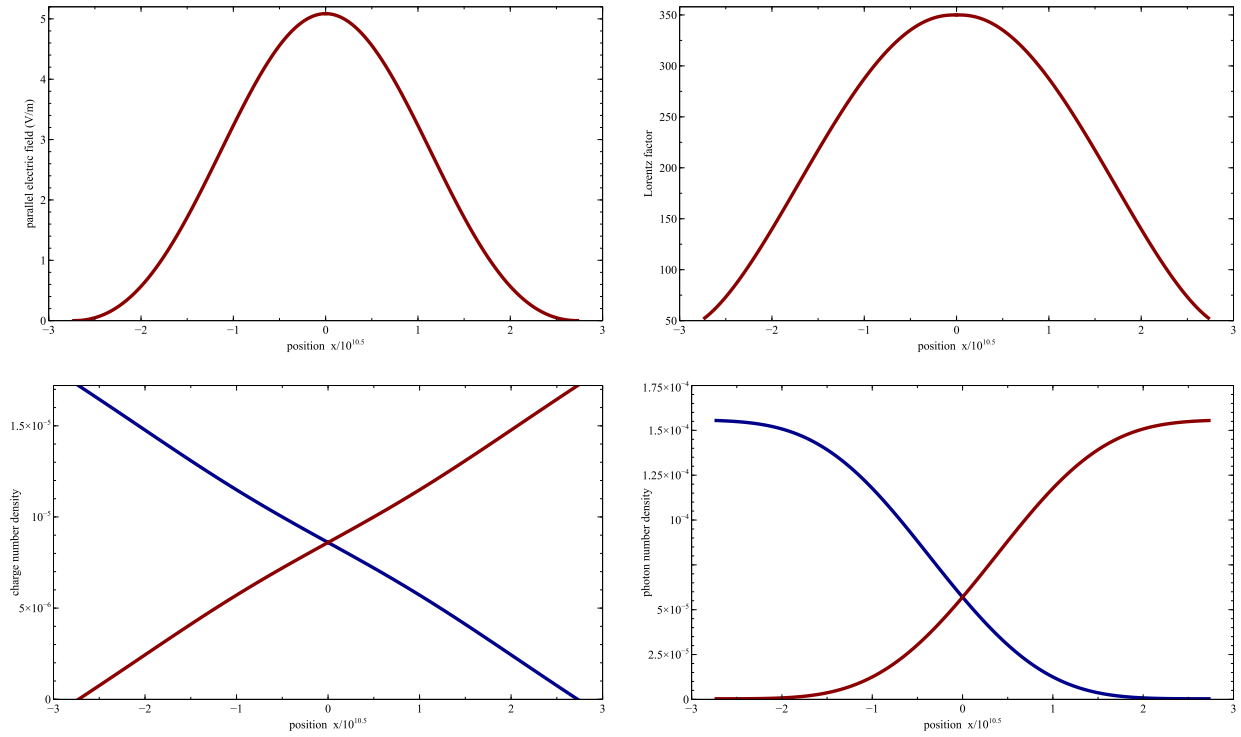

Figure 5.2: The structure of the gap starting in the upper left and going clockwise, the figures show the variation of $E_{||}$, Lorentz factor, charge number density, and photon number density as a function of the position along the field line for an arbitrary value of A_θ. The center of the gap is at zero. The red and blue lines signify motion away from and toward the black hole, respectively.

After optimizing the 1D code, a 2D solver for the structure of the gap was implemented by finding a new A_θ before each 1D run. In order to find a proper A_θ, ρ_{GJ} needs to be expanded about its position where $\rho_{GJ} = 0$. The code implemented solves $\rho_{GJ}(r_0, \theta) = 0$ for r_0, given θ. This r_0 is then used to find A_θ. Similarly, an implementation for runs that vary mass, spin, or magnetic field strength require A_θ to be computed before each 1D run. The pseudo-code illustrating the loop structure for a 2D run that varies the mass of the black hole is shown below.

$\theta = \theta_{\text{start}}$ initial θ
$M = M_{\text{start}}$ initial mass
$B = B$ magnetic field
$a = a$ spin
$r_0 = r_H$ initial guess for the radius where $\rho_{GJ} = 0$
$\delta_M = \delta_M$ the step size parameter for mass
$\delta_\theta = \delta_\theta$ the step size parameter for θ

```
while M < M_finish do
  while θ < θ_finish do
    while ρ ≠ 0 do
      ρ = ρ_GJ(r_0, θ, M, B, a)
      if ρ ≠ 0 then
        Adjust r_0
      end if
    end while
    A = A_θ(r_0, θ, M, B, a)
    while boundary conditions are not satisfied do
      RK4
    end while
    θ = θ + δ_θ · θ
  end while
  M = M + δ_M · M
end while
```

Chapter 6

Structure of the Gap

6.1 Detailed Structure of the Gap

The 2D structure of the gap allows one to examine the inclination angle at which the plasma cascade process is most efficient. The width of the gap can be used as a proxy for efficiency of the cascade process. The maximum Lorentz factor can be used as a proxy for the available energy in the cascade process. In Figures 6.1, 6.2, 6.3, & 6.5, the size of the gap relative to the black hole radius is not to scale, but it is reflective of the actual shape of the gap. The peak Lorentz factor, as shown in Figure 6.1 is 1950 at $\theta = 0$. The corresponding electric field strength at $\theta = 0$ is 160 V/m and is also the peak electric field. The gap width is at it's minimum value at $\theta = 0$ as well. This is strong evidence that the cascade process is most efficient along the axis of rotation. Figure 6.4 shows the spectral transition through the gap. Each line is a snapshot in space of the up-scattered Compton spectrum in the gap. Looking closely at the tail, one can see slight softening of the spectrum before it exits the gap. Figure 6.5 illustrates the outgoing energy flux of the γ-rays that are from the Comptonization of the ambient photons.

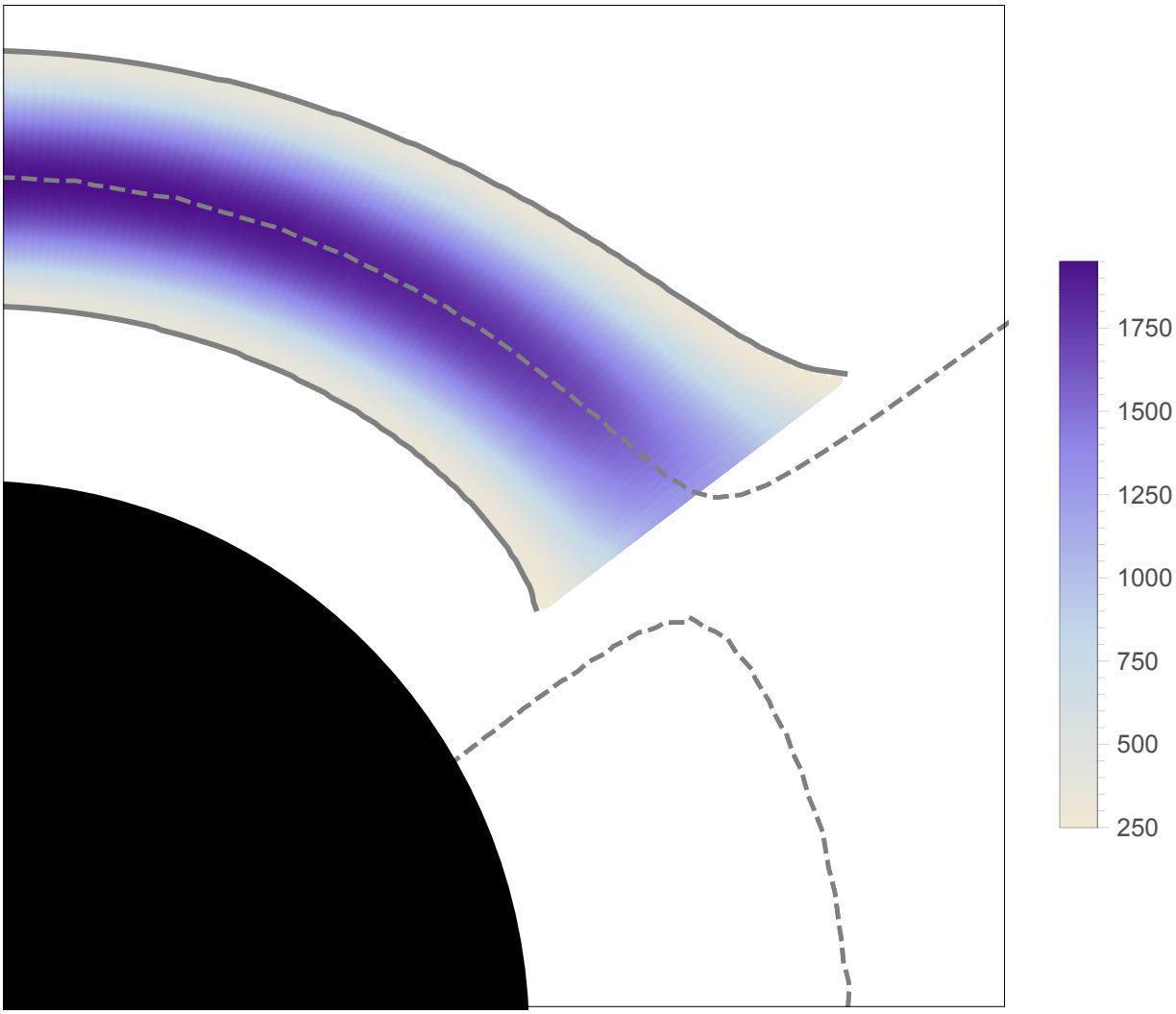

Figure 6.1: Lorentz factor versus polar angle. This solution is for a maximumly spinning black hole of mass, $10^7 M_\odot$ with a magnetic field strength of 10^4 Gauss and an ambient energy density of 10^6 ergs/cm^3.

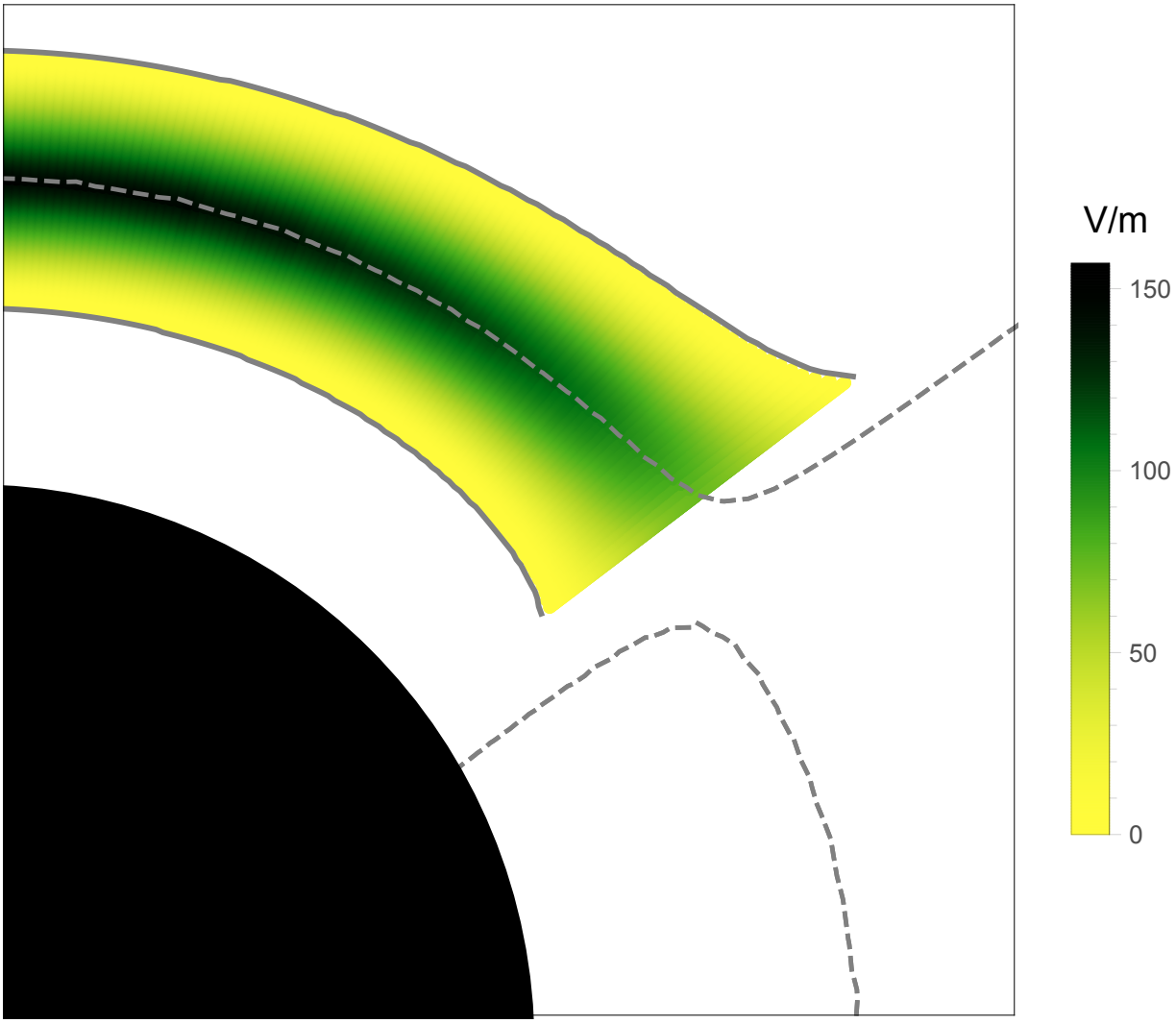

Figure 6.2: The parallel electric field versus polar angle. This solution is for a maximumly spinning black hole of mass, $10^7 M_\odot$ with a magnetic field strength of 10^4 Gauss and an ambient energy density of 10^6 ergs/cm^3.

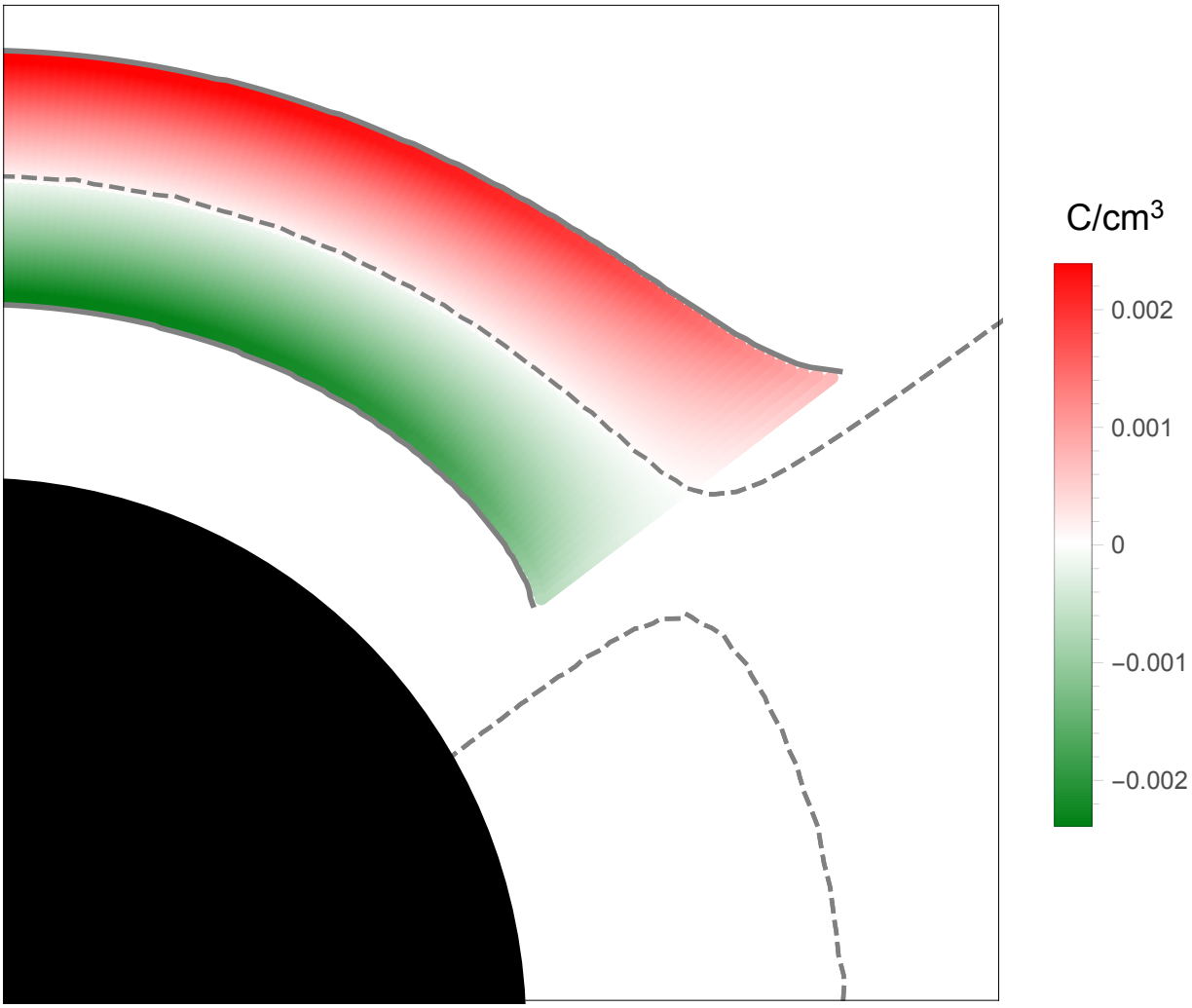

Figure 6.3: The charge density versus polar angle. This solution is for a maximumly spinning black hole of mass, $10^7 M_\odot$ with a magnetic field strength of 10^4 Gauss and an ambient energy density of 10^6 ergs/cm^3.

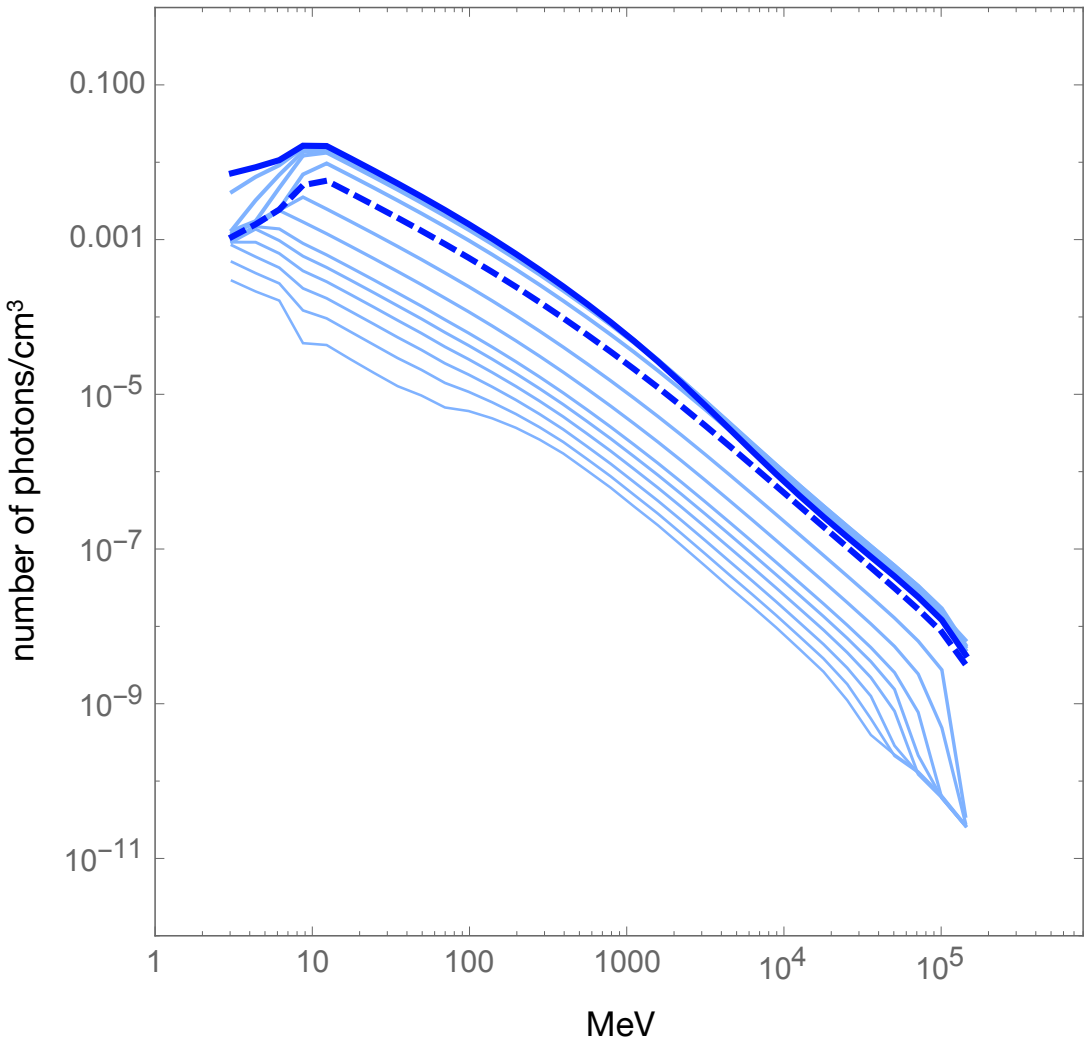

Figure 6.4: The spectral transition from the inner boundary of the gap through the center of the gap (bold dashed line) and the outer boundary of the gap (bold solid line). Starting at 12% of the gap width after the inner (closest to the black hole) boundary, 14 spectral lines are shown. The 8 lines under the dashed line are all equally spaced and from the inner side of the gap. The 4 lines between the dashed line and solid line are all from the outer part of the gap and equally spaced.

6.2 Adjustable Parameters

The model has four parameters that can be adjusted: the mass and spin of the black hole, the seed magnetic field, and the available background energy density. By changing the magnetic field, mass, or spin; the physical change to the model is in ρ_{GJ}. By changing the

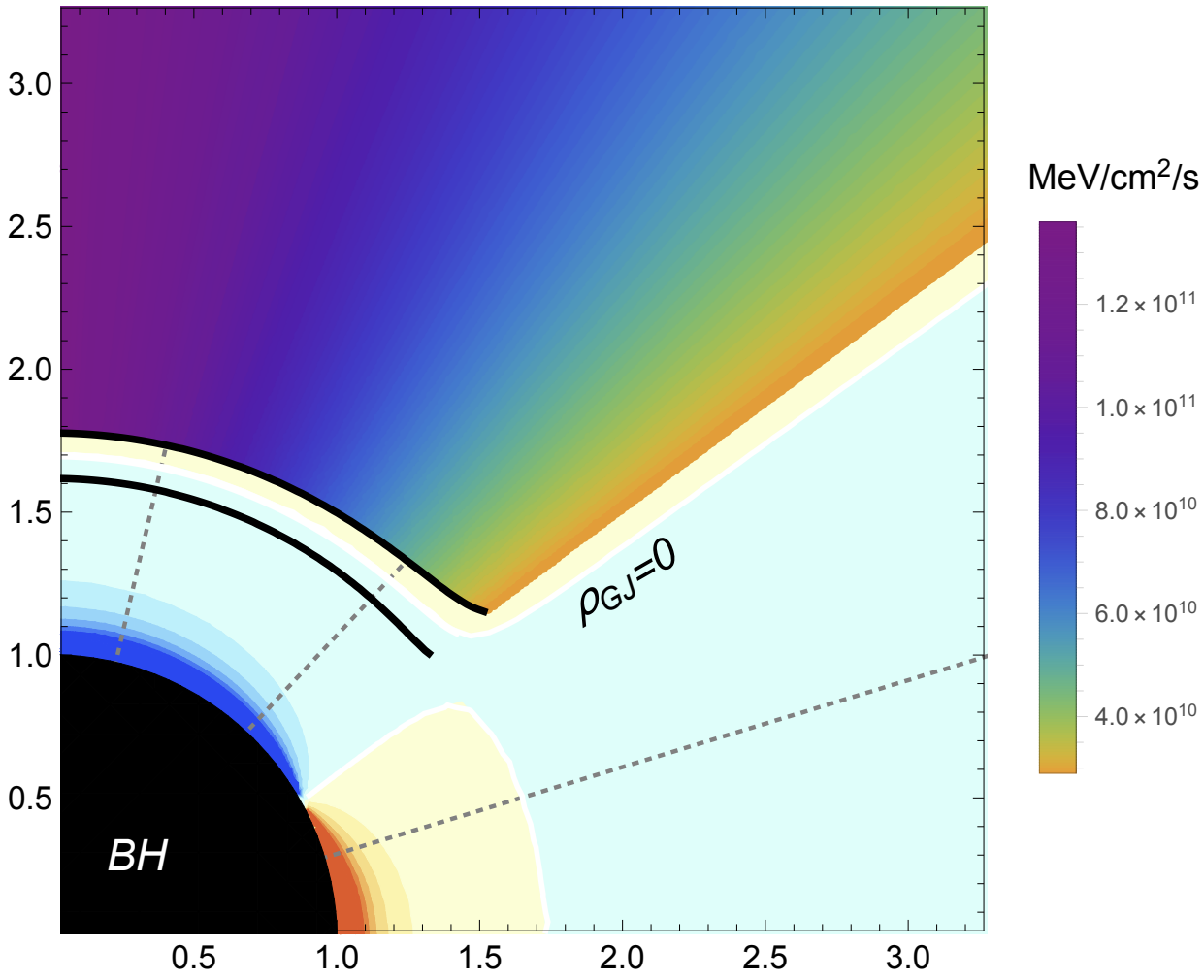

Figure 6.5: The outgoing energy flux from the up-scattered photons as a function of polar angle. This solution is for a black hole mass of $10^7 M_\odot$ with a magnetic field strength of 10^4 Gauss and an ambient energy density of 10^6 ergs/cm^3

background energy density, the physical changes to the model are in the angle-averaged pair production redistribution function and the Compton redistribution function. By changing these parameters one can gain insight into how they effect the different aspects of the cascade process, i.e., the gap width, the peak Lorentz factor, maximum electric field, etc.

Chapter 7

Mass

7.1 Varying the Black Hole Mass

Changing the mass of the black hole changes the ρ_{GJ}, and therefore, A_θ in the one dimensional model. Changing the mass and observing how the structure of the gap changes gives one insight into the conditions needed to produce AGN. Figure 7.2 shows how the size of the gap changes with mass and angle. The energy stored in the kinetic energy of the charges as a function of angle can be seen in Figure 7.1. These figures detail how the kinetic energy of the charges and the size of the gap relate. Normalizing the gap width and Lorentz factor to one at the axis of rotation (Figures 7.4 & 7.3), one can see that the mass is invariant with respect to θ, while the gap is thin. Overlaid on the results in Figures 7.1, 7.2, 7.3, 7.4, 7.6, & 7.7 are exponential fits as a function of θ. The fits are summarized in Table 7.1. These fits are useful, for example, in estimating the change in available energy as a function of inclination angle. Since the results are mass invariant, one can extrapolate these fits to any size black hole as long as the resulting gap width remains small. The gap half width as a function of θ is $H \propto e^{7.4\theta}$ (Ford et al., 2017). Figure 7.4 clearly illustrates how at large θ $\left(\sim \cos^{-1}\left\{1/\sqrt{3}\right\}\right.$, see Equation 3.31$\left.\right)$ the gap width increases up to ~ 1.7 times: its smallest width (at $\theta = 0$). The maximum Lorentz factor as a function of

θ is $\Gamma_{\max} \propto -e^{5.4\theta}$. As θ increases, the available kinetic energy in the gap drops by up to $\sim 50\%$ at large θ. Similarly, the maximum electric field strength's angular dependence is $E_{\max} \propto e^{7.4\theta}$ (Ford et al., 2017).

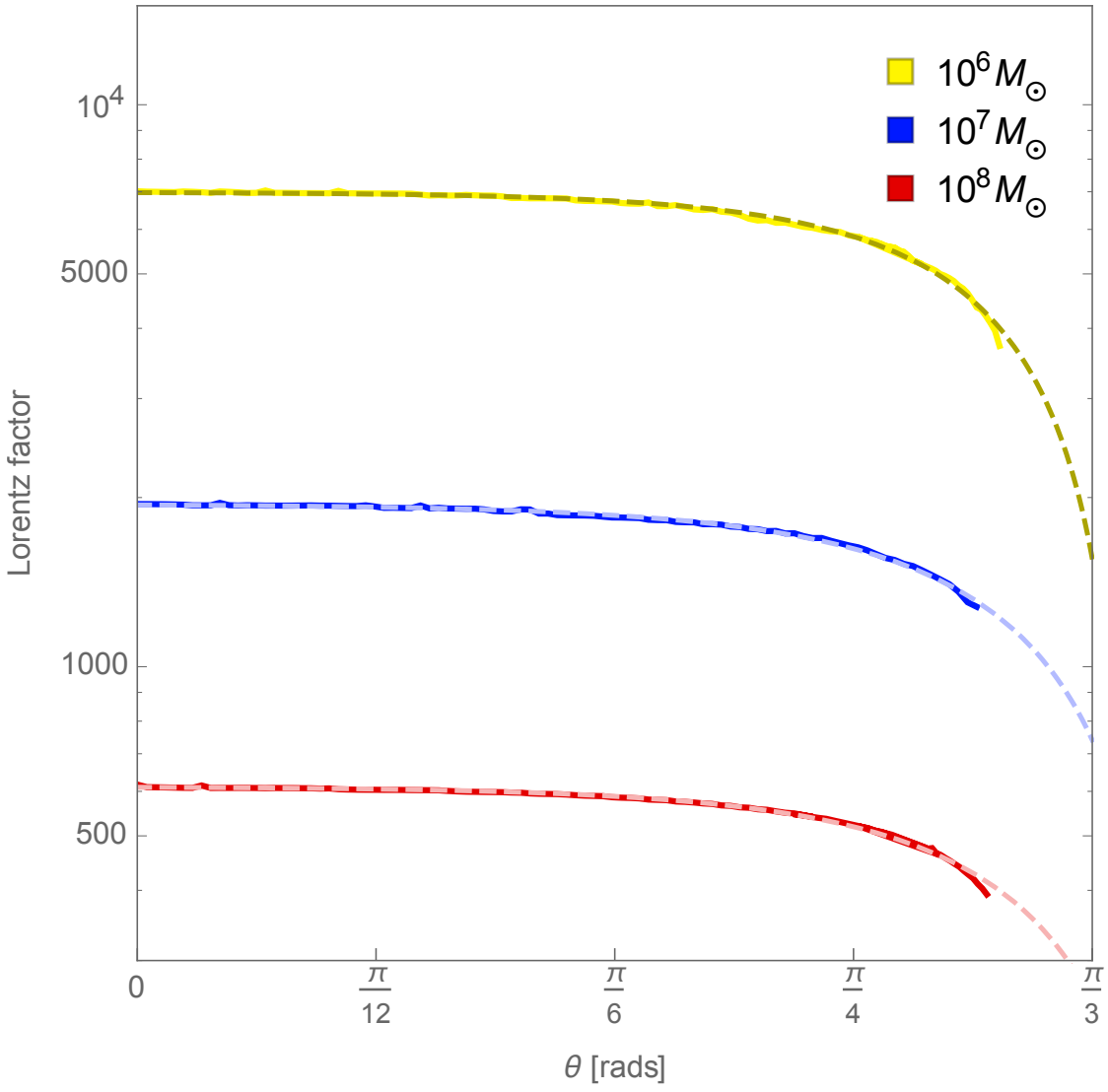

Figure 7.1: Lorentz factor versus polar angle. The three curves represent the change in Lorentz factor as polar angle increase going away from the axis of rotation for three different masses and their corresponding fits represented with dashed lines. From the top down the masses are $10^6 M_\odot$, $10^7 M_\odot$, and $10^8 M_\odot$. And similarly, the fits from the top down are $-11e^{5.9\theta} + 7.0\times10^3$, $-6.3e^{5.0\theta} + 1.9\times10^3$, and $-1.6e^{5.2\theta} + 6.1\times10^2$.

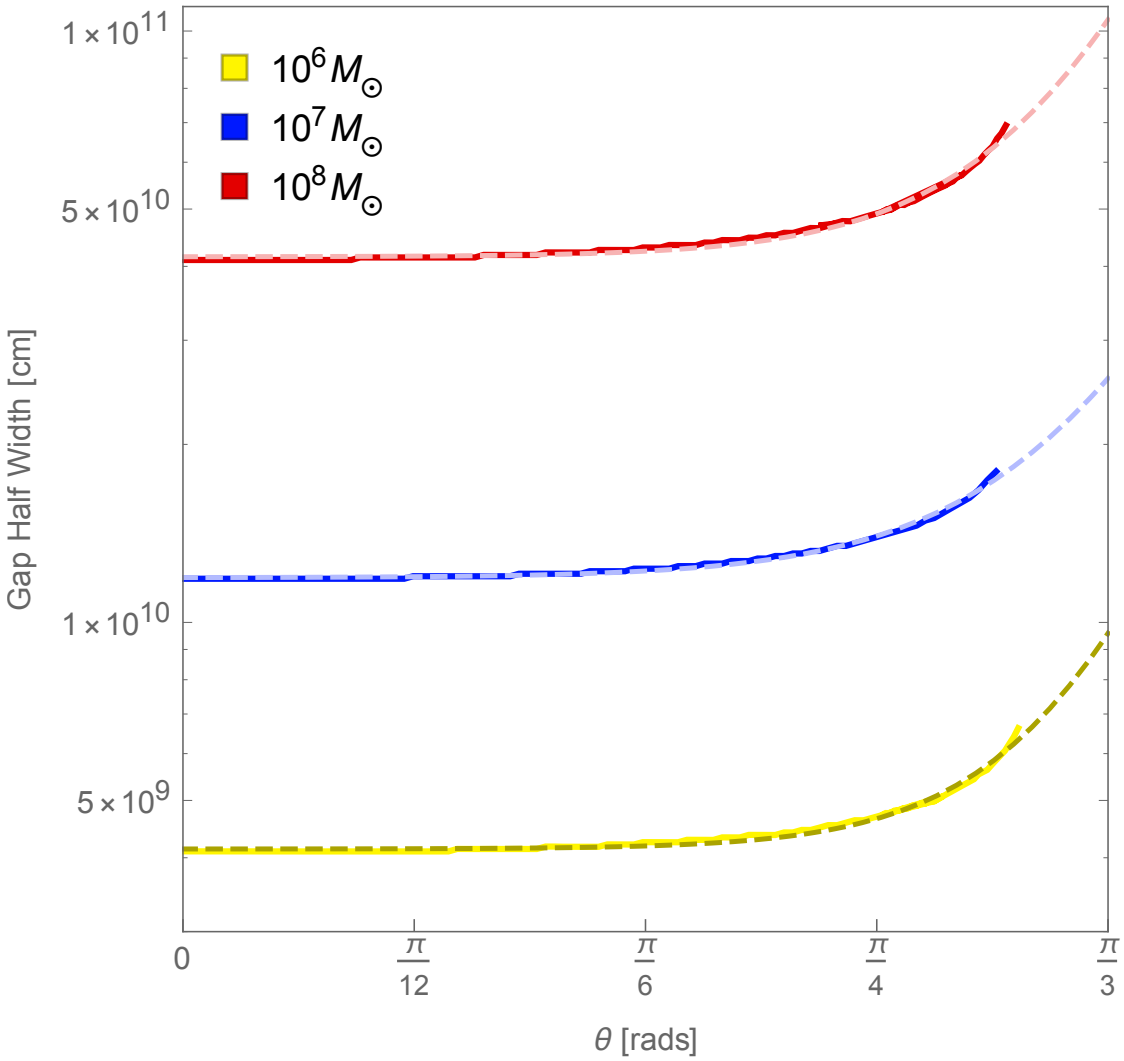

Figure 7.2: The width of half of the gap in centimeters versus polar angle. The three curves represent the change in the gap width as polar angle increase going away from the axis of rotations for three different masses and their corresponding fits represented with dashed lines. From the top down the masses are $10^8 M_\odot$, $10^7 M_\odot$, and $10^6 M_\odot$. And similarly, the fits from the top down are $1.3\times10^7 e^{8.1\theta} + 4.1\times10^{10}$, $7.1\times10^6 e^{7.2\theta} + 1.2\times10^{10}$, and $4.5\times10^5 e^{9.0\theta} + 4.1\times10^9$.

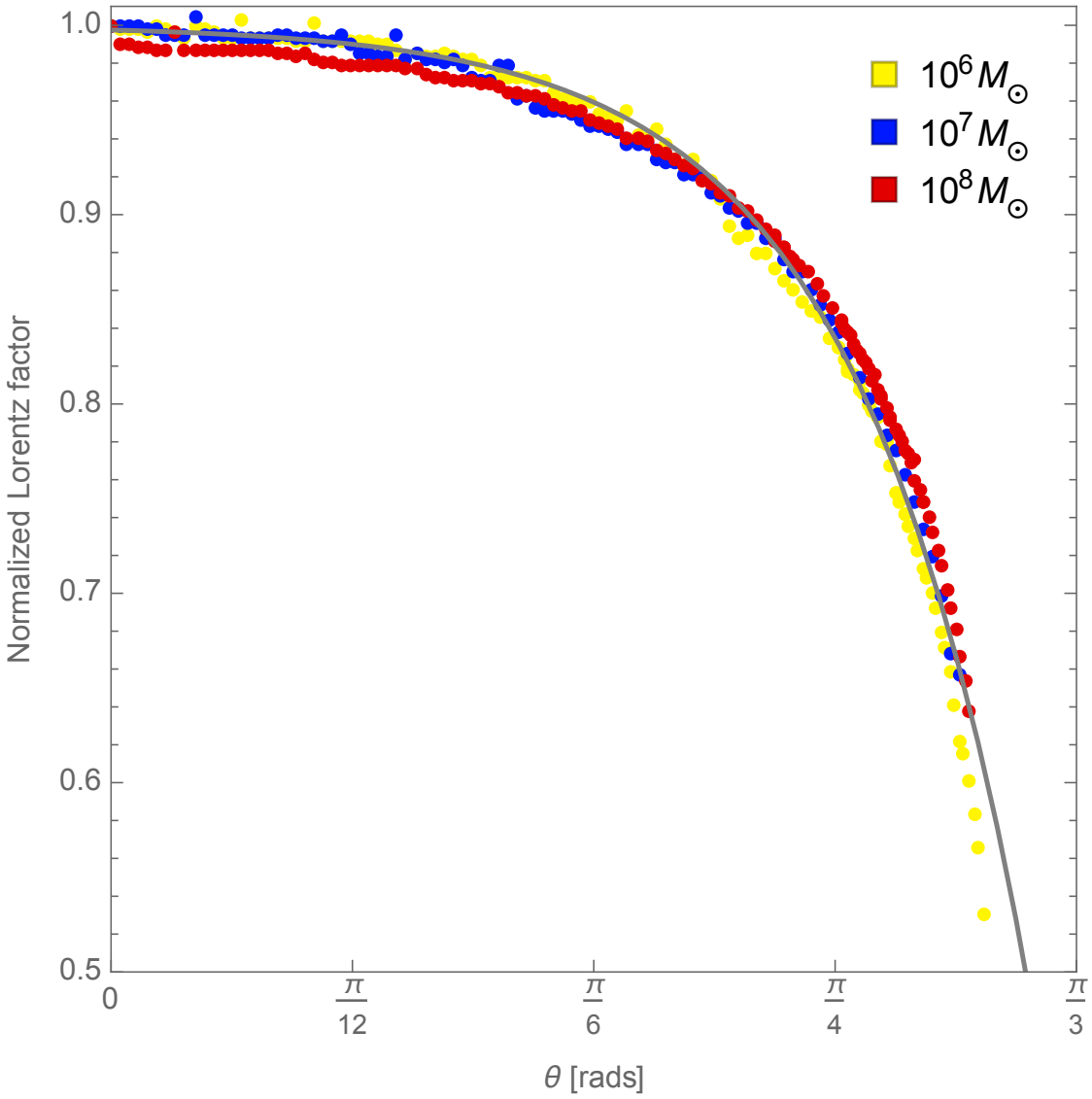

Figure 7.3: The Lorentz factor normalized at the axis of rotation versus the polar angle. An exponential fit of all three masses is $-2.5\times10^{-3}e^{5.4\theta}+1$. This demonstrates that for a thin gap the available kinetic energy as a function of polar angle is invariant relative to the mass of the black hole.

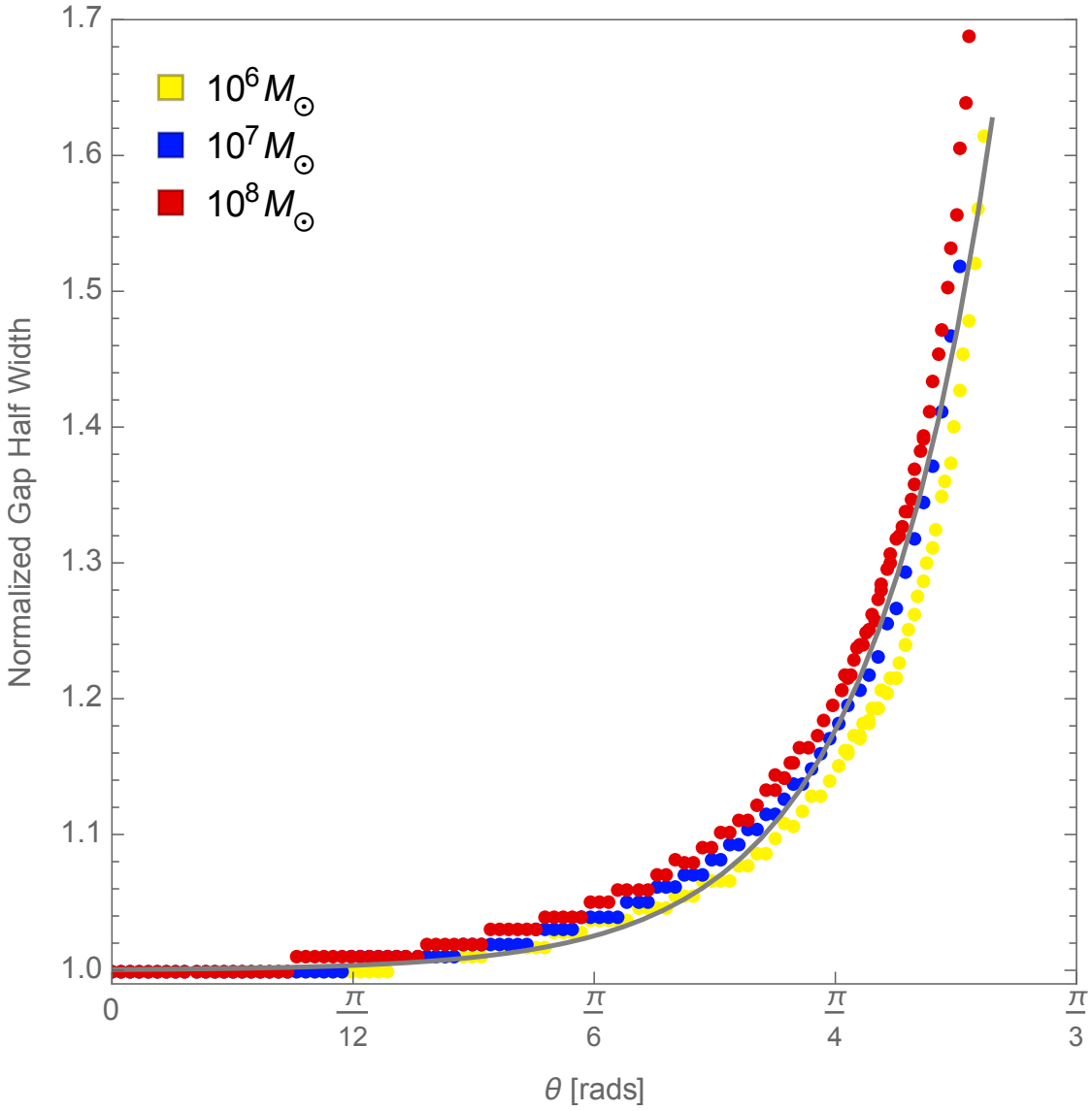

Figure 7.4: The width of half of the gap normalized at the axis of rotation versus the polar angle. An exponential fit of all three masses is $5.2\times10^{-4}e^{7.4\theta}+1$. This demonstrates that the efficiency of the cascade process as a function of polar angle, while the gap is thin, is invariant relative to the mass of the black hole.

Similarly, Figures 7.7 illustrates the drop off in outgoing photon energy flux as a function of θ, $\int F_\nu d\nu \propto -e^{4.2\theta}$ (Ford et al., 2017). As θ increases, the outgoing energy flux drops by almost 95% at large θ. Figure 7.5 shows the outgoing spectrum of the $gamma$-rays that were produced in the gap via inverse Compton scattering.

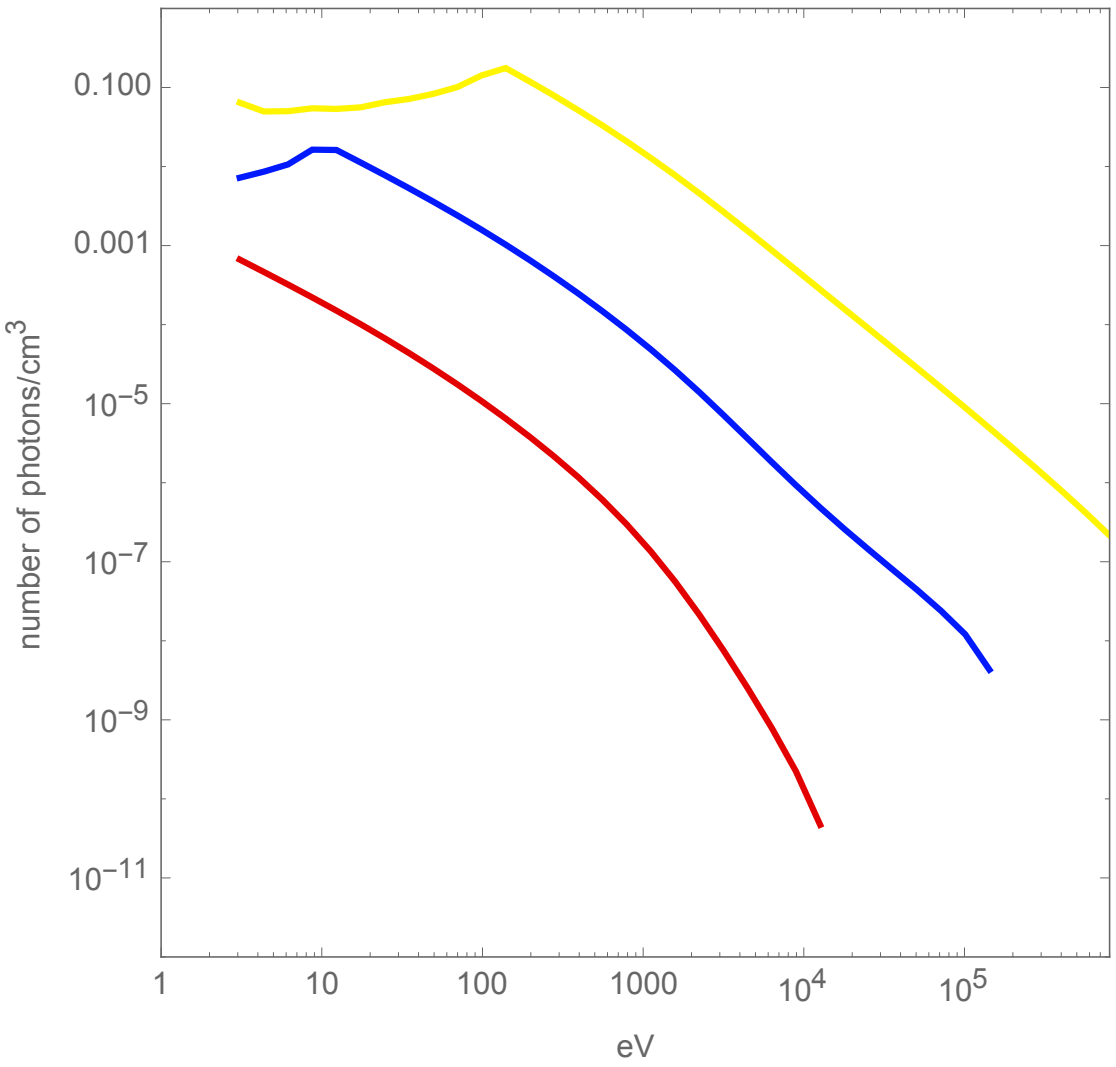

Figure 7.5: The outgoing spectrum for the different masses. From the top down the masses are $10^8 M_\odot$, $10^7 M_\odot$, and $10^6 M_\odot$.

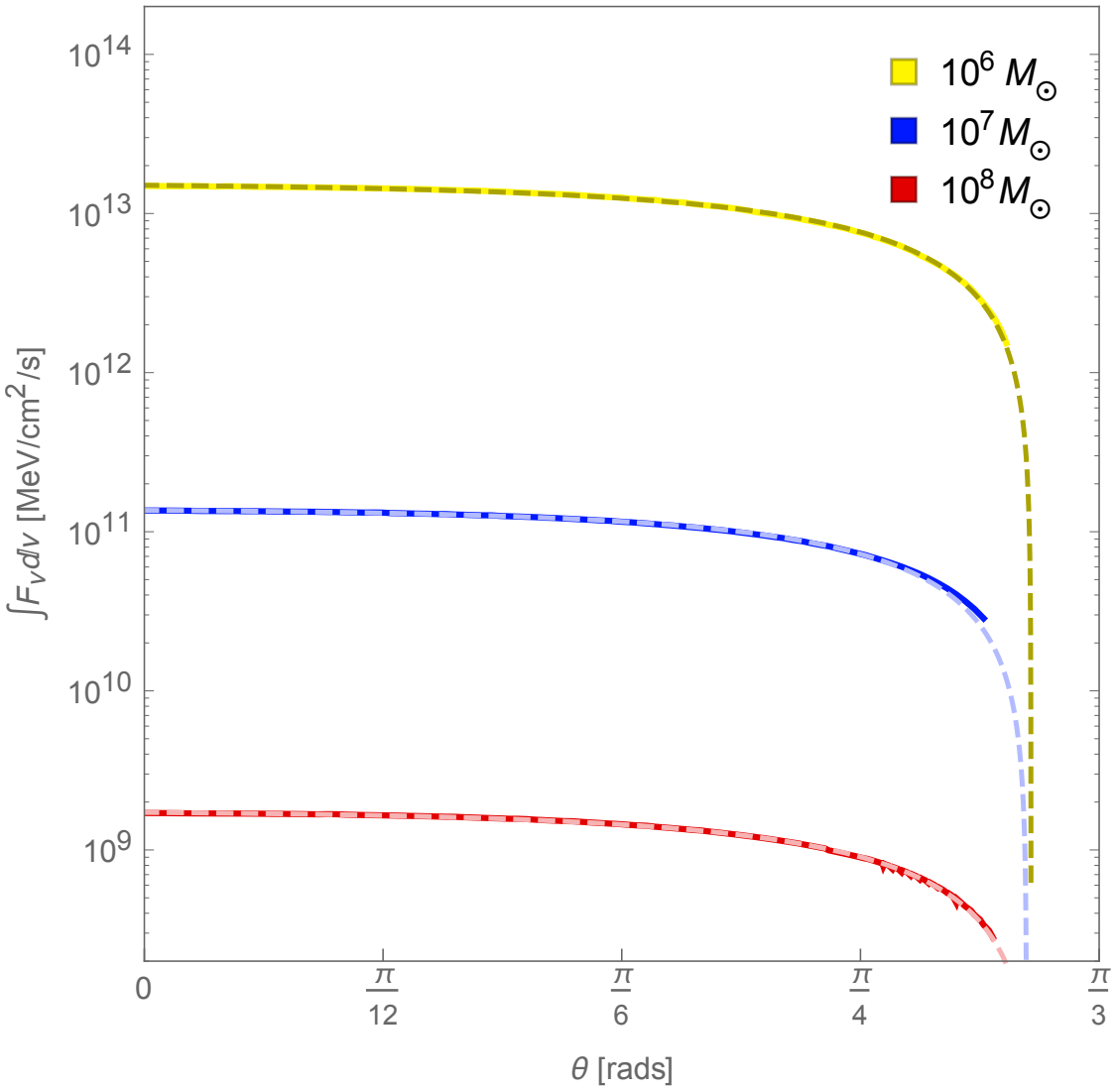

Figure 7.6: The total outgoing energy flux from the up-scattered photons versus polar angle. The three curves represent the change in the gap width as polar angle increase going away from the axis of rotations for three different masses and their corresponding fits represented with dashed lines. From the top down the masses are $10^6 M_\odot$, $10^7 M_\odot$, and $10^8 M_\odot$. And similarly, the fits from the top down are $1.5\times10^{13} - 4.5\times10^{11}e^{3.6\theta}$, $1.4\times10^{11} - 2.8\times10^{9}e^{4.0\theta}$, and $1.8\times10^{9} - 4.4\times10^{7}e^{3.8\theta}$.

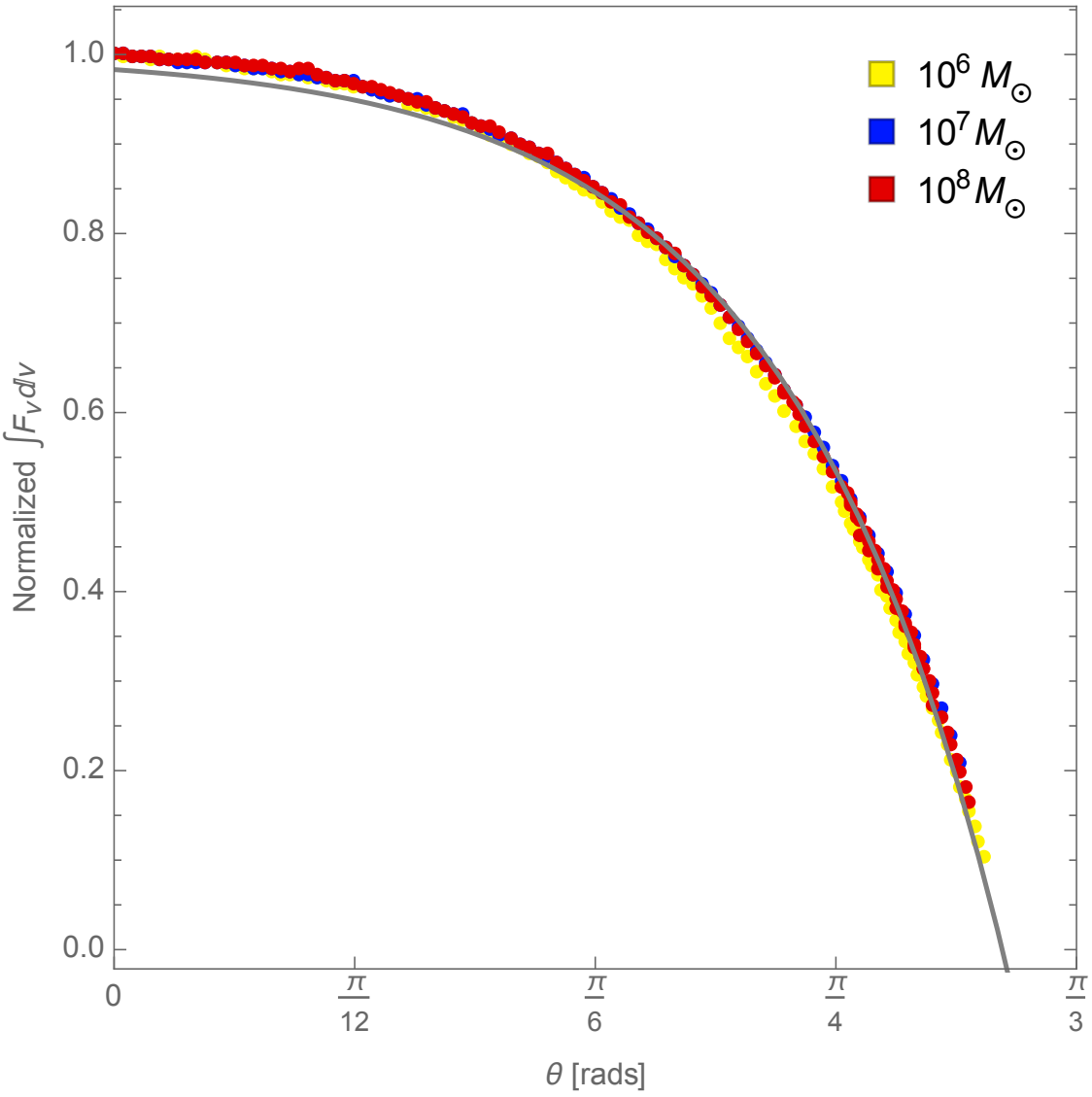

Figure 7.7: The outgoing photon energy density normalized at the axis of rotation versus the polar angle. An exponential fit of all three masses is $-1.7\times10^{-2}e^{4.2\theta}+1$. This demonstrates that for a thin gap the change in the outgoing energy flux as a function of theta scales with the mass of the black hole.

Figure 7.8 takes Figure 4.1 and overlays the gap for the varying black hole masses. This is to scale and shows how large the gap is with respect to the black hole environment.

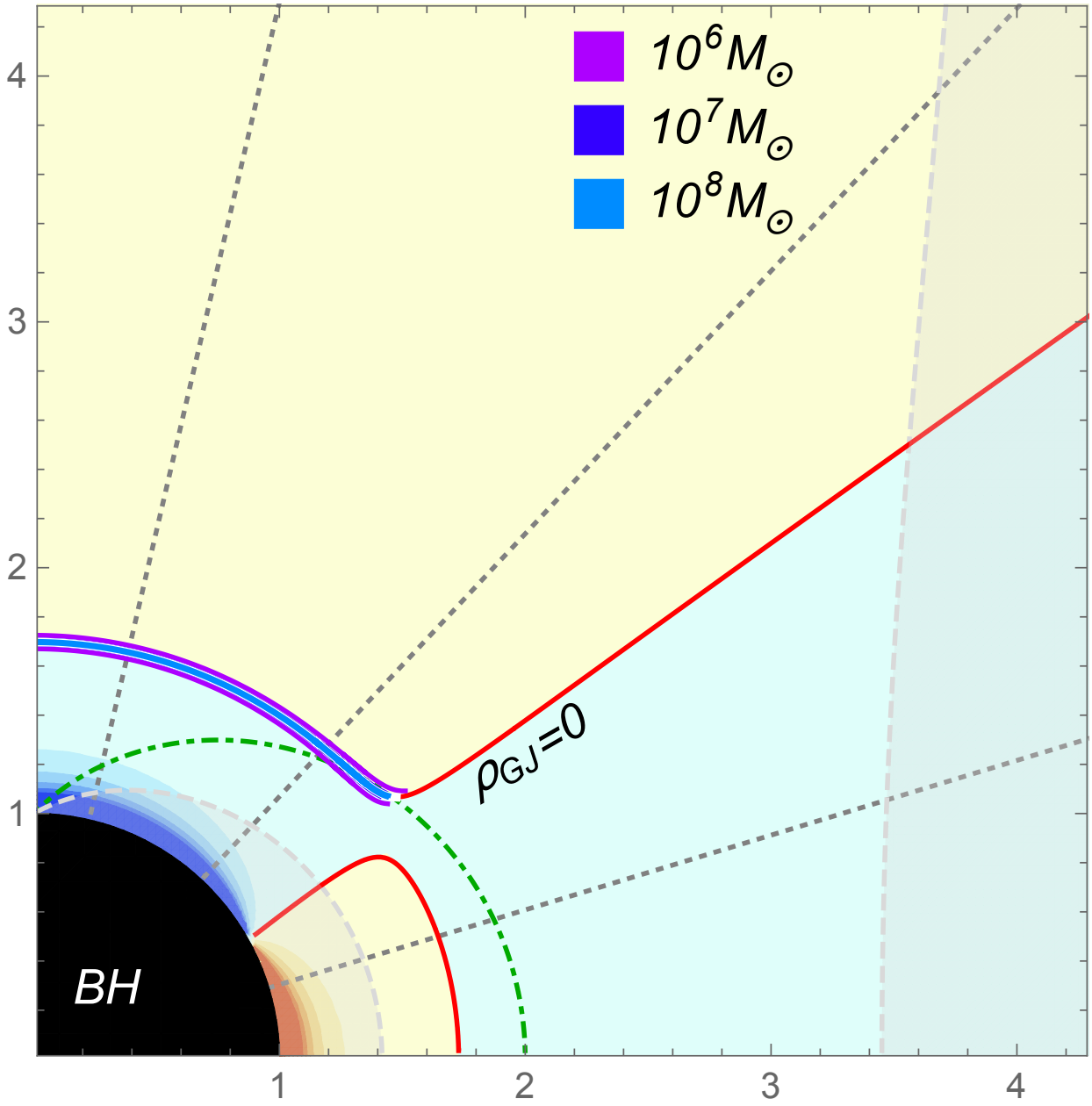

Figure 7.8: The black hole radius has been set to one and the gap widths are shown to scale. This is to illustrate the relative size of the gap to the black hole.

By increasing the gap width by an order of magnitude, Figure 7.9 illustrates the varying gap sizes with mass.

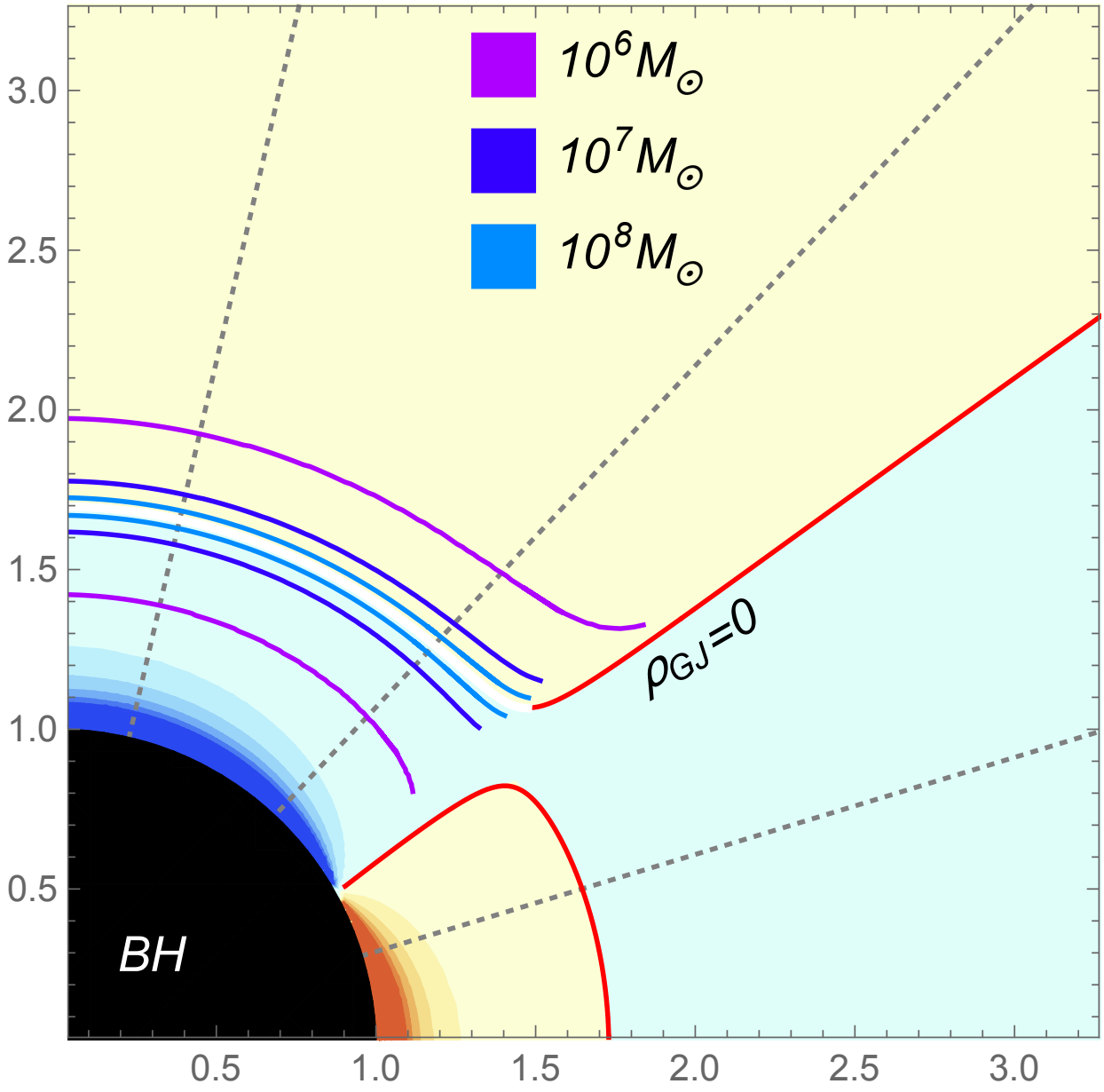

Figure 7.9: The black hole radius has been set to one and the gap widths have been increased by an order of magnitude for illustration. One can see that as the black hole mass decreases, the gap width with respect to the black hole radius increases. This is a sign that the plasma cascade is less efficient for lower mass black holes.

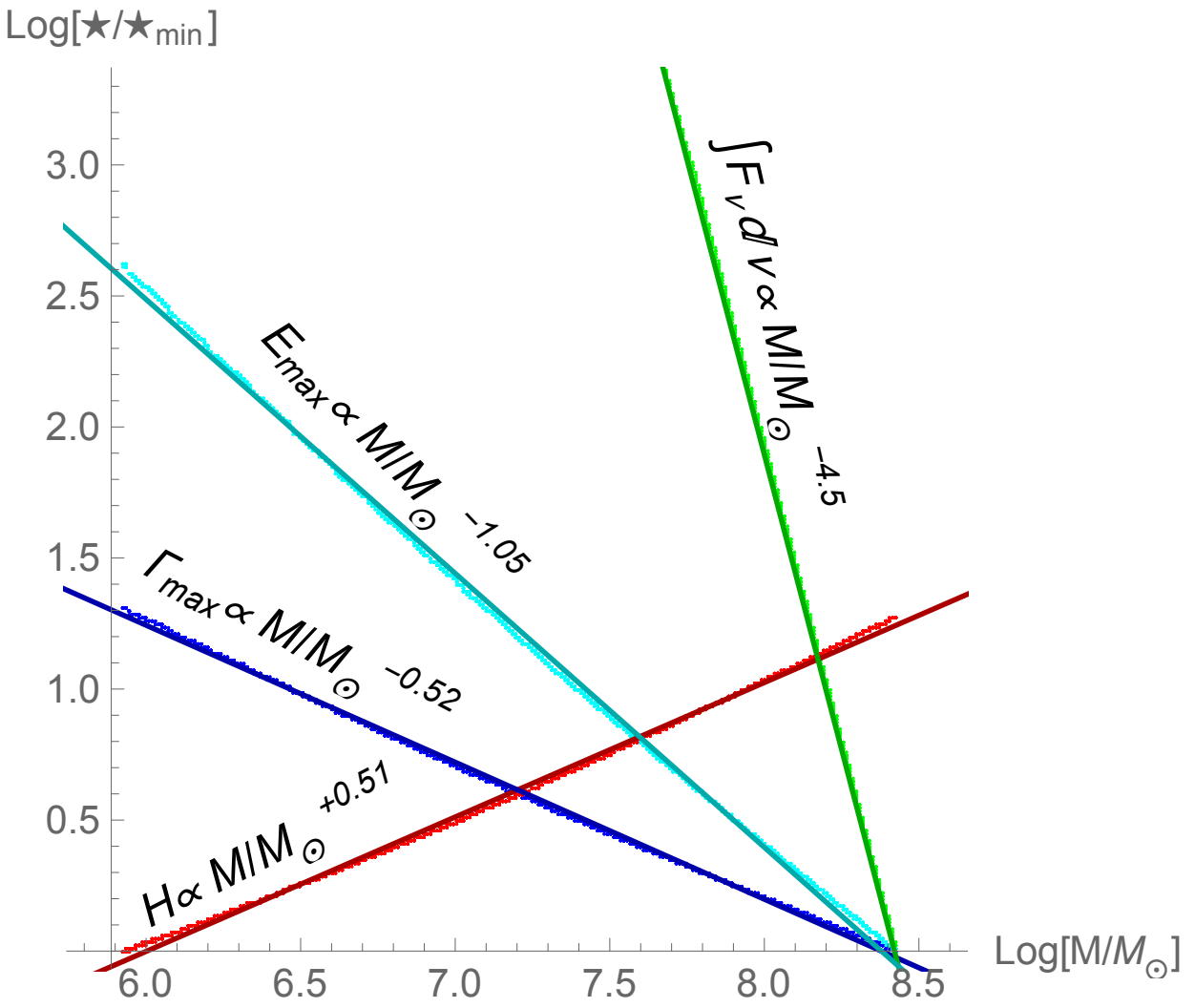

Figure 7.10: The ⋆ is a place holder that represents the maximum Lorentz factor, maximum electric field, gap width, and photon energy flux. Each physical quantity is normalized to it's minimum value and then plotted with respect to the mass of the black hole on a log-log scale.

After probing the structure of the gap over several orders of magnitude in black hole mass, one can find relationships between relevant physical parameters and black hole

mass:

$$
\begin{aligned}
H &= 3.2\times10^{6}\left[\frac{M}{M_{\odot}}\right]^{0.51}\ \mathrm{cm},\\
\Gamma_{\max} &= 9.2\times10^{6}\left[\frac{M}{M_{\odot}}\right]^{-0.52},\\
E_{\max} &= 3.5\times10^{9}\left[\frac{M}{M_{\odot}}\right]^{-1.05}\ \mathrm{V/m},\\
\int F_{\nu}d\nu &= 2.0\times10^{46}\left[\frac{M}{M_{\odot}}\right]^{-4.5}\ \mathrm{MeV/cm^{2}/s}.
\end{aligned}
\tag{7.1}
$$

Figure 7.10 shows these parameters plotted with respect to the mass of the black hole on a log-log scale after being normalized by their minimum value over the shown mass range. These relationships allow one to estimate the energy output, energy available, cascade efficiency, etc. for any maximumly spinning black hole embedded in a 10^4 Gauss magnetic field with an available background photon energy density of 10^6 ergs/cm^3.

Mass	Lorentz factor	Gap Half Width [cm]	Energy Flux [MeV/cm^2/s]
$10^6 M_\odot$	$7.0\times10^3 - 11e^{5.9\theta}$	$4.5\times10^5 e^{9.0\theta} + 4.1\times10^9$	$1.5\times10^{13} - 4.5\times10^{11} e^{3.6\theta}$
$10^7 M_\odot$	$1.9\times10^3 - 6.3e^{5.0\theta}$	$7.1\times10^6 e^{7.2\theta} + 1.2\times10^{10}$	$1.4\times10^{11} - 2.8\times10^9 e^{4.0\theta}$
$10^8 M_\odot$	$6.1\times10^2 - 1.6e^{5.2\theta}$	$1.3\times10^7 e^{8.1\theta} + 4.1\times10^{10}$	$1.8\times10^9 - 4.4\times10^7 e^{3.8\theta}$
all	$1 - 2.5\times10^{-3} e^{5.4\theta}$	$5.2\times10^{-4} e^{7.4\theta} + 1$	$1 - 1.7\times10^{-2} e^{4.2\theta}$

Table 7.1: Angular fits for the peak Lorentz factor, gap half width, and outgoing photon energy flux. These fits are shown on Figures 7.1, 7.2, 7.3, 7.4, 7.6, and 7.7.

Chapter 8

Seed Magnetic Field

8.1 Varying the Magnetic Field Strength

Varying the strength of the magnetic field around the black hole changes the ρ_{GJ}, and therefore, A_θ in the model. Changing the magnetic field strength and observing how the structure of the gap changes gives one insight into the conditions needed to produce AGN. Figure 8.2 shows how the size of the gap changes with magnetic field strength and polar angle. The energy stored in the kinetic energy of the charges versus θ can be seen in Figure 8.1. These figures detail how the kinetic energy of the charges and the size of the gap relate. Normalizing the gap width and Lorentz factor to one at the axis of rotation (Figures 8.4 & 8.3) one can see that the magnetic field strength is invariant with respect to angle, while the gap is thin. Overlaid on the results in Figures 8.1, 8.2, 8.3, 8.4, 8.6, & 8.7 are exponential fits as a function of θ. The fits are summarized in Table 8.1. These fits are useful, for example, in estimating the change in gap width as a function of inclination angle. Since the results are magnetic field invariant, one can extrapolate these fits to any magnetic field strength as long as the resulting gap width remains small. The gap width as a function of θ is $H \propto e^{5.3\theta}$ (Ford et al., 2017). Figure 8.4 clearly illustrates how at large θ the gap width increases up to ~ 1.6 times: its smallest width (at $\theta = 0$). The maximum

Lorentz factor as a function of θ is $\Gamma_{\max} \propto -e^{6.8\theta}$ (Ford et al., 2017). As θ increases, the available kinetic energy in the gap drops by $\sim 35\%$ at large θ. Similarly, the maximum electric field strength's angular dependence is $E_{\max} \propto -e^{4.7\theta}$.

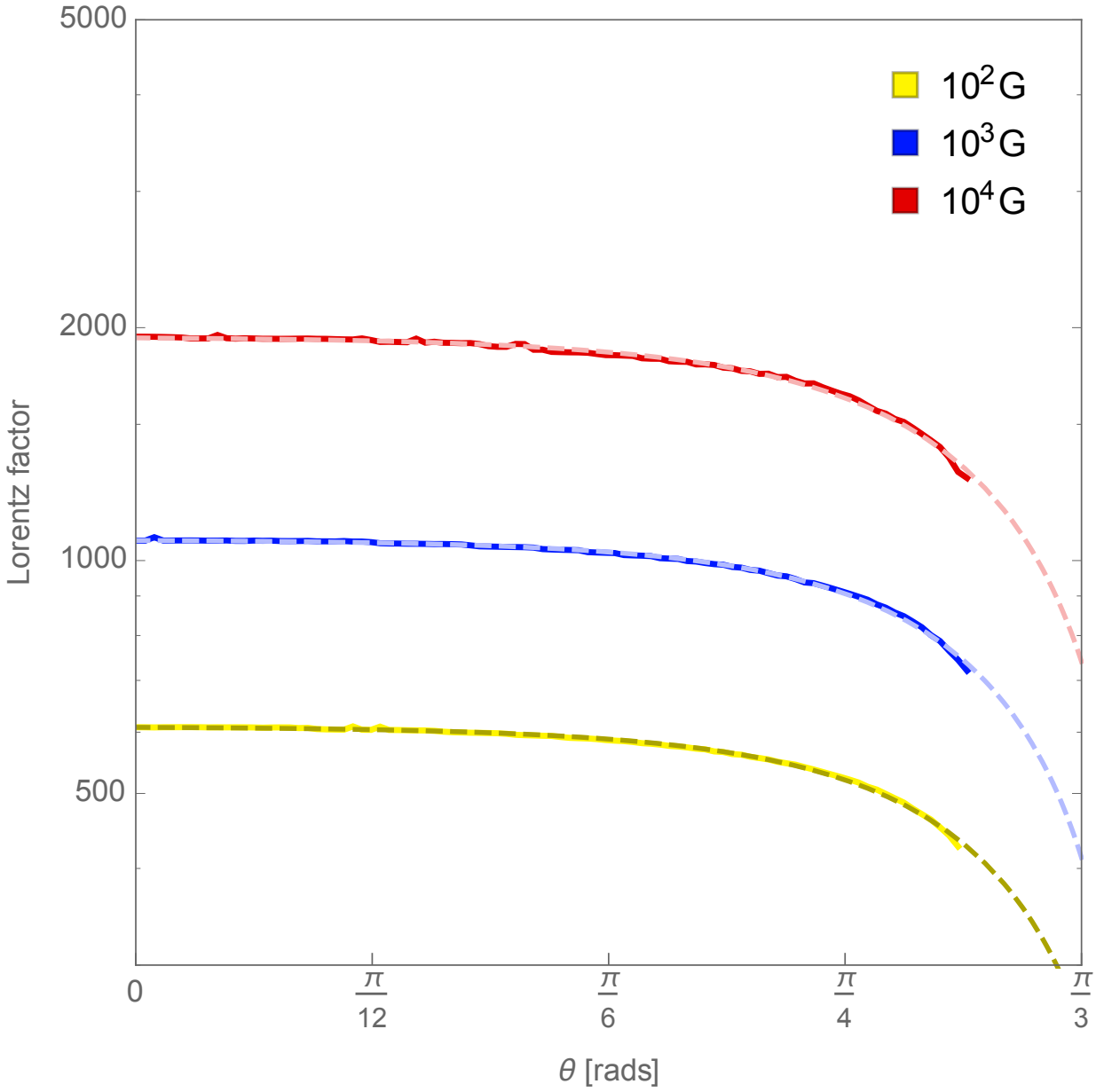

Figure 8.1: Lorentz factor versus polar angle. The three curves represent the change in Lorentz factor as polar angle increase going away from the axis of rotations for three different magnetic fields. From the top down the magnetic field strengths are 10^4G, 10^3G, and 10^2G. And similarly, the fits from the top down are $-6.3e^{5.0\theta}+2.0\times10^3$, $-2.2e^{5.4\theta}+1.0\times10^3$, and $-1.4e^{5.3\theta}+6.1\times10^2$.

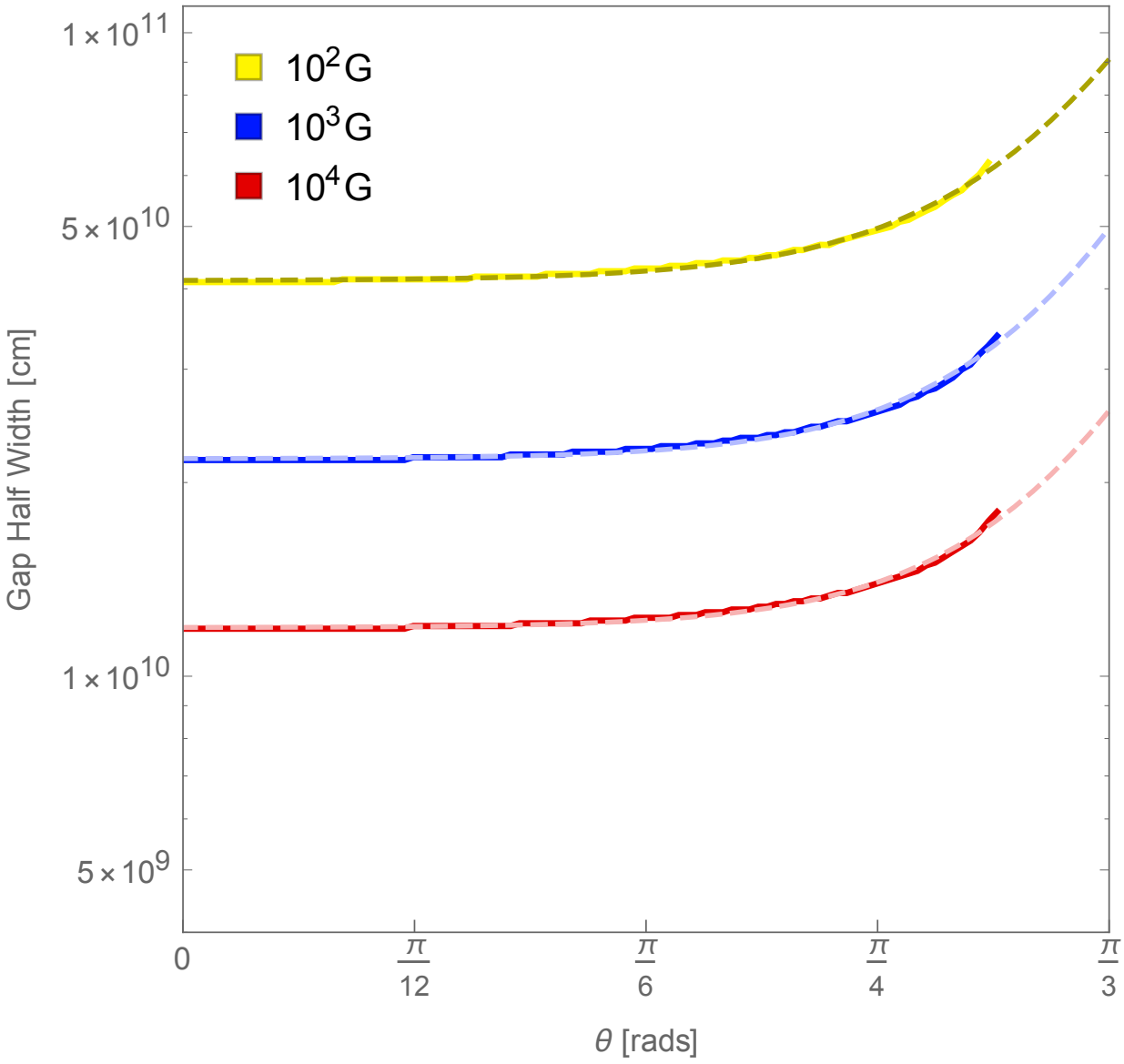

Figure 8.2: The width of half of the gap in centimeters versus polar angle. The three curves represent the change in the gap width as polar angle increase going away from the axis of rotations for three different magnetic field. From the top down the magnetic field strengths are 10^2G, 10^3G, and 10^4G. And similarly, the fits from the top down are $4.2\times10^7 e^{6.8\theta}+4.1\times10^{10}$, $1.4\times10^7 e^{7.3\theta}+2.2\times10^{10}$, and $7.1\times10^6 e^{7.2\theta}+1.2\times10^{10}$.

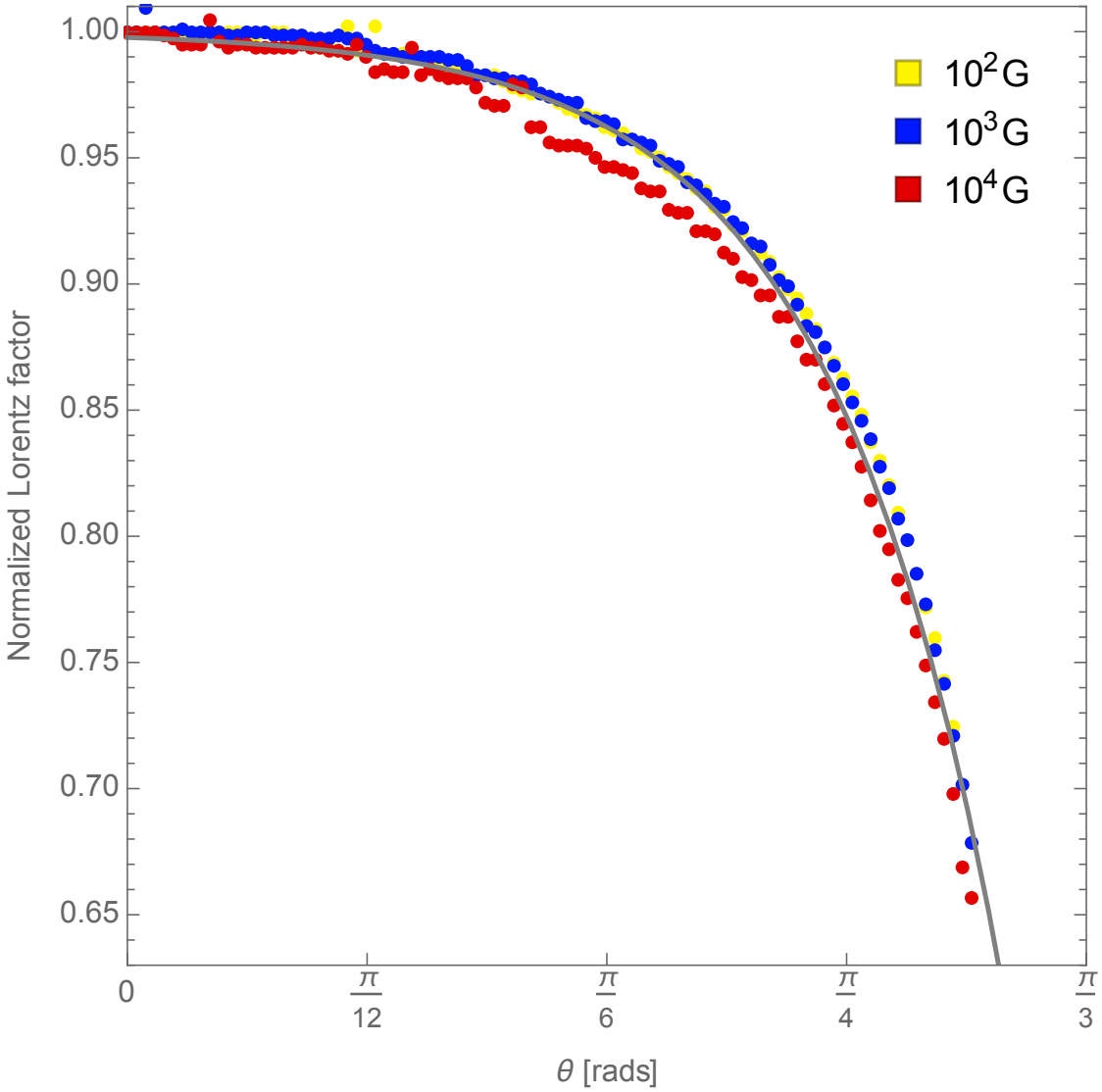

Figure 8.3: The Lorentz factor normalized at the axis of rotation versus the polar angle. An exponential fit of all three magnetic field strengths is $-2.3\times10^{-3}e^{6.8\theta}+1$. This demonstrates how the available kinetic energy in the gap versus angle scales with the magnetic field strength around the black hole.

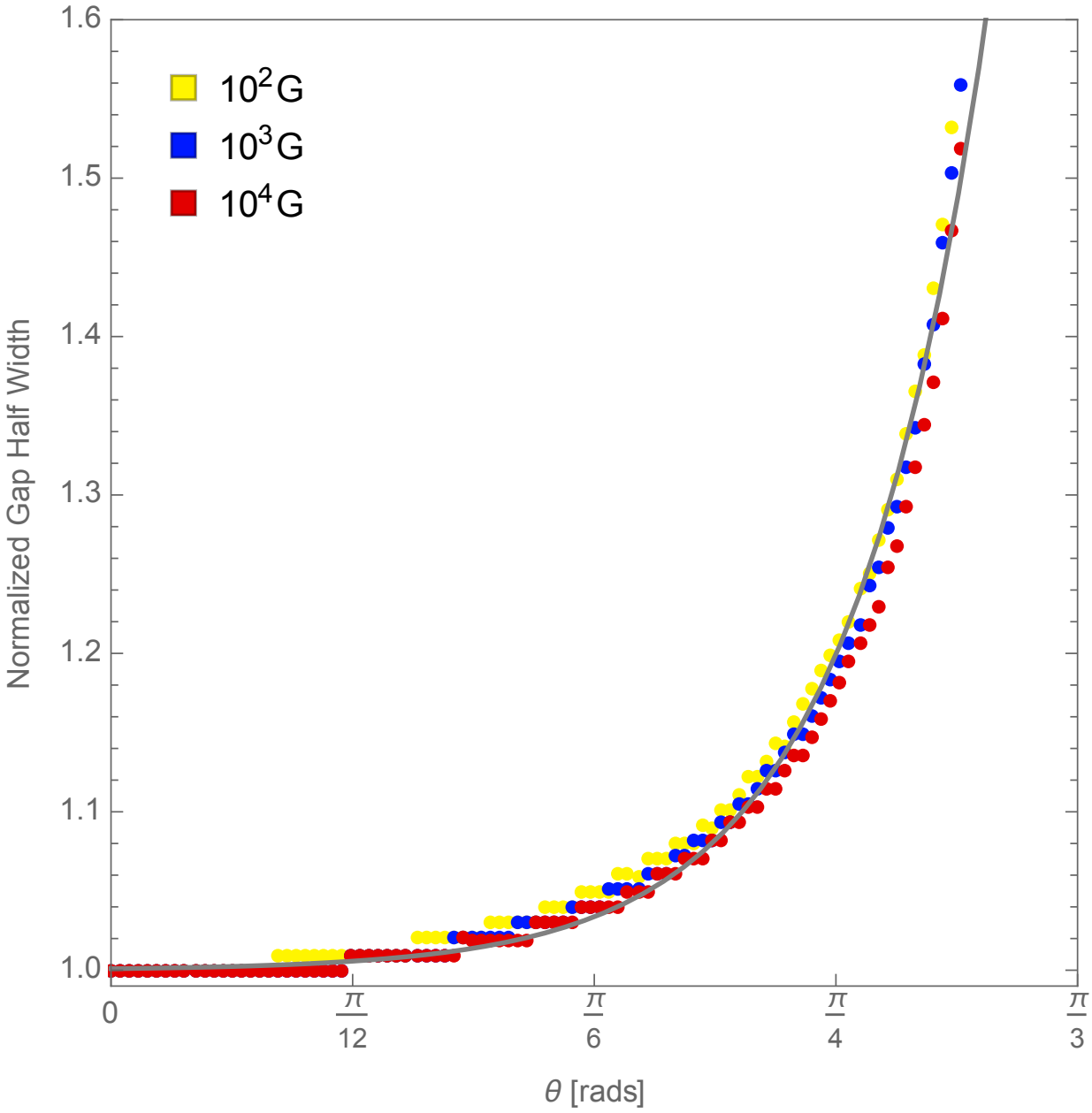

Figure 8.4: The width of half of the gap normalized at the axis of rotation versus the polar angle. An exponential fit of all three magnetic field strengths is $1.0\times10^{-4}e^{5.3\theta}+1$. This demonstrates that for a thin gap the seed magnetic field strength is invariant relative to the efficiency of the cascade process as a function of θ.

Figure 8.6 illustrates the drop off in outgoing photon energy flux as a function of θ, $\int F_\nu d\nu \propto -e^{4.5\theta}$. As θ increases the outgoing energy flux drops by almost 95% at large θ. Figure 8.5 shows the spectrum of the outgoing γ-rays at the edge of the gap.

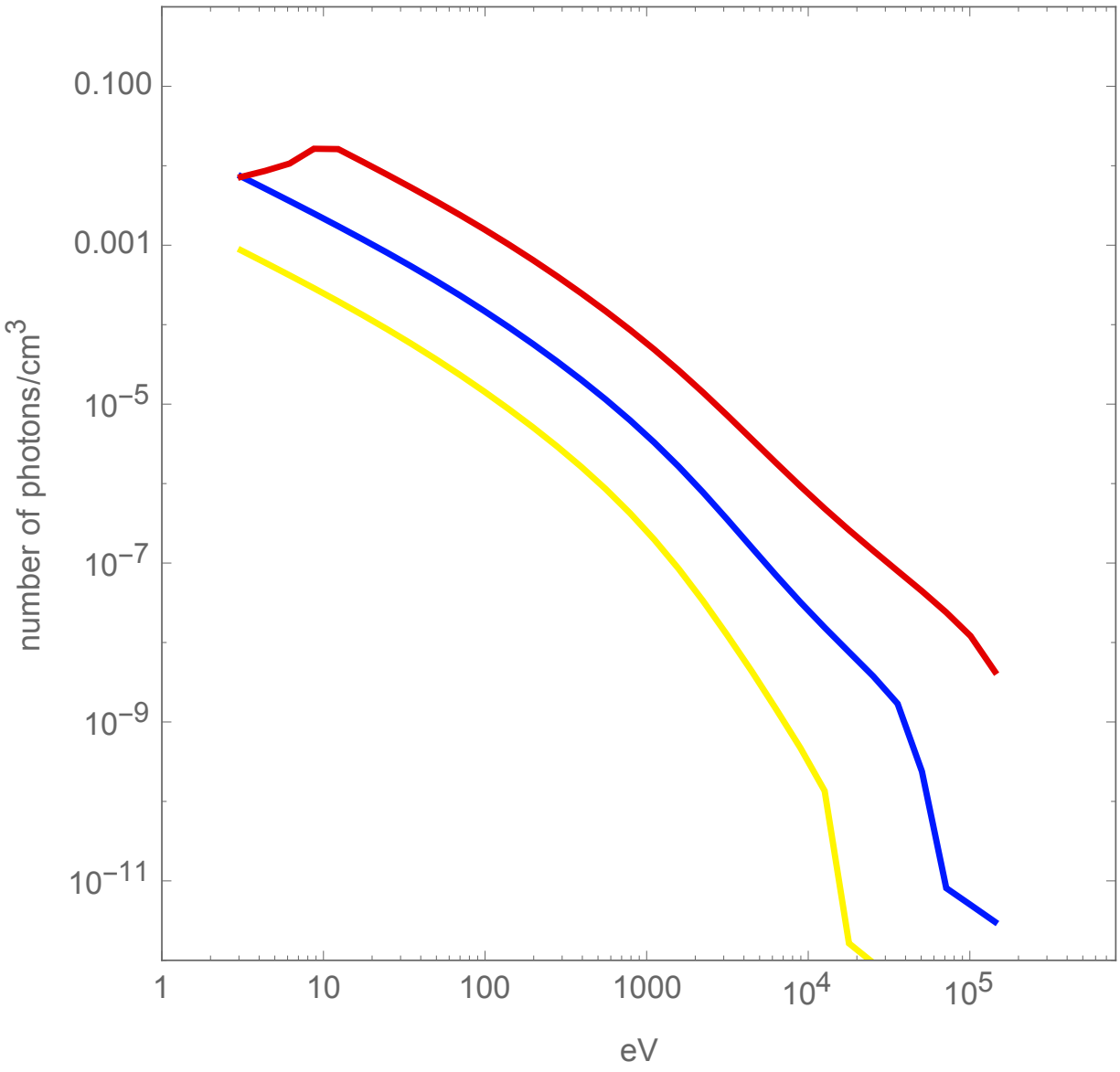

Figure 8.5: The outgoing spectrum for the different magnetic field strengths. From the top down they are 10^4 G, 10^3 G, and 10^2 G.

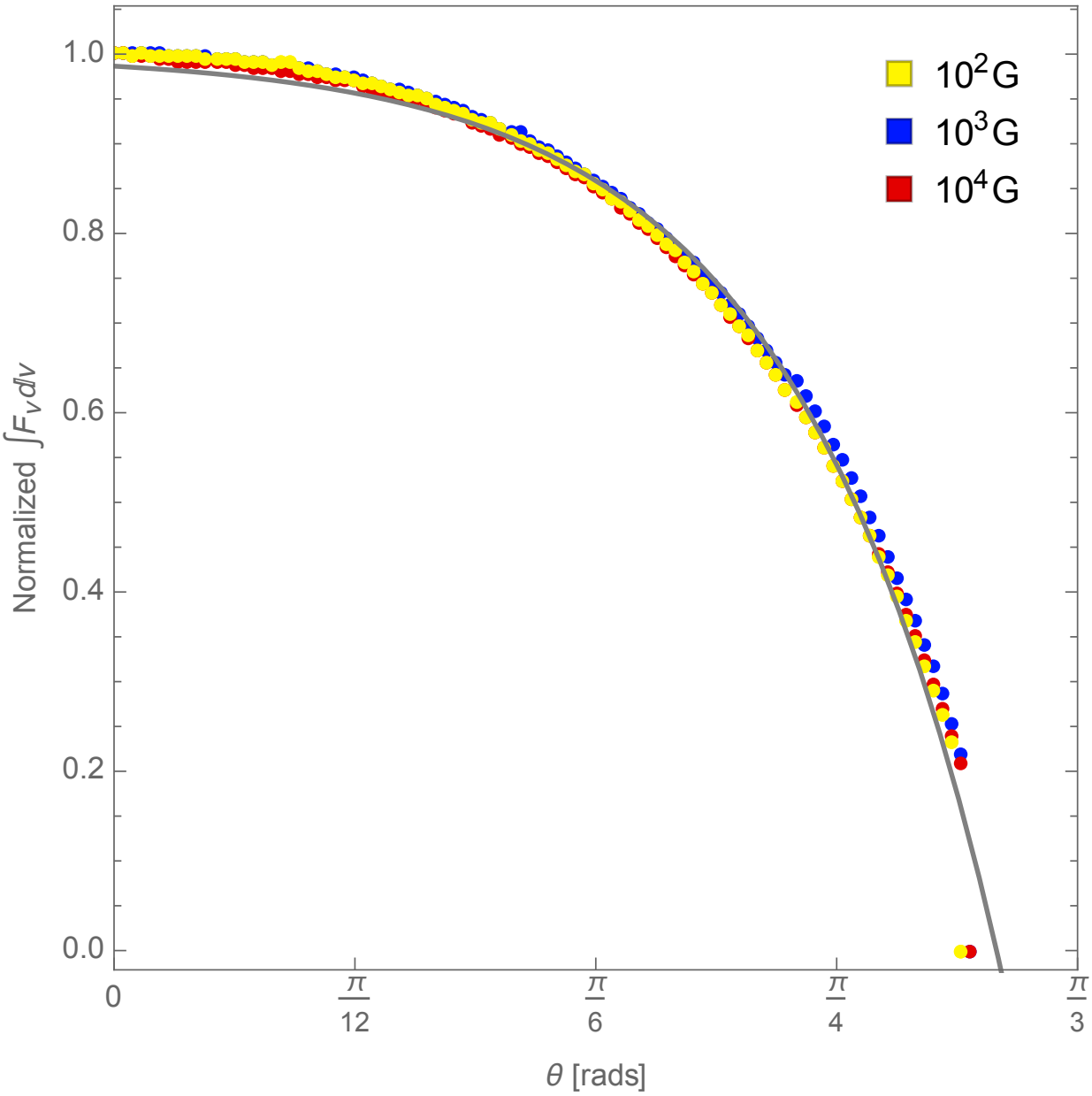

Figure 8.6: The outgoing photon energy density normalized at the axis of rotation versus the polar angle. An exponential fit of all three magnetic fields is $1 - 0.013e^{4.5\theta}$.

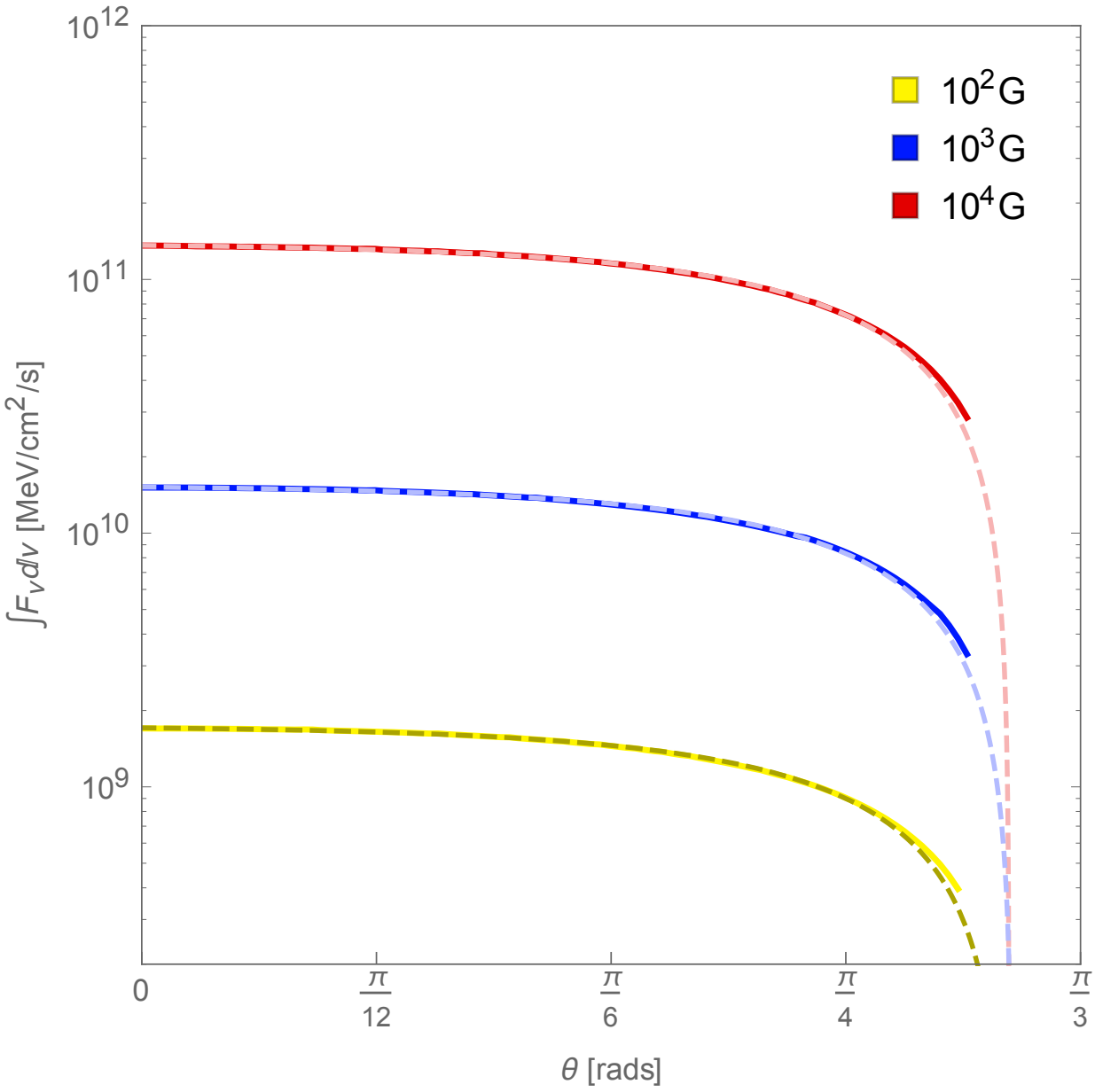

Figure 8.7: The total outgoing energy flux from the up-scattered photons versus polar angle. The three curves represent the change in the gap width as polar angle increase going away from the axis of rotations for three different magnetic field strengths and their corresponding fits, represented with dashed lines. From the top down the magnetic field strengths are 10^4 G, 10^3 G, and 10^2 G. And similarly, the fits from the top down are for 10^2G is $1.7\times10^9 - 3.3\times10^7 e^{4.1\theta}$, for 10^3G is $1.6\times10^{10} - 2.7\times10^8 e^{4.2\theta}$, and for 10^4G is $1.4\times10^{11} - 2.8\times 10^9 e^{4.0\theta}$.

Figure 8.8 illustrates the varying gap size with seed magnetic field strength by overlaying the different gaps widths increased by an order of magnitude on Figure 4.1.

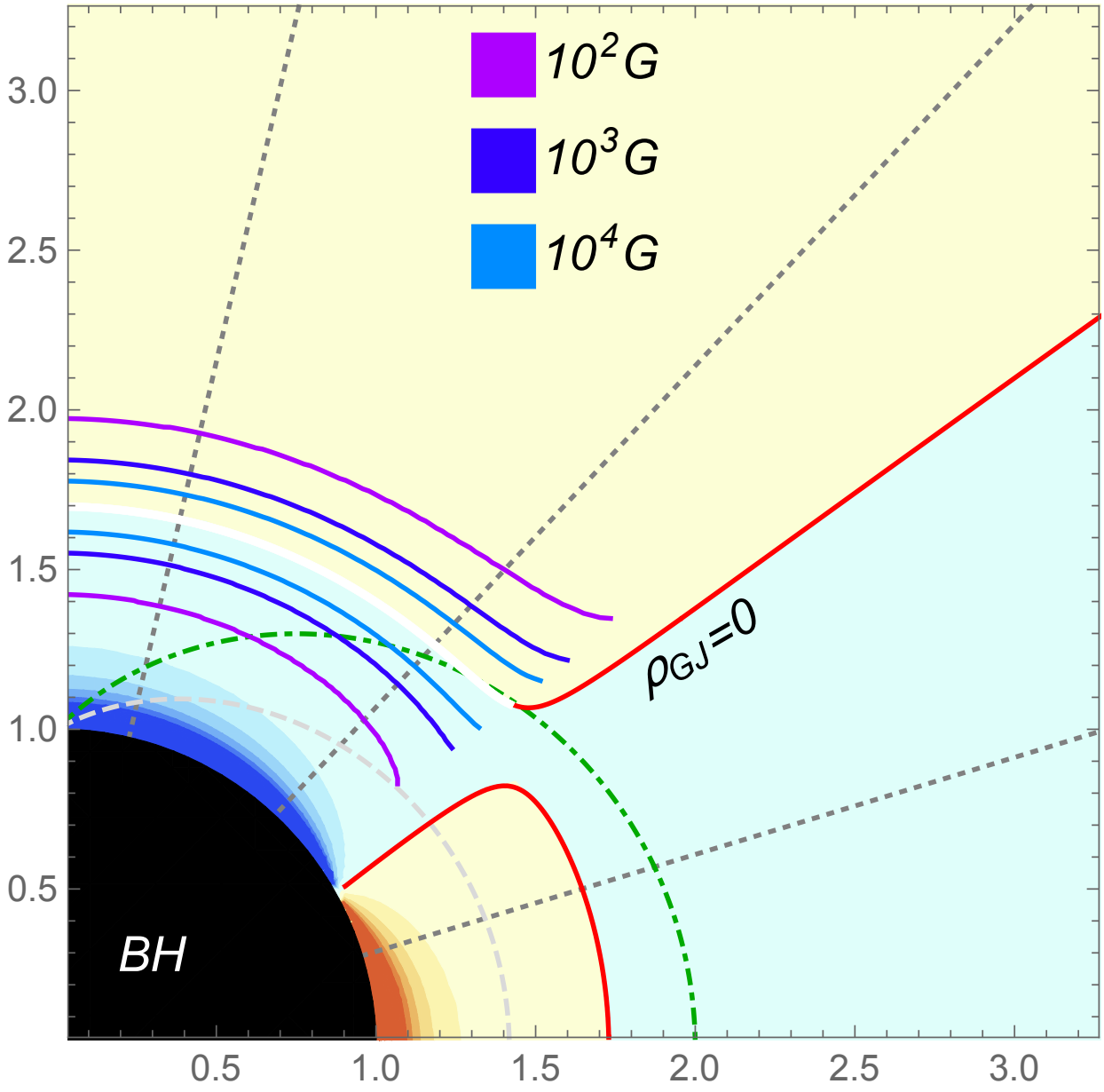

Figure 8.8: The black hole radius has been set to one, and the gap widths have be increase by an order of magnitude for illustration. One can see that as the magnetic field decreases the gap width with respect to the black hole radius increases. This is a sign that the plasma cascade is more efficient for strong magnetic fields.

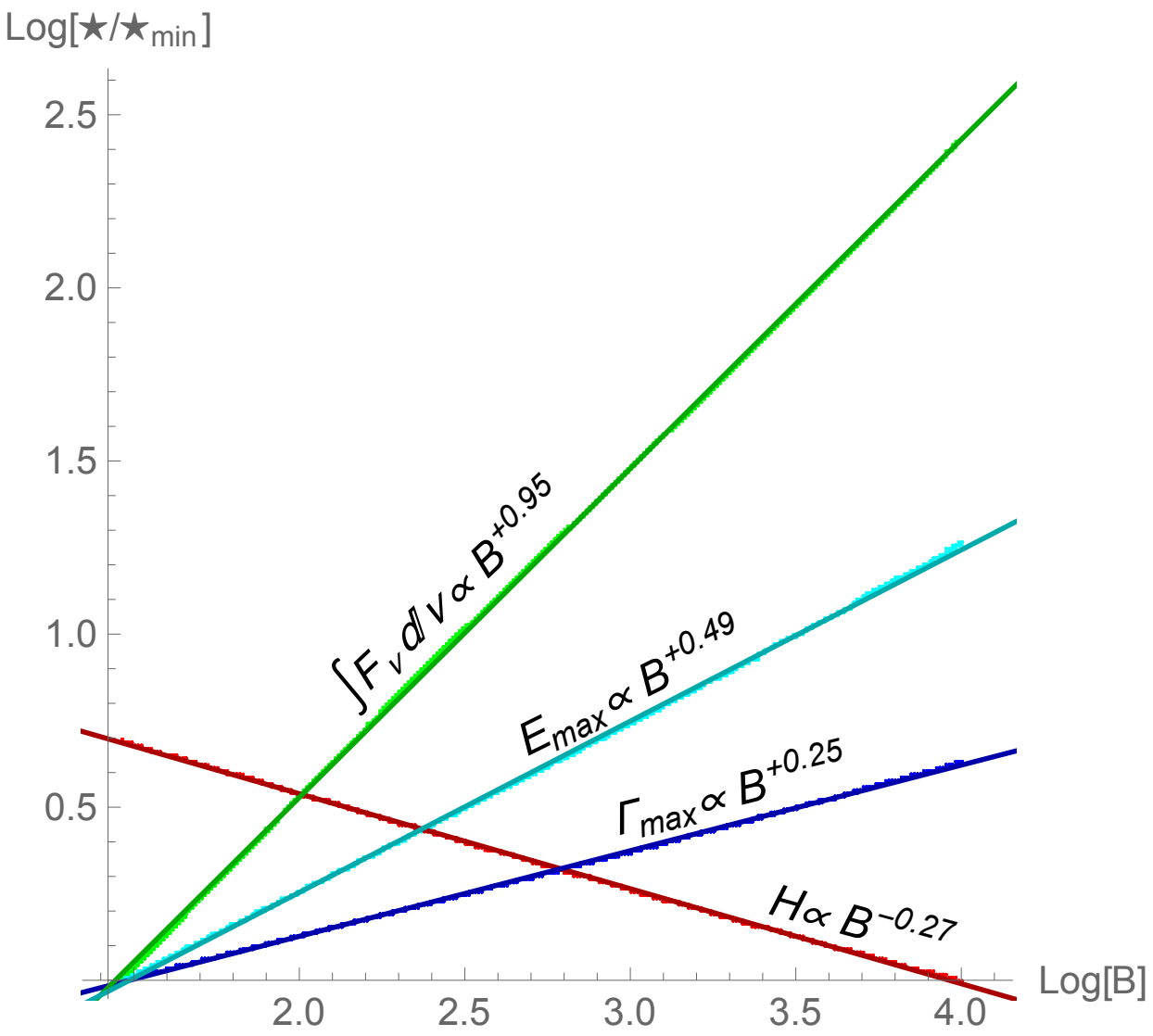

Figure 8.9: The ⋆ is a place holder that represents the maximum Lorentz factor, maximum electric field, gap width, and photon energy flux. Each physical quantity is normalized to its minimum value and then plotted with respect to the magnetic field strength on a log-log scale.

After probing the structure of the gap over several orders of magnitude in magnetic field strength, relationships between relevant physical parameters and magnetic field

strength can be obtained:

$$
\begin{aligned}
H &= 1.5\times10^{11}\left[\frac{B}{\text{Gauss}}\right]^{-0.27}\text{cm},\\
\Gamma_{\max} &= 190\left[\frac{B}{\text{Gauss}}\right]^{0.25}\\
, E_{\max} &= 1.6\left[\frac{B}{\text{Gauss}}\right]^{0.49}\text{V/m},\\
\int F_\nu d\nu &= 2.1\times10^{7}\left[\frac{B}{\text{Gauss}}\right]^{0.95}\text{MeV/cm}^2\text{/s}.
\end{aligned}
\tag{8.1}
$$

Figure 8.9 shows these parameters plotted with respect to magnetic field strength on a log-log scale after being normalized by their minimum value over the shown magnetic field strength range. These relationships allow one to estimate the energy output, energy available, cascade efficiency, etc. for any maximumly spinning black hole of mass $10^7 M_\odot$ with an available background photon energy density of 10^6 ergs/cm^3 (Ford et al., 2017).

Magnetic Field	Lorentz factor	Gap Half Width [cm]	Energy Flux [MeV/cm^2/s]
10^2 G	$2.0\times10^3 - 6.3e^{5.0\theta}$	$4.2\times10^7 e^{6.8\theta} + 4.1\times10^{10}$	$1.7\times10^9 - 3.3\times10^7 e^{4.1\theta}$
10^3 G	$1.0\times10^3 - 2.2e^{5.4\theta}$	$1.4\times10^7 e^{7.3\theta} + 2.2\times10^{10}$	$1.6\times10^{10} - 2.7\times10^8 e^{4.2\theta}$
10^4 G	$6.1\times10^2 - 1.4e^{5.3\theta}$	$7.1\times10^6 e^{7.2\theta} + 1.2\times10^{10}$	$1.4\times10^{11} - 2.8\times10^9 e^{4.0\theta}$
all	$1 - 2.3\times10^{-3} e^{6.8\theta}$	$1.0\times10^{-4} e^{5.3\theta} + 1$	$1 - 0.013e^{4.5\theta}$

Table 8.1: Angular fits for the peak Lorentz factor, gap half width, and outgoing photon energy flux. These fits are shown on Figures 8.1, 8.2, 8.3, 8.4, 8.6, and 8.7.

Chapter 9

Photon Background Energy Density

9.1 Varying the Strength of the available Photon Background Energy Density

Changing the background photon energy density around the black hole changes the energy available for $e^{\pm}$ to inverse Compton scatter with and for γ-rays to pair produce with in the one dimensional model. Changing U_b and observing how the structure of the gap changes gives one insight into the conditions needed to produce AGN. Figure 9.2 show how the size of the gap changes with the background photon energy density and angle. The energy stored in the kinetic energy of the charges can be seen in Figure 9.1. These figures detail how the kinetic energy of the charges and the size of the gap relate. Normalizing the gap width and Lorentz factor to one at the axis of rotation (Figures 9.4 & 9.3), one can see how, as a function of θ, they scale with U_b while the gap is thin. Overlaid on the results in Figures 9.1, 9.2, 9.3, 9.4, 9.6, & 9.7 are exponential fits as a function of θ. The fits are summarized in Table 9.1. These fits are useful in estimating the change in available energy as a function of inclination angle, estimating the outgoing γ-ray energy flux, etc. One can extrapolate these fits to any background energy density as long as the resulting gap width remains small. The gap width as a function of θ is $H \propto e^{6.8\theta}$. Figure 9.4

clearly illustrates how at large θ $\left(\text{again, large } \sim \cos^{-1}\left\{1/\sqrt{3}\right\}\right)$ the gap width increases up to ~ 1.55 times: its smallest width (at $\theta = 0$). The maximum Lorentz factor as a function of θ is $\Gamma_{\max} \propto -e^{5.2\theta}$ (Ford et al., 2017). As θ increases, the available kinetic energy in the gap drops by up to 45% at large θ. Similarly, the maximum electric field strength's angular dependence is $E_{\max} \propto e^{4.7\theta}$ (Ford et al., 2017).

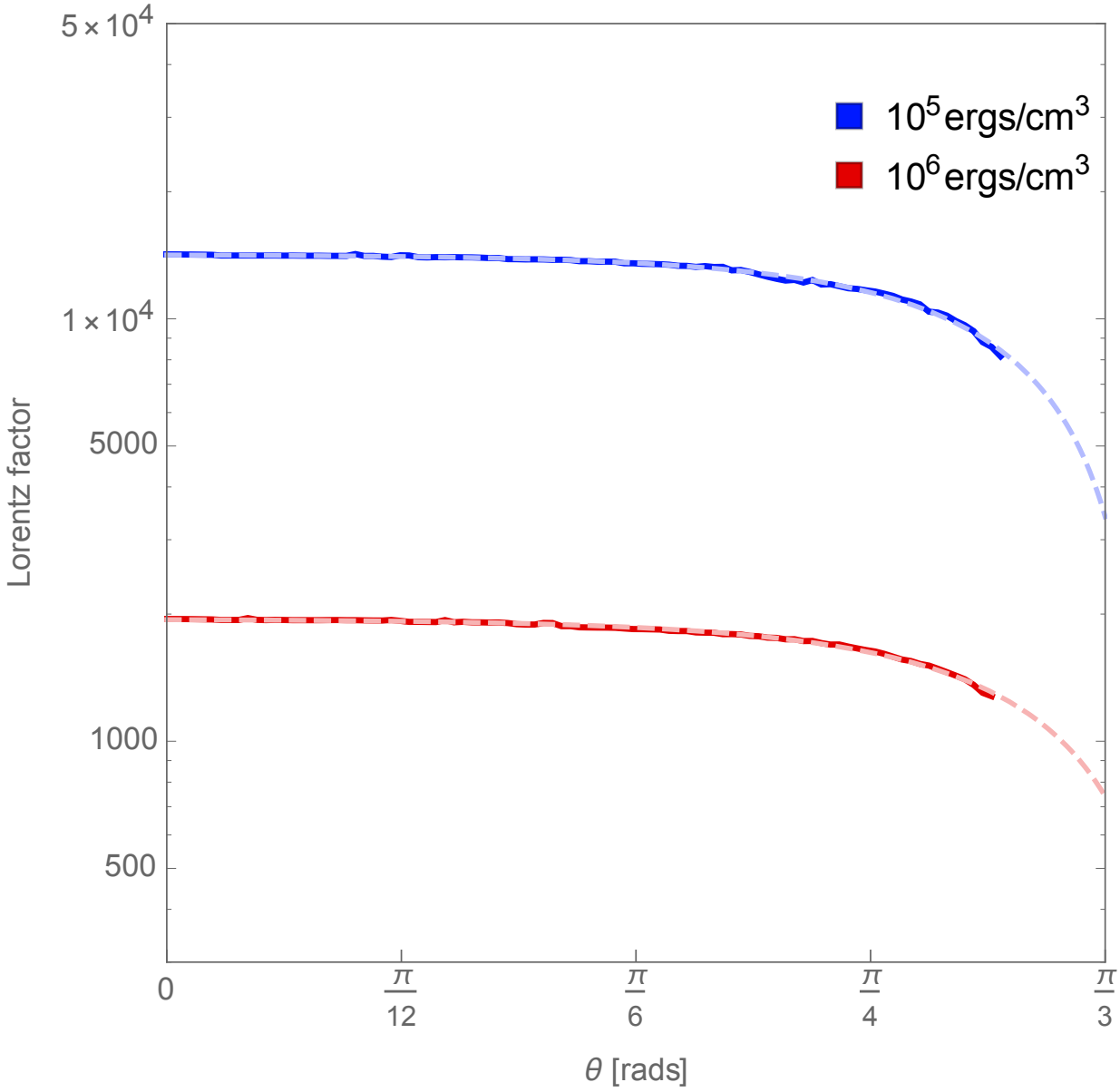

Figure 9.1: Lorentz factor versus polar angle. The three curves represent the change in Lorentz factor as polar angle increase going away from the axis of rotations for two different background energy densities. From the top down the U_b are 10^5ergs/cm^3 and 10^6ergs/cm^3. And similarly, the fits from the top down are $-40e^{5.4\theta}+1.4\times10^4$ and $-6.3e^{5.0\theta}+1.9\times10^3$.

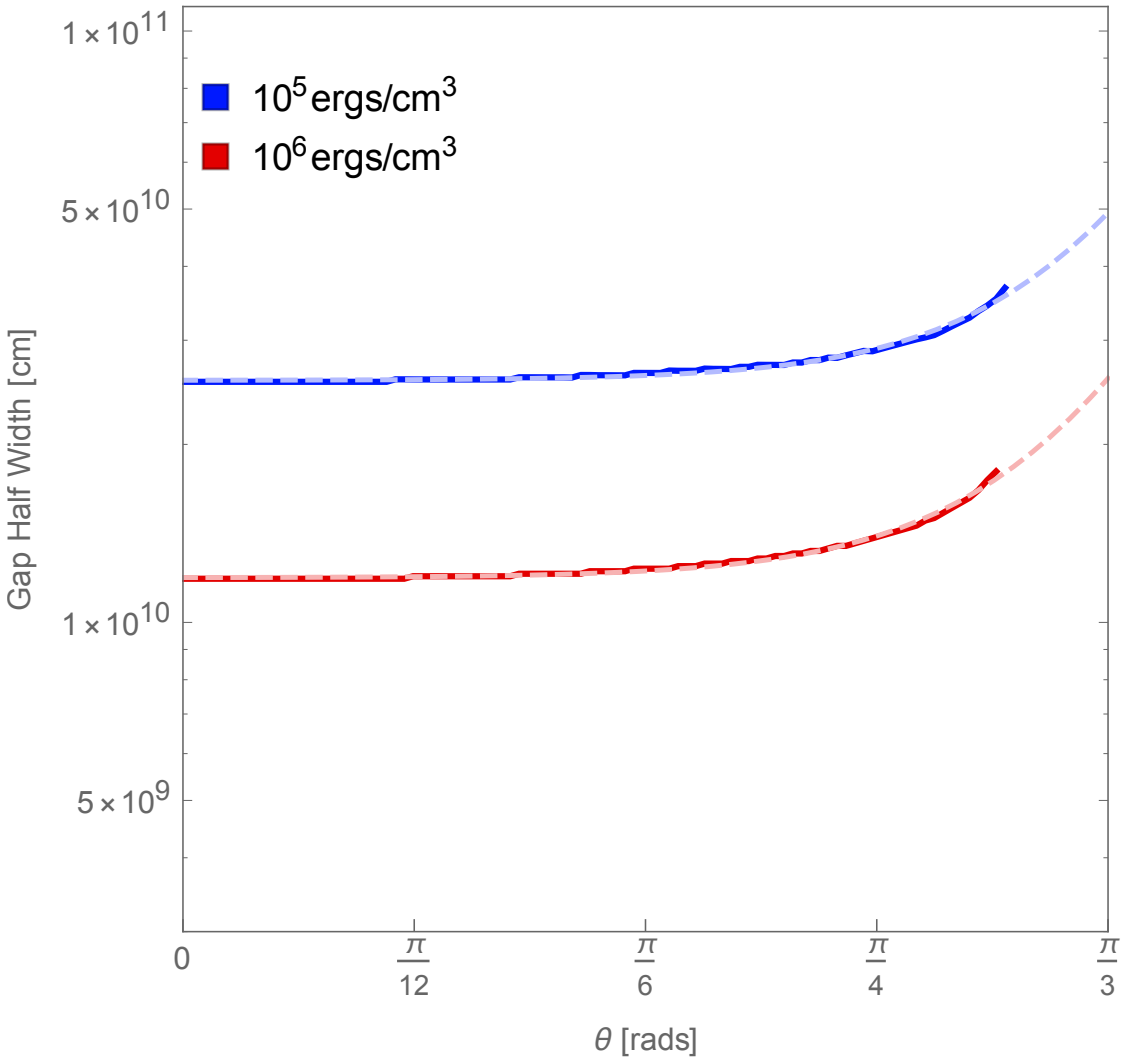

Figure 9.2: The width of half of the gap in centimeters versus polar angle. The three curves represent the change in the gap width as polar angle increases going away from the axis of rotations for two different ambient photon energy densities. From the top down the U_b are 10^5ergs/cm^3 and 10^6ergs/cm^3. And similarly, the fits from the top down are $1.2\times10^7 e^{7.4\theta}+2.6\times10^{10}$ and $7.1\times10^6 e^{7.2\theta}+1.2\times10^{10}$

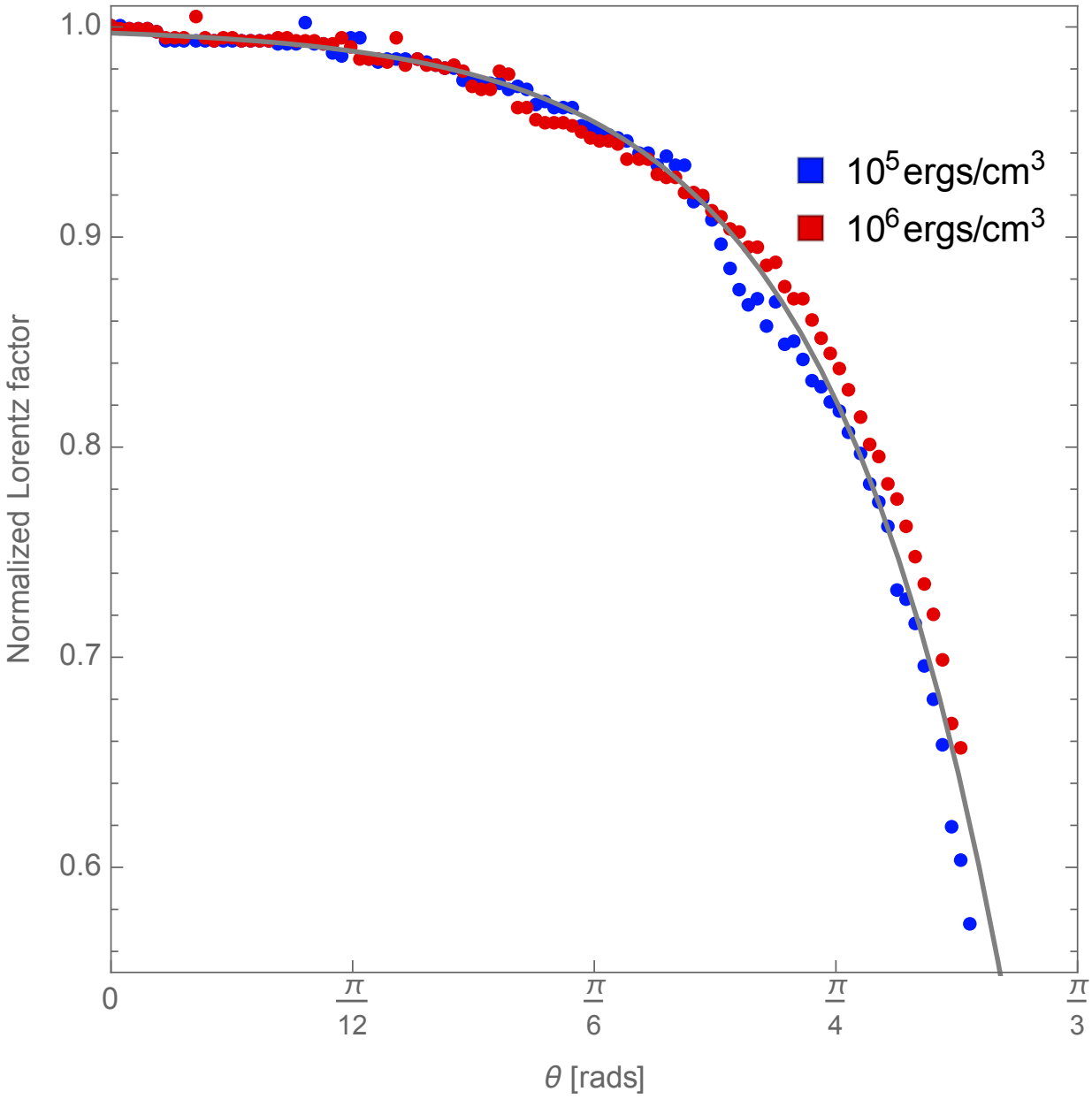

Figure 9.3: The width of half of the gap normalized at the axis of rotation versus the polar angle. An exponential fit of both background energy densities is $-2.9\times10^{-3}e^{5.2\theta}+1$. This demonstrates that for a thin gap the available kinetic energy in the gap as a function of θ is invariant relative to the background energy densities around the black hole.

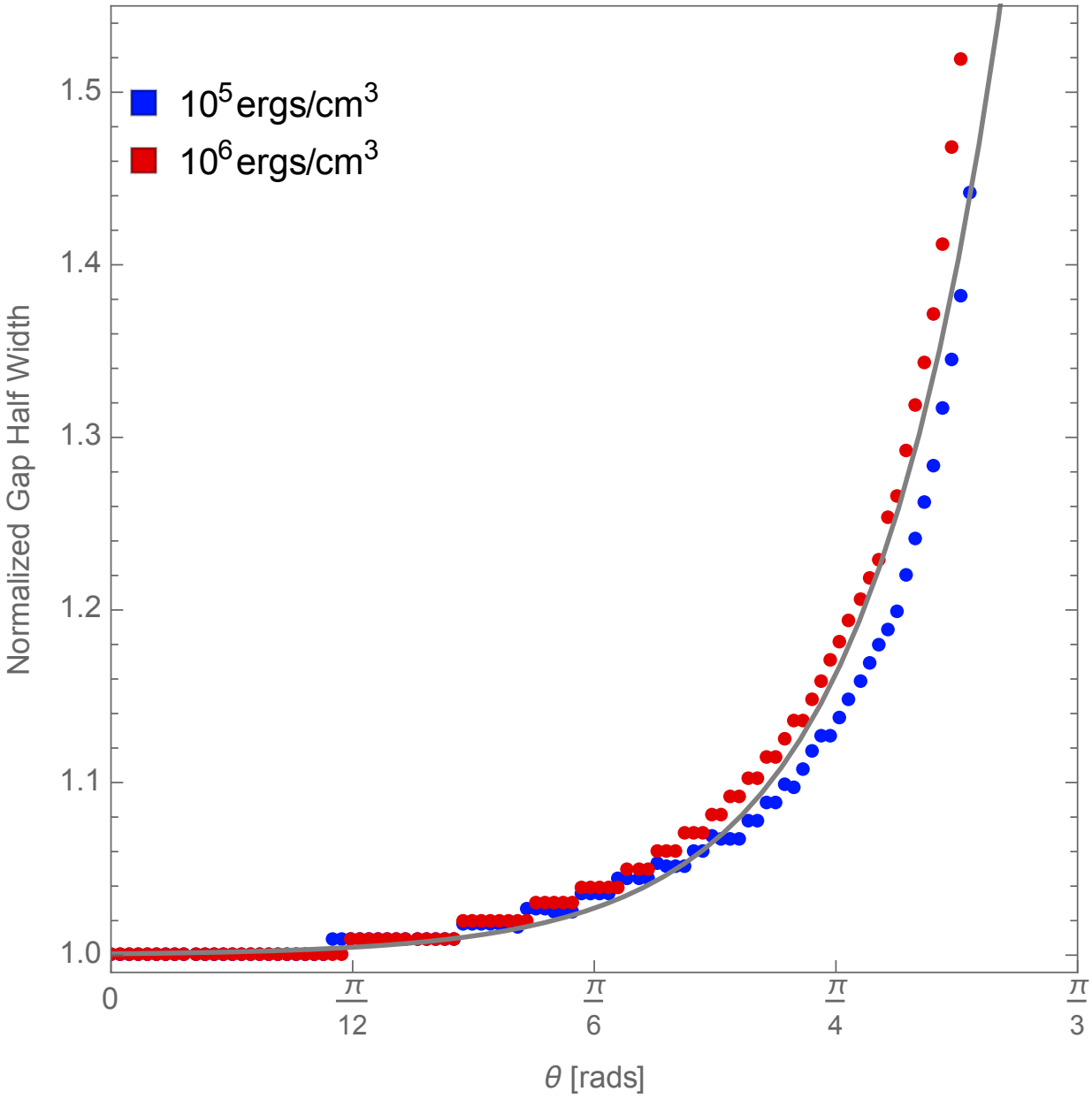

Figure 9.4: The width of half of the gap normalized at the axis of rotation versus the polar angle. An exponential fit of both background energy densities is $7.6\times10^{-4}e^{6.8\theta}+1$. This demonstrates how, while the gap is thin, the efficiency of the cascade process as a function of θ scales with the ambient photon energy density.

Figure 9.6 illustrates the drop-off in outgoing photon energy flux as a function of θ, $\int F_\nu d\nu \propto -e^{4.3\theta}$ (Ford et al., 2017). As θ increases, the outgoing energy flux drops by almost 90% at large θ. Figure 9.5 is a comparison of the spectral transition through the gap. Each line is a snapshot in space of the up-scattered spectrum in the gap. The top spectral transition plot is for $U_b = 10^5$ ergs/cm^3 and has a peak in its spectrum around 1000 MeV. The bottom spectral transition plot for $U_b = 10^6$ ergs/cm^3 is the same as Figure 6.4, and has a peak in its spectrum around 10 MeV.

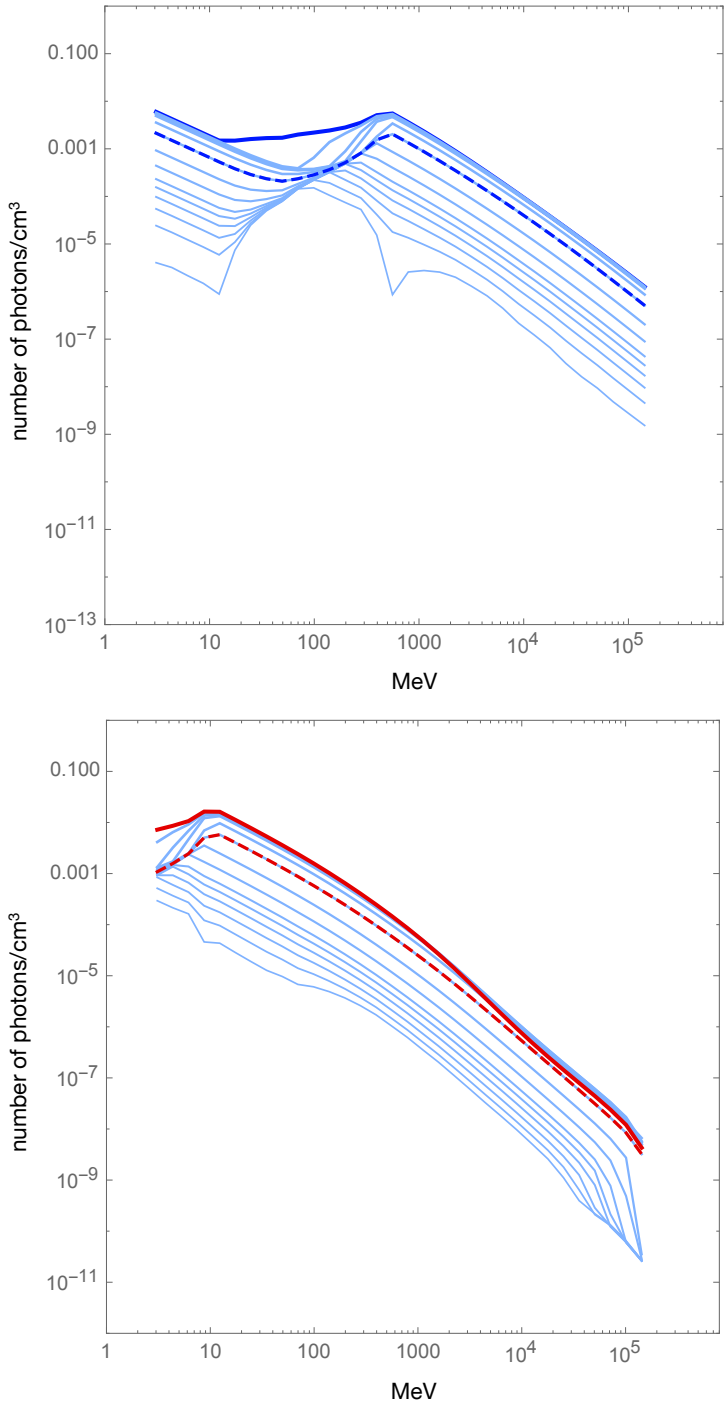

Figure 9.5: A comparison of the spectral transition from the inner boundary of the gap through the center of the gap (bold dashed line) and the outer boundary of the gap (bold solid line). Starting at 12% of the gap width after the inner (closest to the black hole) boundary, 14 spectral lines are shown. The 8 line under the dashed line are all equally spaced and from the inner side of the gap. The 4 lines between the dashed line and solid line are all from the outer part of the gap and equally spaced. The top spectral transition plot is for $U_b = 10^5$ ergs/cm^3. The bottom spectral transition plot is for $U_b = 10^6$ ergs/cm^3 and is the same as Figure 6.4.

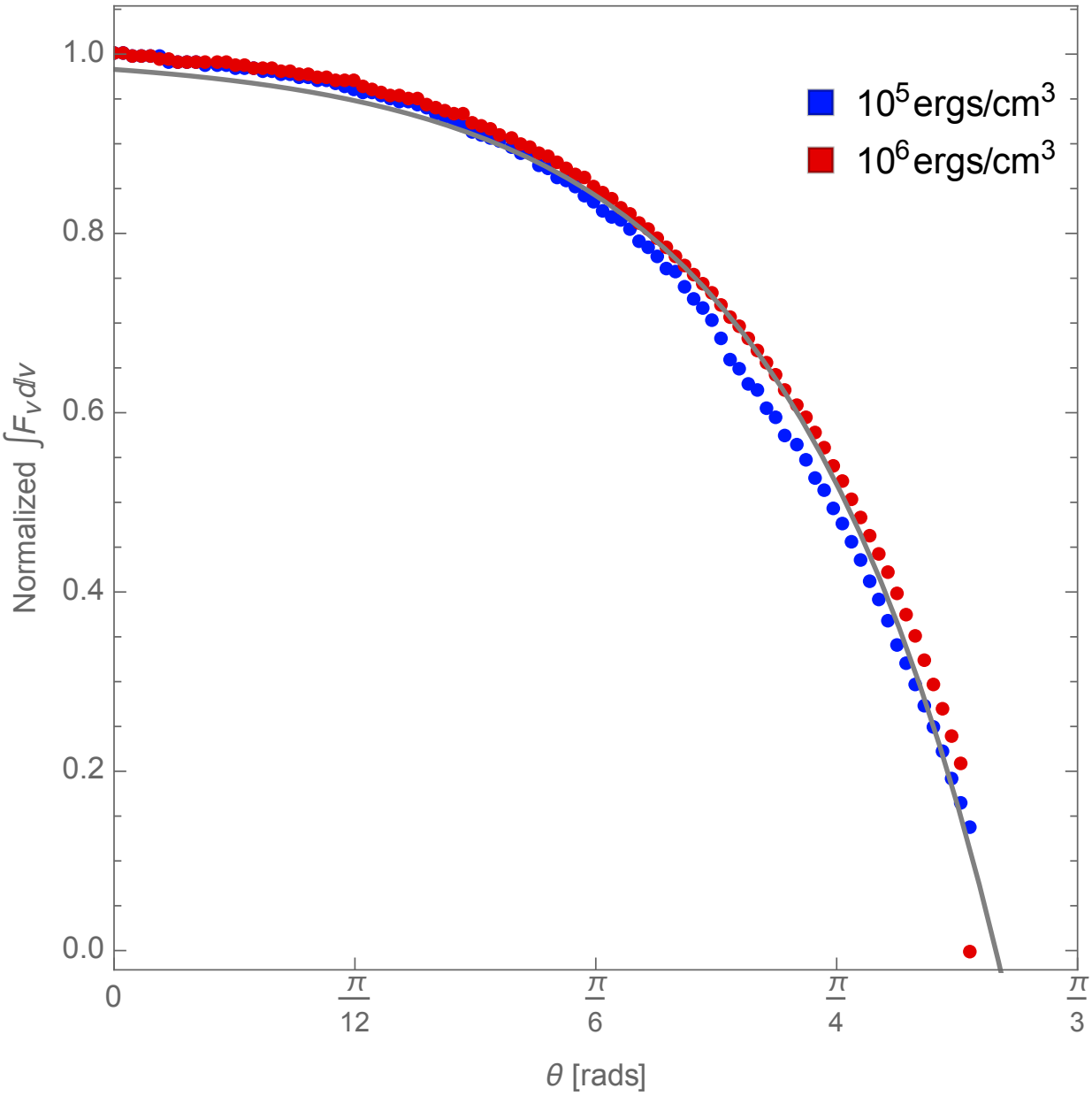

Figure 9.6: The outgoing photon energy density normalized at the axis of rotation versus the polar angle. An exponential fit of both background energy densities is $1 - 0.017e^{4.3\theta}$.

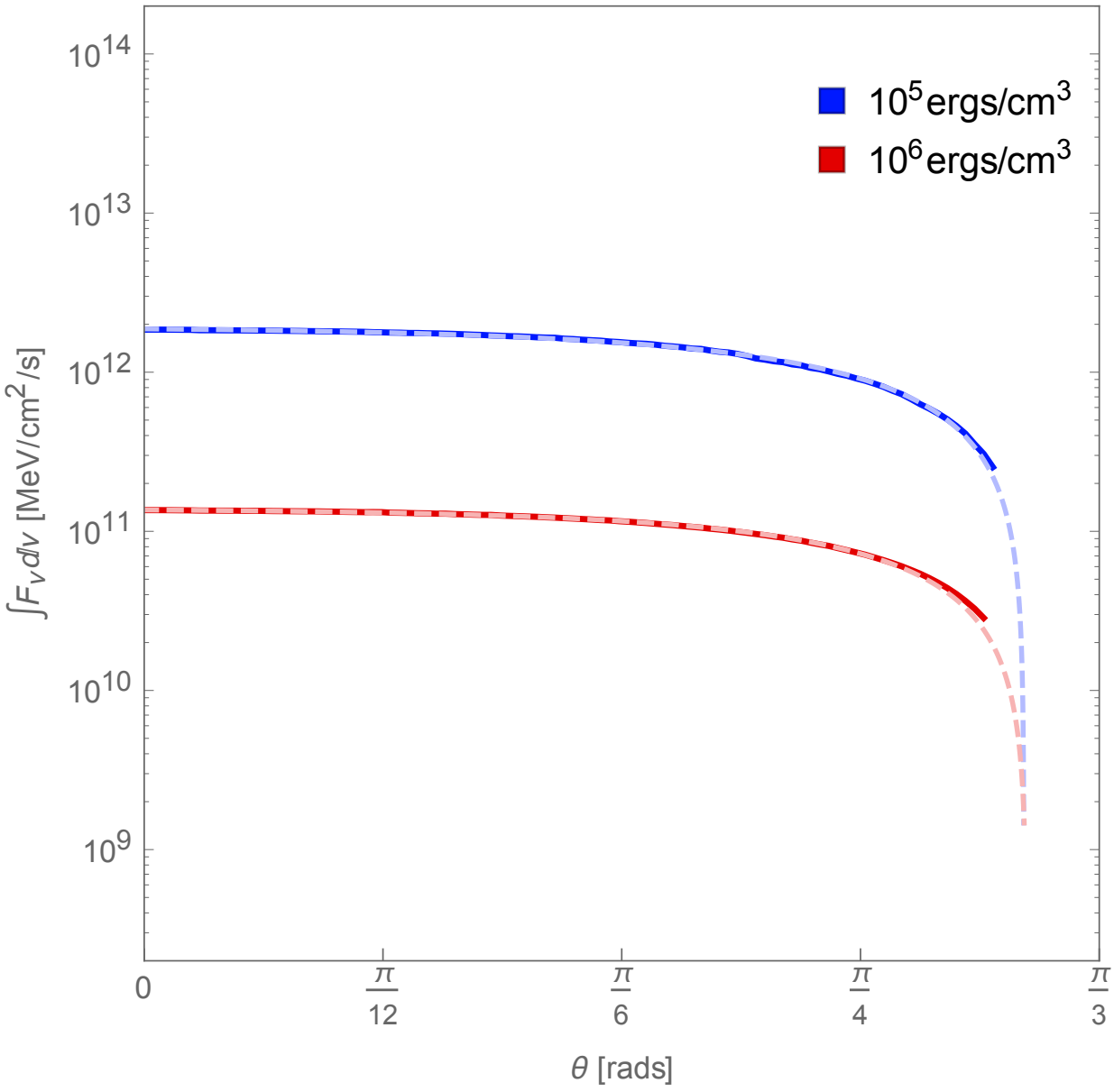

Figure 9.7: The total outgoing energy flux from the up-scattered photons versus polar angle. The curves represent the change in the gap width as polar angle increase going away from the axis of rotations for two different U_b and their corresponding fits, represented with dashed lines. From the top down the U_b are 10^5 ergs/cm^3 and 10^6 ergs/cm^3. And similarly, the fits from the top down are $1.9\times10^{12} - 6.3\times10^{10}e^{3.6\theta}$ and $1.4\times10^{11} - 2.8\times10^{9}e^{4.0\theta}$.

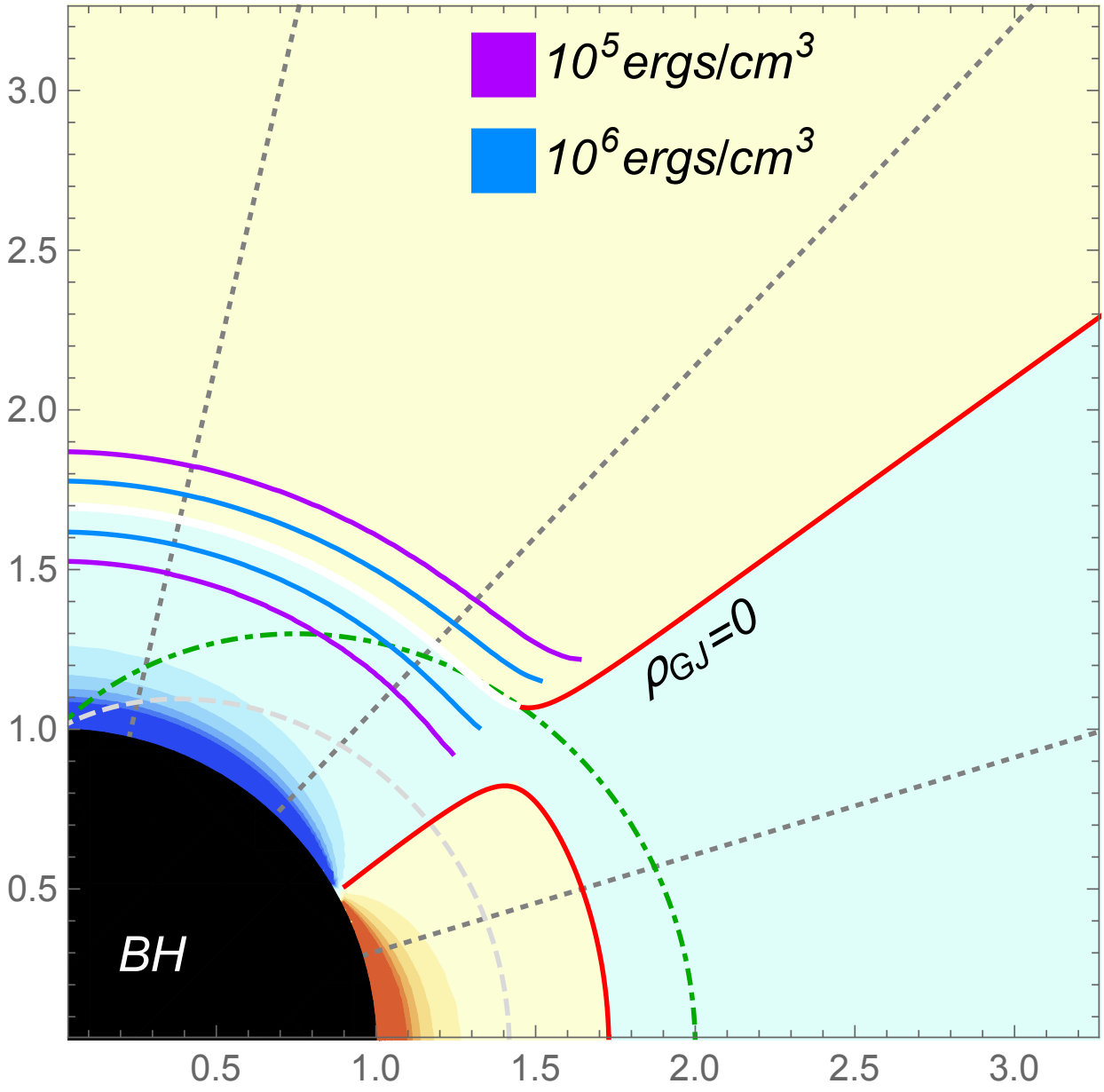

Figure 9.8: The black hole radius has been set to one, and the gap widths have be increase by an order of magnitude for illustration. One can see that as the magnetic field decreases the gap width with respect to the black hole radius increases. This is a sign that the plasma cascade is more efficient for stronger ambient photon energy densities.

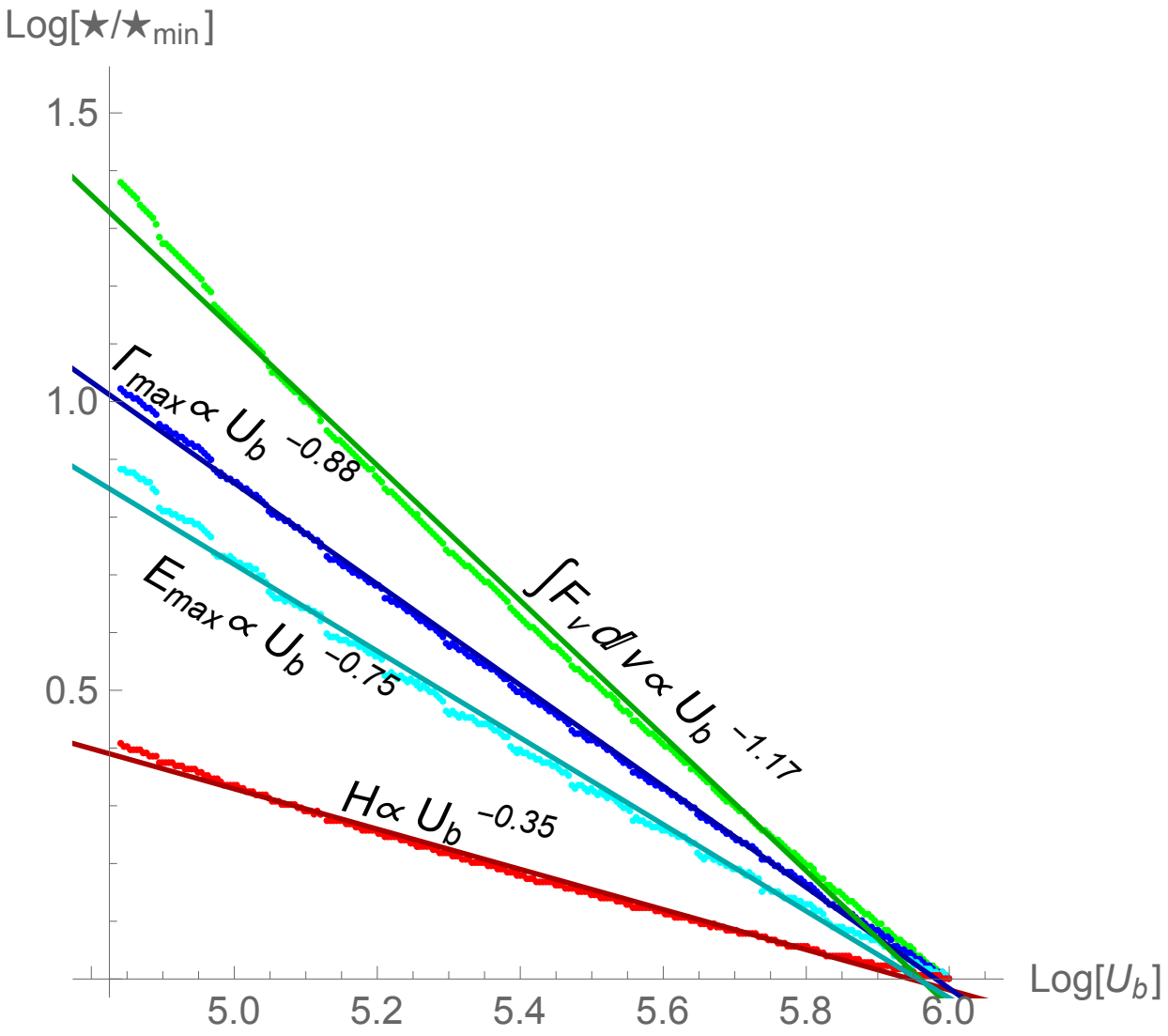

Figure 9.9: The ⋆ is a place holder that represents the maximum Lorentz factor, maximum electric field, gap width, and photon energy flux. Each physical quantity is normalized to its minimum value and then plotted with respect to the background energy density on a log-log scale.

After probing the structure of the gap over several orders of magnitude in background photon energy density, one can find relationships between relevant physical parameters and the ambient photon energy density:

$$
\begin{aligned}
H &= 1.4\times10^{12}\left[\frac{U_b}{\mathrm{ergs/cm^3}}\right]^{-0.35}\ \mathrm{cm},\\
\Gamma_{\max} &= 3.4\times10^{8}\left[\frac{U_b}{\mathrm{ergs/cm^3}}\right]^{-0.88},\\
E_{\max} &= 4.7\times10^{6}\left[\frac{U_b}{\mathrm{ergs/cm^3}}\right]^{-0.75}\ \mathrm{V/m},\\
\int F_\nu d\nu &= 1.8\times10^{29}\left[\frac{U_b}{\mathrm{ergs/cm^3}}\right]^{-1.2}\ \mathrm{MeV/cm^2/s}].
\end{aligned}
\tag{9.1}
$$

Figure 9.9 shows these parameters plotted with respect to the background energy density on a log-log scale after being normalized by their minimum value over the shown range of U_b. These relationships allow one to estimate, for example, the full gap width versus the black hole radius for any maximumly spinning black hole of mass $10^7 M_\odot$ embedded in a 10^4 Gauss magnetic field.

Energy Flux	Lorentz factor	Gap Half Width [cm]	Energy Flux [MeV/cm^2/s]
$10^5 \frac{\text{ergs}}{\text{cm}^3}$	$1.4\times10^4 - 40e^{5.4\theta}$	$1.2\times10^7 e^{7.4\theta} + 2.6\times10^{10}$	$1.9\times10^{12} - 6.3\times10^{10}e^{3.6\theta}$
$10^6 \frac{\text{ergs}}{\text{cm}^3}$	$1.9\times10^3 - 6.3e^{5.0\theta}$	$7.1\times10^6 e^{7.2\theta} + 1.2\times10^{10}$	$1.0\times10^{10} - 8.4\times10^8 e^{2.6\theta}$
all	$1 - 2.9\times10^{-3}e^{5.2\theta}$	$7.6\times10^{-4}e^{6.8\theta} + 1$	$1 - 0.017e^{4.3\theta}$

Table 9.1: Angular fits for the peak Lorentz factor, gap half width, and outgoing photon energy flux. These fits are shown on Figures 9.1, 9.2, 9.3, 9.4, 9.6, and 9.7.

Chapter 10

Spin

10.1 Probing Over All Spins

Varying the spin of the black hole from the maximum value, 1, to the minimum value, 0, changes the Goldreich-Julian charge density, and therefore, A_θ in the model. Furthermore, as the spin of the black hole decreases, the radius of the black hole increases and the inner edge of the gap gets closer to the horizon. Changing the spin and observing how the structure of the gap changes gives one insight into the conditions needed to produce AGN. Figure 10.1 show how the size of the gap changes with spin and angle. The energy stored in the kinetic energy of the charges can be seen in Figure 10.2. These figures detail how the kinetic energy of the charges and the size of the gap relate. Overlaid on the results in Figures 10.2, 10.1, 10.3, 10.4, 10.5, & 10.6 are exponential fits as a function of θ. The fits are summarized in Table 10.1. These fits are useful, for example, in estimating the change in available energy as a function of inclination angle. The gap width as a function of θ is $H \propto e^{7.4\theta}$ (Ford et al., 2017). Figure 10.3 illustrates how at large θ the gap width increases up to ~ 1.8 times: its smallest width (at $\theta = 0$). The maximum Lorentz factor as a function of θ is $\Gamma_{\max} \propto -e^{4.4\theta}$ (Ford et al., 2017). As θ increases, the available kinetic energy in the gap drops by up to 40% at large θ. Similarly, the maximum electric

field strength's angular dependence is $E_{\max} \propto -e^{1.7\theta}$ (Ford et al., 2017).

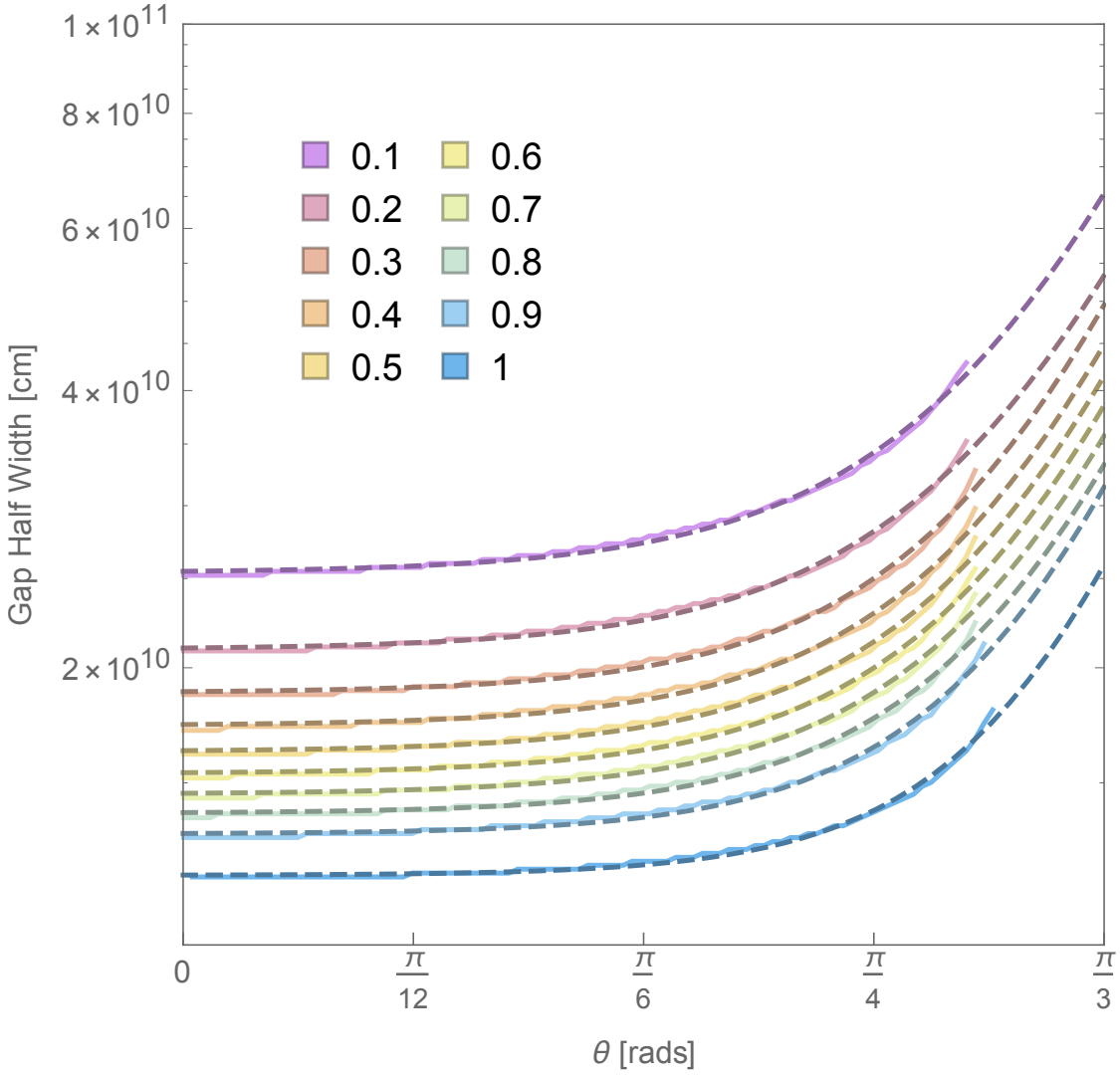

Figure 10.1: Half width of the gap versus polar angle. The 10 curves represent the change in width as polar angle increase going away from the axis of rotation for 10 different spins and their corresponding fits represented with dashed lines. From the top down the spins are 0.1, 0.2, 0.3, 0.4, 0.5, 0.6, 0.7, 0.8, 0.9, and 1. And similarly, the fits from the top down are $9.7\times10^7 e^{5.8\theta}+2.5\times10^{10}$, $7.9\times10^7 e^{5.8\theta}+2.1\times10^{10}$, $5.1\times10^7 e^{6.1\theta}+1.9\times10^{10}$, $4.7\times10^7 e^{6.1\theta}+1.7\times10^{10}$, $4.3\times10^7 e^{6.1\theta}+1.6\times10^{10}$, $3.7\times10^7 e^{6.1\theta}+1.5\times10^{10}$, $3.4\times10^7 e^{6.2\theta}+1.5\times10^{10}$, $2.7\times10^7 e^{6.3\theta}+1.4\times10^{10}$, $1.7\times10^7 e^{6.6\theta}+1.3\times10^{10}$, and $7.1\times10^6 e^{7.3\theta}+1.2\times10^{10}$.

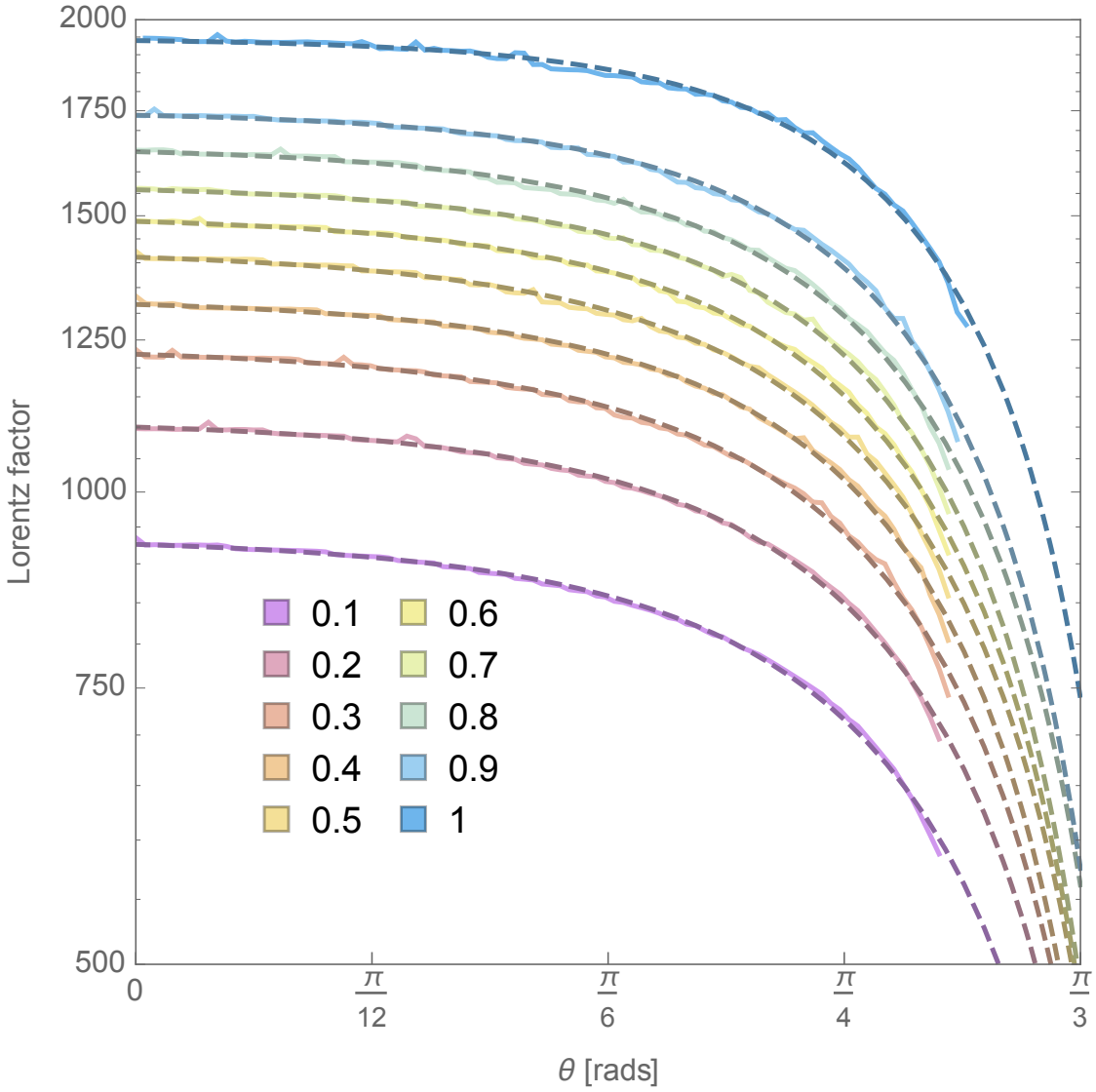

Figure 10.2: Lorentz factor of the gap versus polar angle. The 10 curves represent the change in width as polar angle increase going away from the axis of rotation for 10 different spin and their corresponding fits represented with dashed lines. From the top down the spins are 1, 0.9, 0.8, 0.7, 0.6, 0.5, 0.4, 0.3, 0.2, and 0.1. And similarly, the fits from the top down are $1900 - 6.3e^{5.0\theta}$, $940 - 9.5e^{4.0\theta}$, $1100 - 11e^{4.0\theta}$, $1200 - 13e^{4.0\theta}$, $1300 - 12e^{4.1\theta}$, $1400 - 15e^{4.0\theta}$, $1500 - 14e^{4.1\theta}$, $1600 - 11e^{4.4\theta}$, $1700 - 14e^{4.2\theta}$, and $1700 - 10e^{4.5\theta}$.

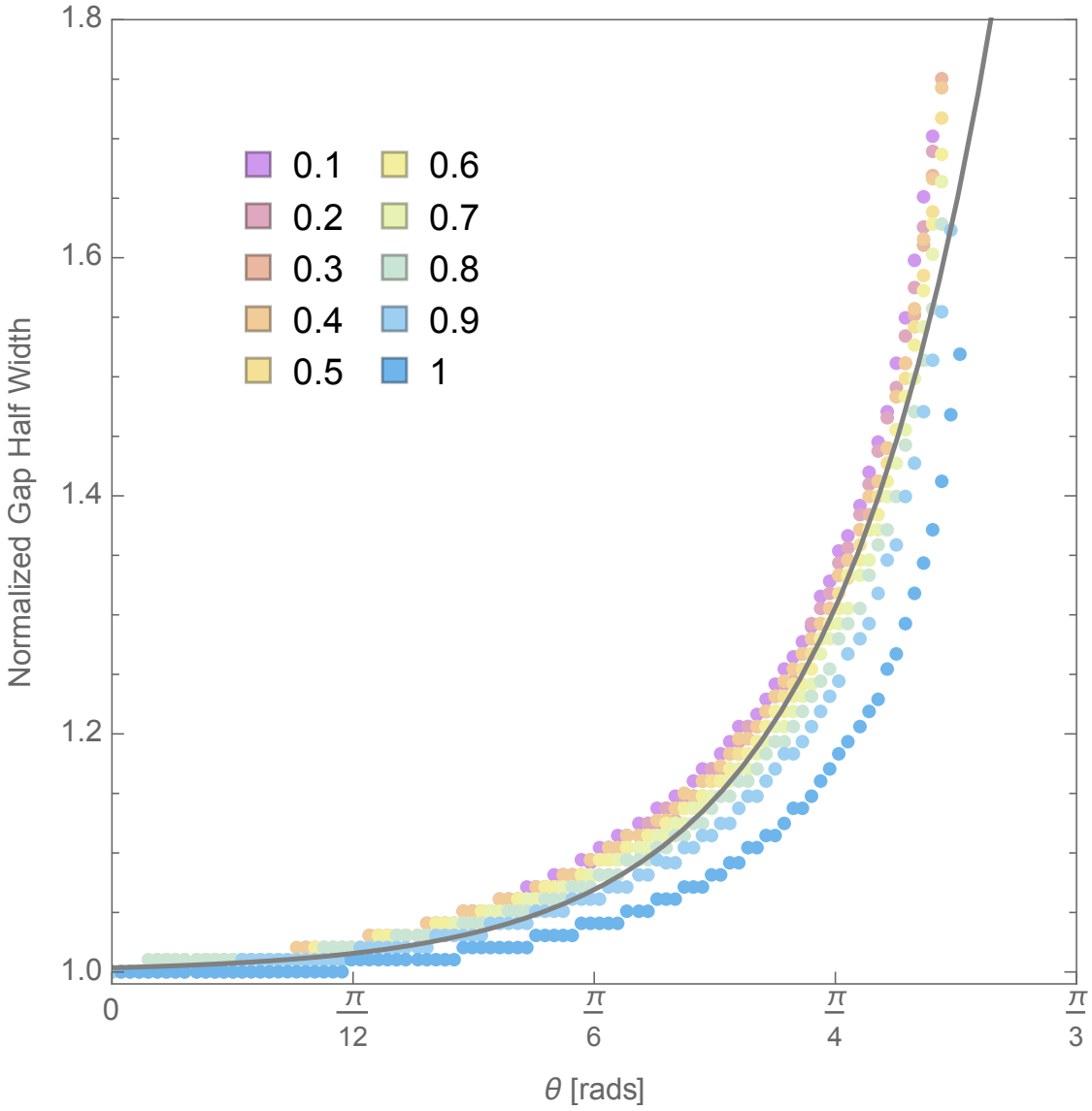

Figure 10.3: The width of half of the gap normalized at the axis of rotation versus the polar angle. An exponential fit of all ten spins is $5.2\times10^{-4}e^{7.4\theta}+1$.

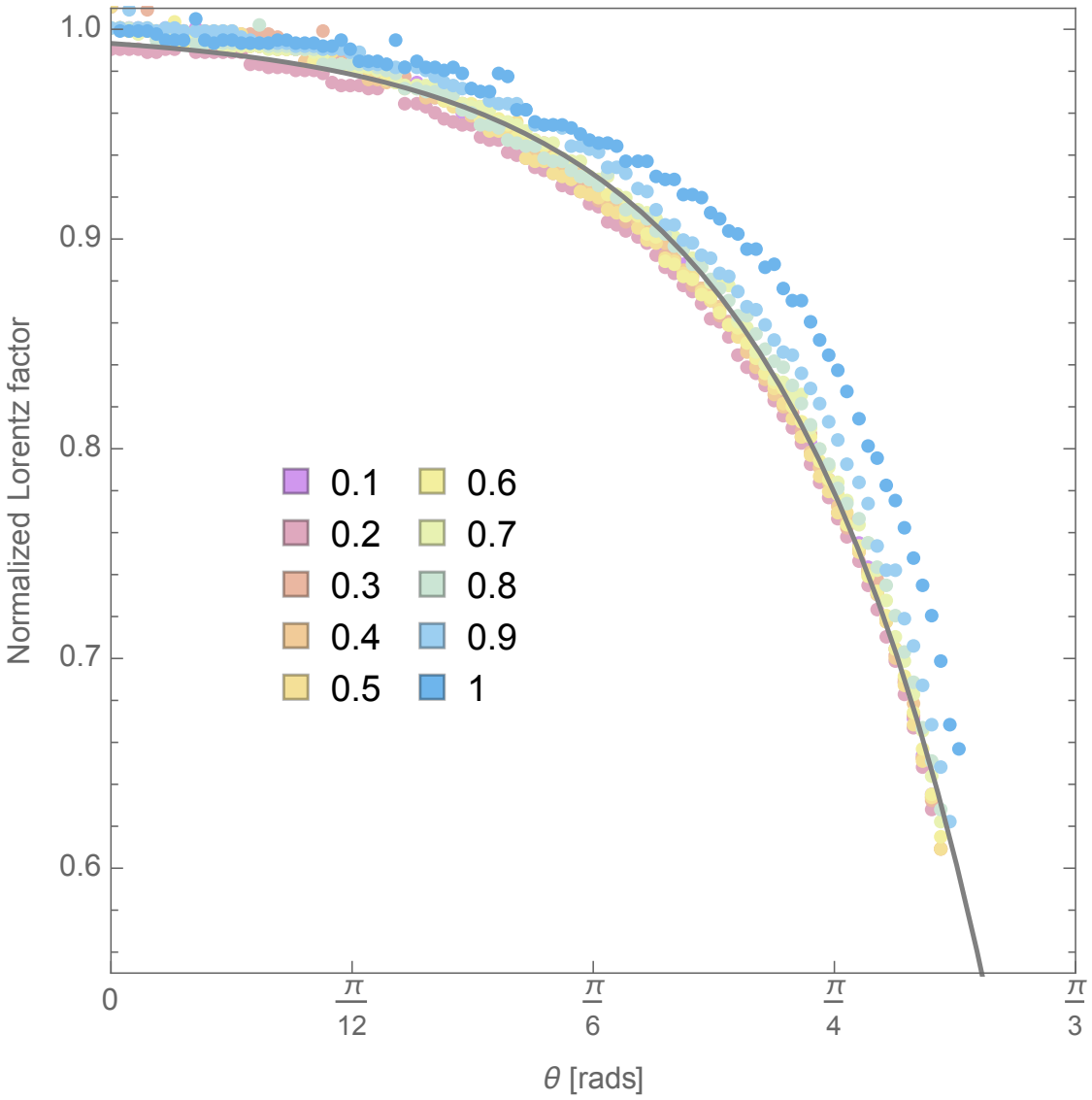

Figure 10.4: The width of half of the gap normalized at the axis of rotation versus the polar angle. An exponential fit of all ten spins is $1-6.8\times10^{-3}e^{4.4\theta}$.

Figure 10.5 illustrates the drop off in outgoing photon energy flux as a function of θ, $\int F_\nu d\nu \propto -e^{3.1\theta}$ (Ford et al., 2017). As θ increases, the outgoing energy flux drops by almost 90% at large θ. Figure 10.7 illustrates the varying gap size for different spins by overlaying the different gaps widths increased by an order of magnitude on Figure 4.1. The black hole radius for a maximumly spinning black hole is set to one. One can see that the black

hole radius increases substantially more than the gap width when the spin changes from 1 to 0.9. One can also see that the gap width increases more than the black hole radius when the spin changes from 0.3 to 0.1.

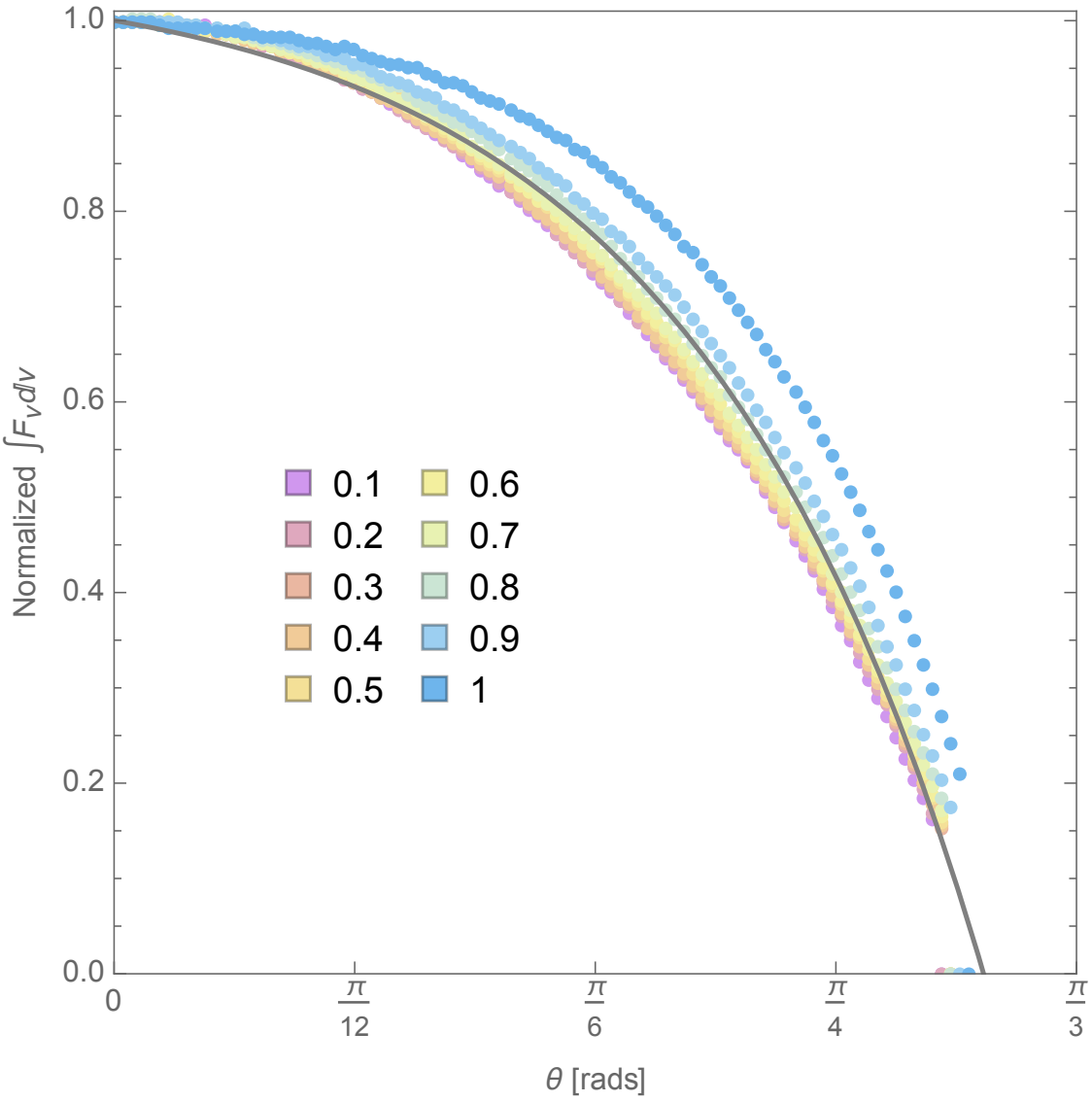

Figure 10.5: The outgoing photon energy density normalized at the axis of rotation versus the polar angle. An exponential fit of 10 different spins is $1.1 - 0.055e^{3.1\theta}$.

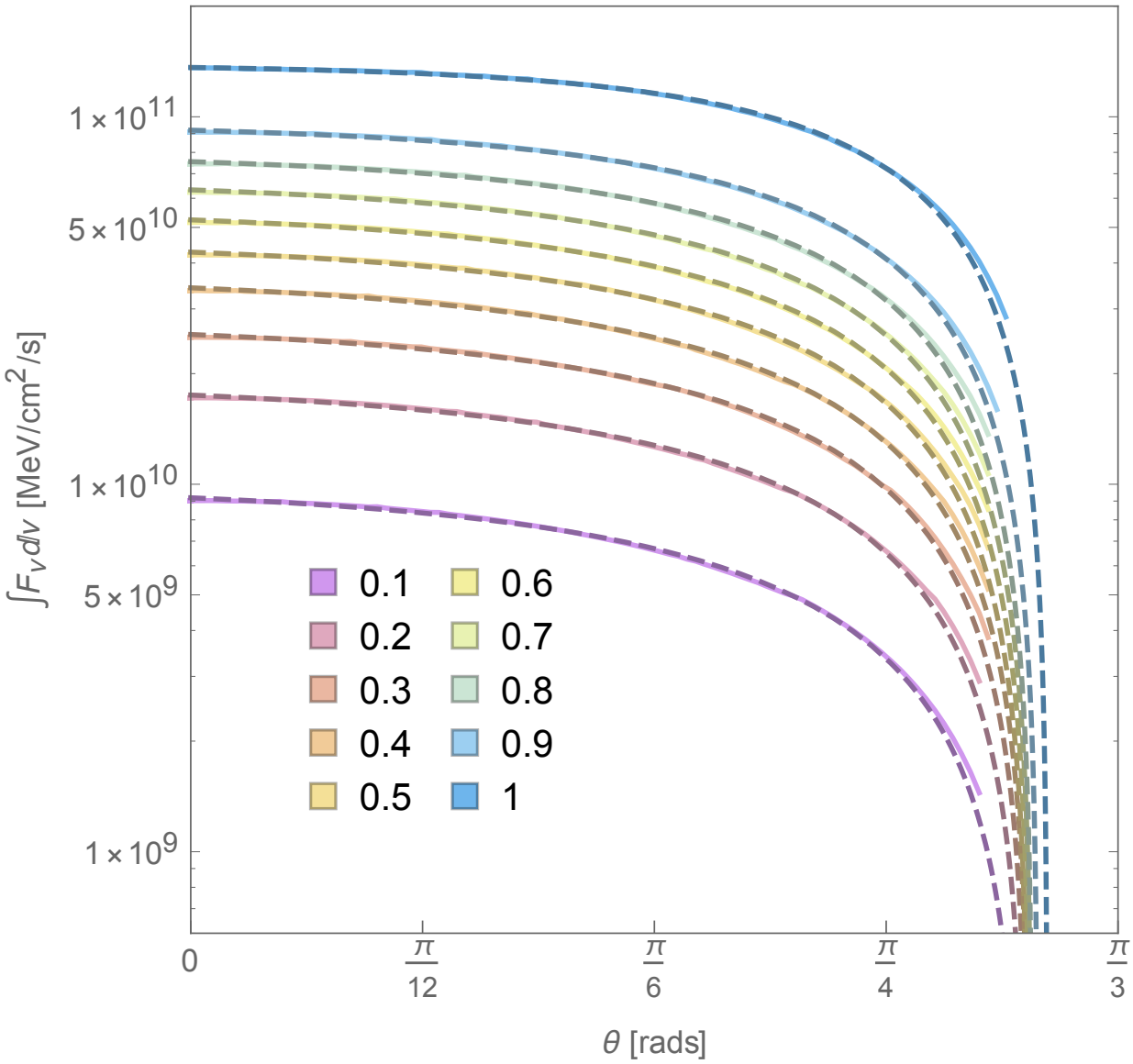

Figure 10.6: The total outgoing energy flux from the up-scattered photons versus polar angle. The three curves represent the change in the gap width as polar angle increase going away from the axis of rotations for 10 different spins and their corresponding fits, represented with dashed lines. From the top down the spins are 1, 0.9, 0.8, 0.7, 0.6, 0.5, 0.4, 0.3, 0.2, and 0.1. And similarly, the fits from the top down are $1.4\times10^{11}-2.8\times10^{9}e^{4.0\theta}$, $1.0\times10^{10}-8.4\times10^{8}e^{2.6\theta}$, $1.9\times10^{10}-1.6\times10^{9}e^{2.6\theta}$, $2.8\times10^{10}-2.2\times10^{9}e^{2.7\theta}$, $3.7\times10^{10}-3.1\times10^{9}e^{2.6\theta}$, $4.6\times10^{10}-3.4\times10^{9}e^{2.8\theta}$, $5.6\times10^{10}-4.0\times10^{9}e^{2.8\theta}$, $6.8\times10^{10}-4.5\times10^{9}e^{2.9\theta}$, $8.0\times10^{10}-4.4\times10^{9}e^{3.1\theta}$, and $9.6\times10^{10}-4.3\times10^{9}e^{3.3\theta}$.

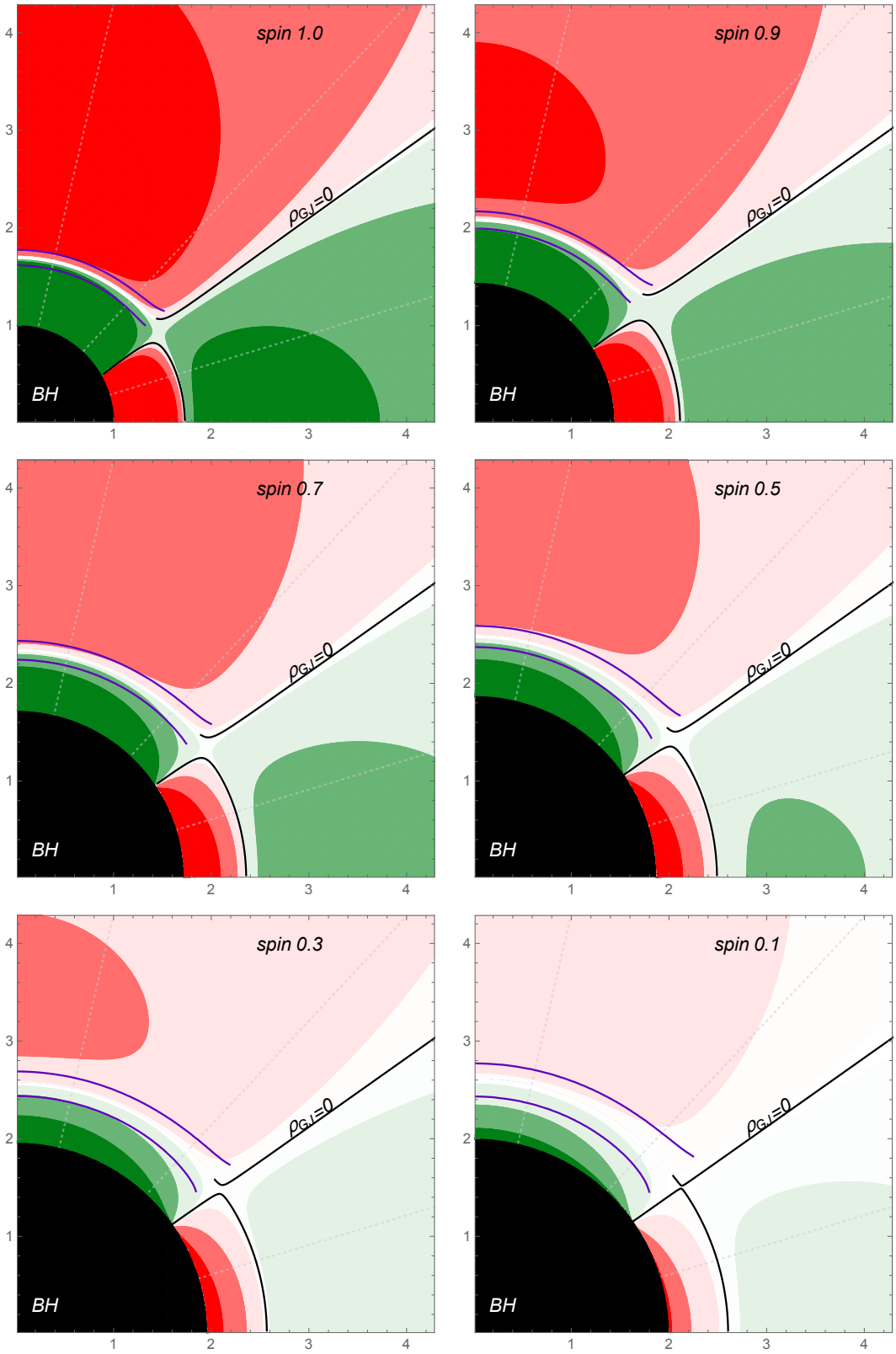

Figure 10.7: Gap width increased by an order of magnitude. For a maximally spinning black hole, the radius is set to one. The plasma density is displayed in red and green. It can be seen that, as the black hole's spin decreases, the gap width increase and the plasma density around the gap decreases.

After probing the structure of the gap over all spin, one can obtain relationships between physical parameters and a:

$$\begin{aligned} H &= 1.3\times10^{10}a^{-0.28}\text{cm}, \\ \Gamma_{\max} &= 1.6\times10^{3}a^{0.24}, \\ E_{\max} &= 110a^{0.49}\text{V/m}, \\ \int F_\nu d\nu &= 8.3\times10^{10}a^{0.96}\text{MeV/cm}^2\text{/s}. \end{aligned} \tag{10.1}$$

Figure 10.8 shows these parameters plotted with respect to a on a log-log scale after being normalized by their minimum value over the shown mass range. These relationships allow one to estimate the energy output, energy available, cascade efficiency, etc, for any black hole of mass 10^7 embedded in a 10^4 Gauss magnetic field with an available background photon energy density of 10^6 ergs/cm^3.

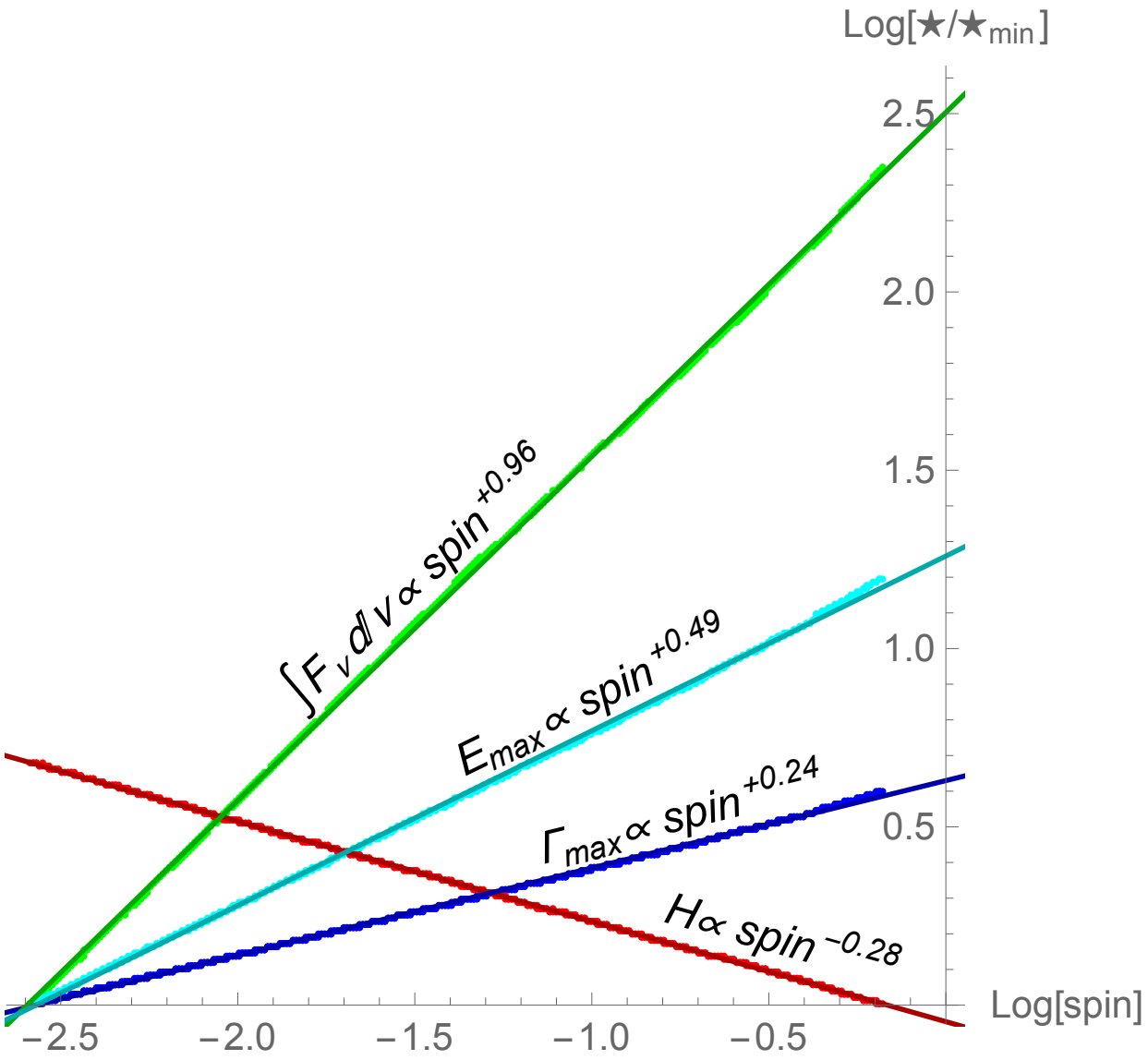

Figure 10.8: The ⋆ is a place holder that represents the maximum Lorentz factor, maximum electric field, gap width, and photon energy flux. Each physical quantity is normalized to its minimum value and then plotted with respect to the spin of the black hole on a log-log scale.

Spin	Lorentz factor	Gap Half Width [cm]	Energy Flux [MeV/cm^2/s]
1	$1900 - 6.3e^{5.0\theta}$	$7.1\times10^{6}e^{7.3\theta} + 1.2\times10^{10}$	$1.4\times10^{11} - 2.8\times10^{9}e^{4.0\theta}$
0.9	$940 - 9.5e^{4.0\theta}$	$1.7\times10^{7}e^{6.6\theta} + 1.3\times10^{10}$	$1.0\times10^{10} - 8.4\times10^{8}e^{2.6\theta}$
0.8	$1100 - 11e^{4.0\theta}$	$2.7\times10^{7}e^{6.3\theta} + 1.4\times10^{10}$	$1.9\times10^{10} - 1.6\times10^{9}e^{2.6\theta}$
0.7	$1200 - 13e^{4.0\theta}$	$3.4\times10^{7}e^{6.1\theta} + 1.5\times10^{10}$	$5.6\times10^{10} - 4.0\times10^{9}e^{2.8\theta}$
0.6	$1300 - 12e^{4.1\theta}$	$3.7\times10^{7}e^{6.1\theta} + 1.5\times10^{10}$	$4.6\times10^{10} - 3.4\times10^{9}e^{2.8\theta}$
0.5	$1400 - 15e^{4.0\theta}$	$4.3\times10^{7}e^{6.1\theta} + 1.6\times10^{10}$	$3.7\times10^{10} - 3.1\times10^{9}e^{2.6\theta}$
0.4	$1500 - 13e^{4.1\theta}$	$4.7\times10^{7}e^{6.1\theta} + 1.7\times10^{10}$	$2.8\times10^{10} - 2.2\times10^{9}e^{2.7\theta}$
0.3	$1600 - 11e^{4.4\theta}$	$5.1\times10^{7}e^{6.1\theta} + 1.9\times10^{10}$	$6.8\times10^{10} - 4.5\times10^{9}e^{2.9\theta}$
0.2	$1700 - 14e^{4.2\theta}$	$7.9\times10^{7}e^{5.8\theta} + 2.1\times10^{10}$	$8.0\times10^{10} - 4.4\times10^{9}e^{3.1\theta}$
0.1	$1700 - 10e^{4.5\theta}$	$9.7\times10^{7}e^{5.8\theta} + 2.5\times10^{10}$	$9.6\times10^{10} - 4.3\times10^{9}e^{3.3\theta}$
all	$1 - 6.8\times10^{-3}e^{4.4\theta}$	$5.2\times10^{-4}e^{7.4\theta} + 1$	$1.1 - 0.055e^{3.1\theta}$

Table 10.1: Angular fits for the peak Lorentz factor, gap half width, and outgoing photon energy flux. These fits are shown on Figures 10.1, 10.2, 10.3, 10.4, 10.5, and 10.6.

Chapter 11

Discussion

This chapter will use the scaling relations developed above to make physical estimates for observed galaxies.

11.1 Estimates of the Structure of the Gap

Combining the data shown in Figures 7.10, 8.9, 9.9, and 10.8 one can construct expressions to estimate the structure of the gap for any mass, spin, magnetic field, and background energy density:

$$H \simeq 4.7\times10^{8} a^{-0.31} \left[\frac{M}{M_{\odot}}\right]^{0.54} \left[\frac{B}{\text{Gauss}}\right]^{-0.27} \left[\frac{U_b}{\text{ergs/cm}^3}\right]^{-0.22} \text{cm}, \tag{11.1}$$

$$\Gamma_{\text{max}} \simeq 1.6\times10^{11} a^{0.24} \left[\frac{M}{M_{\odot}}\right]^{-0.52} \left[\frac{B}{\text{Gauss}}\right]^{0.25} \left[\frac{U_b}{\text{ergs/cm}^3}\right]^{-0.88}, \tag{11.2}$$

$$E_{\text{max}} \simeq 1.2\times10^{12} a^{0.49} \left[\frac{M}{M_{\odot}}\right]^{-1.1} \left[\frac{B}{\text{Gauss}}\right]^{0.49} \left[\frac{U_b}{\text{ergs/cm}^3}\right]^{-0.75} \text{V/m}, \tag{11.3}$$

$$\int F_\nu d\nu \simeq 3.2\times10^{49} a^{0.96} \left[\frac{M}{M_\odot}\right]^{-4.5} \left[\frac{B}{\text{Gauss}}\right]^{0.95} \left[\frac{U_b}{\text{ergs/cm}^3}\right]^{-1.2} \text{MeV/cm}^2\text{/s}. \tag{11.4}$$

By doubling Equation 11.1 and dividing by the radius of the black hole, one can relate the efficiency of the plasma cascade process over a wide range of parameters (Figure 11.2) or for a particular object. As a reminder, the black hole radius is $r_H = GM\left(1+\sqrt{1-a^2}\right)/c^2$. Comparing an active galaxy, e.g., M87, to an inactive galaxy, e.g., Sagittarius A, is illustrative. First one must estimate the background energy density from the luminosity, $U_b \simeq L/(4\pi c r^2)$. One can estimate r using the innermost stable circular orbit (Bardeen et al., 1972),

$$r_{\text{isco}} = \frac{GM}{c^2}\left(3+Z_2-\sqrt{(3-Z_1)(Z_1+2Z_2+3)}\right), \tag{11.5}$$

where

$$Z_1 = 1+\left(\sqrt[3]{\frac{ac^2}{GM}+1}+\sqrt[3]{1-\frac{ac^2}{GM}}\right)\sqrt[3]{1-\frac{a^2c^4}{G^2M^2}}, \tag{11.6}$$

$$Z_2 = \sqrt{\frac{3a^2c^2}{GM}+Z_1}. \tag{11.7}$$

The luminosity of M87 is 2.7×10^{42} ergs/s (Prieto & Fernández-Ontiveros, 2016). Sgr A* has a luminosity of 10^{37} ergs/s (Genzel et al., 1994). Let the ratio of the full width of the gap to the black hole radius be

$$\mathscr{W} = 9.4\times10^{8} a^{-0.31} \left[\frac{M}{M_\odot}\right]^{0.54} \left[\frac{B}{\text{Gauss}}\right]^{-0.27} \left[\frac{L/(4\pi c r_{\text{isco}}^2)}{\text{ergs/cm}^3}\right]^{-0.22} r_H^{-1}. \tag{11.8}$$

Using a mass of $10^{9.5} M_\odot$, a spin of 0.65, and a magnetic field of 15 G for M87 yields $\mathscr{W}_{\text{M87}} = 0.11$ (Wang et al., 2008; Kino et al., 2014). Similarly, using a mass of $10^{6.6} M_\odot$, a spin of 0.65, and a magnetic field of 30 G for Sgr A* yields $\mathscr{W}_{\text{Sgr A}^*} = 1.3$ (Johnson et al., 2015; Dokuchaev, 2015). The order of magnitude difference between $\mathscr{W}$ is consistent with M87 being active and Sgr A* not being active (Ford et al., 2017).

Figure 11.1 displays the full gap width over black hole radius versus magnetic field strength for M87 and Sgr A* and eight additional AGN. Tabel 11.1 contains the physical quantities used. Figure 11.1 shows that the ratio of the full gap width to black hole radius for AGN is < 1 for reasonable values of the magnetic field.

Figure 11.2 shows the parameter space in spin, magnetic field, and background energy density needed for an efficient cascade process. The red shaded regions are where the ratio of the full gap width versus the black hole radius is ≥ 1. The surfaces displayed in Figure 11.2 are spin$= 1$, $U_b = 0.1$, $U_b = 10$, $U_b = 10^6$, $B = 1$, $B = 10$, and $B = 10^5$.

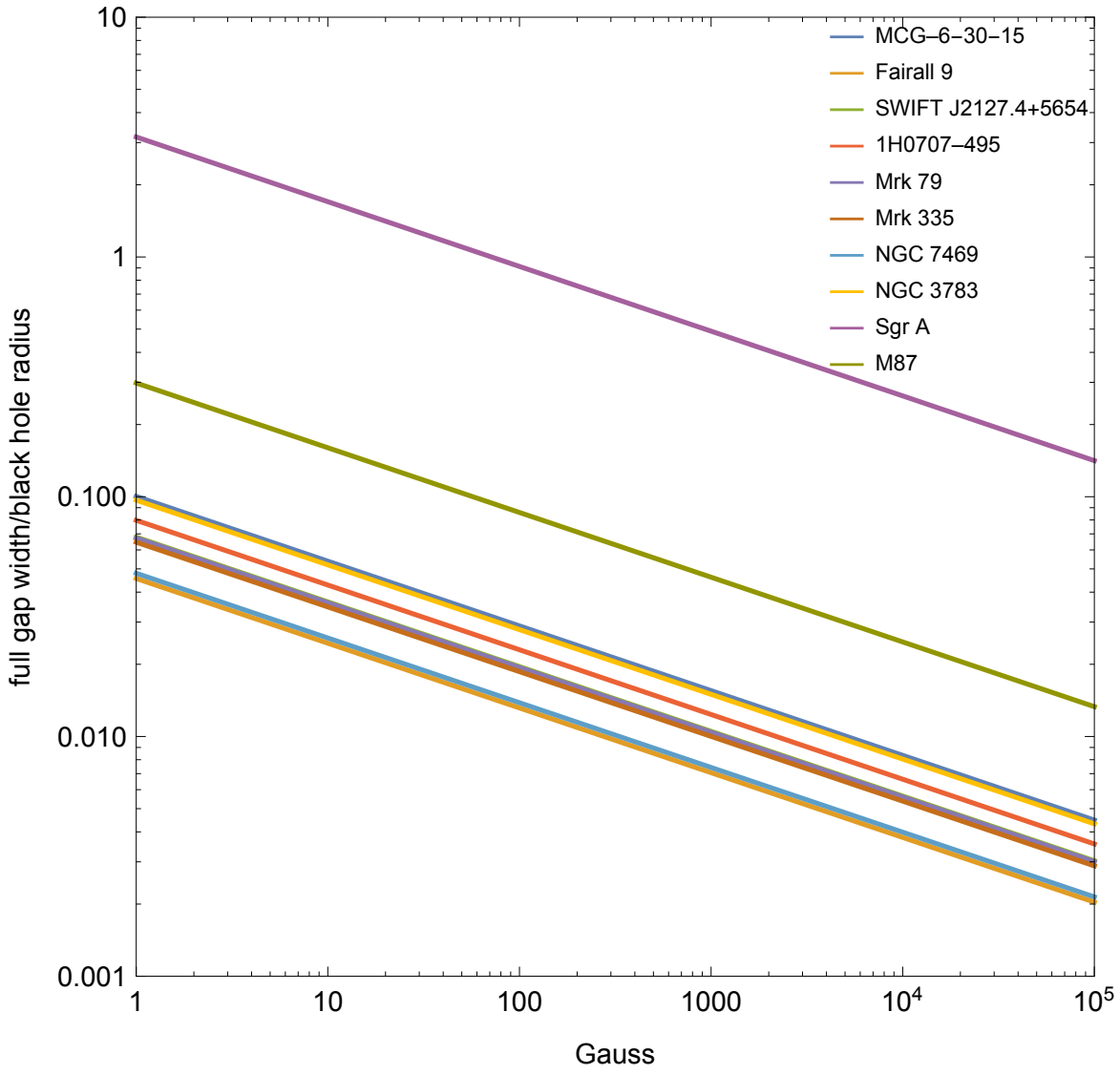

Figure 11.1: The curve for Sgr A* is at the top and followed by M87. Next is MCG–6-30-15 and NGC 3783. They are followed by 1H0707-495. Next Mrk 79, Mrk 335, and SWIFT J2127.4+5654 are clustered together. They are followed by NGC 7469 and Fairall 9. The values for mass, spin, and energy density in Equation 11.9 are listed in Table 11.1.

AGN	Spin	Mass	Energy Density
M87	0.65	$10^{9.5} M_{\odot}$	0.33 ergs/cm^3
Sgr A*	0.65	$10^{6.6} M_{\odot}$	2.1 ergs/cm^3
MCG–6-30-15	0.98	$10^{6.65} M_{\odot}$	3.8×10^7 ergs/cm^3
Fairall 9	0.65	$10^{8.41} M_{\odot}$	8.2×10^4 ergs/cm^3
SWIFT J2127.4+5654	0.65	$10^{7.18} M_{\odot}$	5.0×10^6 ergs/cm^3
1H0707–495	0.98	$10^{6.7} M_{\odot}$	8.4×10^7 ergs/cm^3
Mrk 79	0.7	$10^{7.72} M_{\odot}$	4.0×10^5 ergs/cm^3
Mrk 335	0.7	$10^{7.15} M_{\odot}$	7.5×10^6 ergs/cm^3
NGC 7469	0.69	$10^{7.09} M_{\odot}$	3.8×10^7 ergs/cm^3
NGC 3783	0.98	$10^{7.47} M_{\odot}$	8.5×10^4 ergs/cm^3

Table 11.1: The values used to in Equation 11.9 to make Figure 11.1 (Brenneman et al., 2011; Prieto & Fernández-Ontiveros, 2016; Genzel et al., 1994; Wang et al., 2008; Dokuchaev, 2015).

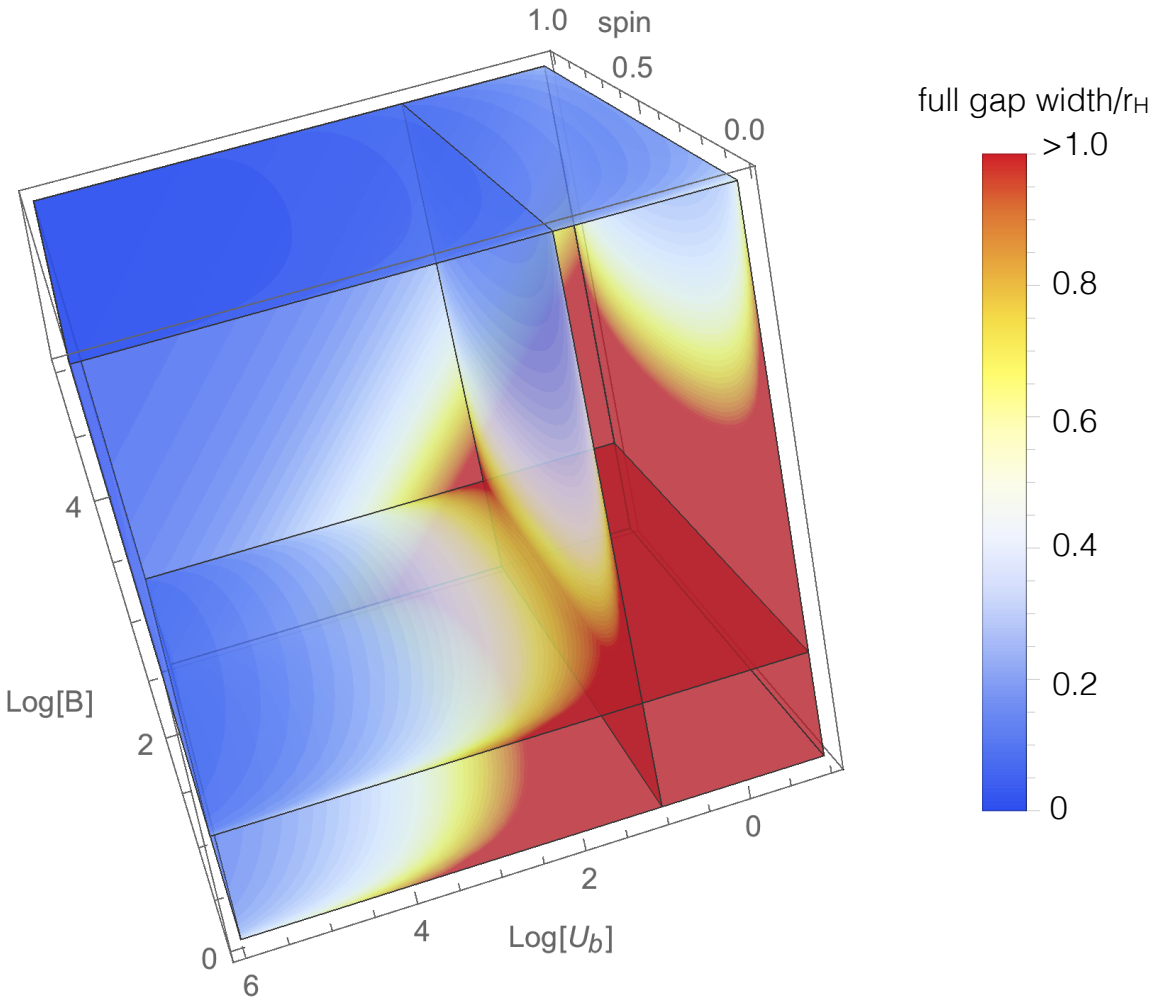

Figure 11.2: Contour plots of Equation 11.1 using a mass of $10^8 M_\odot$. The surfaces shown are spin= 1, $U_b = 0.1$, $U_b = 10$, $U_b = 10^6$, $B = 1$, $B = 10$, and $B = 10^5$. The red shading represents any value ≥ 1 for the ratio of the full gap width to the radius of the black hole.

11.2 Estimates of the Structure of the Gap with θ Dependence

One can also add an angular dependence to Equations 11.1, 11.2, 11.3, and 11.4. See Appendix A for the fits of the parameters verses their angular dependence.

$$H(\theta) \simeq \left\{1.3\times10^{6}e^{5.7\theta}+4.7\times10^{8}\right\} a^{-0.31}\left[\frac{M}{M_{\odot}}\right]^{0.54}\left[\frac{B}{\text{Gauss}}\right]^{-0.27}\left[\frac{U_b}{\text{ergs/cm}^3}\right]^{-0.22}\text{cm}. \quad (11.9)$$

$$\Gamma_{\max}(\theta) \simeq \left\{1.6\times10^{11}-8.2\times10^{8}e^{4.6\theta}\right\} a^{0.24}\left[\frac{M}{M_{\odot}}\right]^{-0.52}\left[\frac{B}{\text{Gauss}}\right]^{0.25}\left[\frac{U_b}{\text{ergs/cm}^3}\right]^{-0.88}. \quad (11.10)$$

$$E_{\max}(\theta) \simeq \left\{1.2\times10^{12}-1.7\times10^{10}e^{4.1\theta}\right\} a^{0.49}\left[\frac{M}{M_{\odot}}\right]^{-1.1}\left[\frac{B}{\text{Gauss}}\right]^{0.49}\left[\frac{U_b}{\text{ergs/cm}^3}\right]^{-0.75}\text{V/m}. \quad (11.11)$$

$$\int F_{\nu}d\nu(\theta) \simeq \left\{1.1-0.047e^{3.2\theta}\right\} 3.2\times10^{49}a^{0.96}\left[\frac{M}{M_{\odot}}\right]^{-4.5}\left[\frac{B}{\text{Gauss}}\right]^{0.95}\left[\frac{U_b}{\text{ergs/cm}^3}\right]^{-1.2}\text{MeV/cm}^2\text{/s}. \quad (11.12)$$

Using the same example as above, M87 and Sgr A*, one can use Equation 11.9 to make a plot similar to Figure 7.8. Figure 11.3 shows the gap widths of M87 and Sgr A* to scale with

the black hole radius. The inner boundary of the gap of Sgr A* goes into the black hole. Sgr A*'s gap is too close to the event horizon to maintain the assumptions of symmetry in Equation 4.31. Further study is needed to get a clear understanding of the structure of the gap around Sgr A*. However, a plausible interpretation of Figure 11.3 is that when the gap reaches the event horizon, the cascade process becomes too inefficient. Therefore the Blandford-Znajek process cannot power the jet.

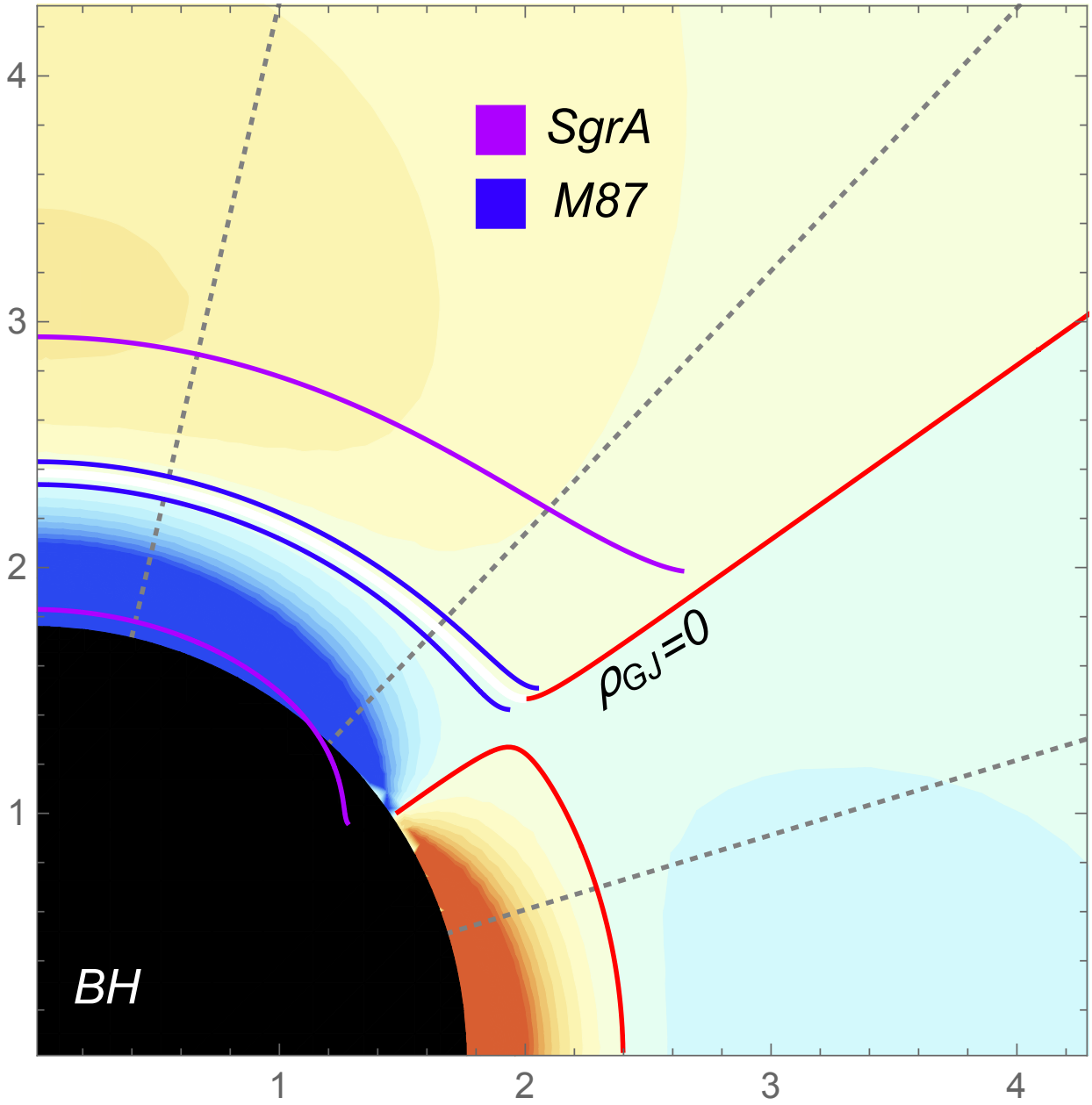

Figure 11.3: The black hole radius of a maximumly spinning black hole has been set to one, and the gap widths have been left to scale. M87 has a luminosity of 2.7×10^{42} ergs/s, mass of $10^{9.5}M_{\odot}$, a spin of 0.65, and a magnetic field of 15 G. Sgr A* has a luminosity of 10^{37} ergs/s, mass of $10^{6.6}M_{\odot}$, a spin of 0.65, and a magnetic field of 30 G.

Chapter 12

Summary

A brief summary of the novel science that has be presented is listed as a conclusion.

- The 2D structure of the gap (Chapter 6).

  This shows how efficient and energetic the cascade process is as it relates to the axis of rotation.

- Outgoing energy flux and spectrum (Chapter 6).

  These are both observables and the shape of the spectrum can give insight to the environment near the black hole.

- Varied physical parameters and probed the structure of the gap by:
  - Several orders of magnitude in black hole mass (Chapter 7).
  - Several orders of magnitude in magnetic field (Chapter 8).
  - Two orders of magnitude in photon background energy density (Chapter 9)
  - All spin (Chapter 10).

    This allows one to see how different physical parameters effect the structure and the efficiency of the gap.

- Characterize the relationship between relevant variables and obtained analytic expressions for estimating the structure of the gap (Chapter 11).

Future studies can expand upon this research by, i.e., implementing a realistic background spectrum (as apposed to the power law spectrum that has been assumed). The expressions (Equations 11.9, 11.10, 11.11, & 11.12) introduced in Chapter 11 should provided robust insight into the 2D structure of the gap for future investigations.

References

Aleksić, J., Alvarez, E. A., Antonelli, L. A., Antoranz, P., Asensio, M., Backes, M., Barrio, J. A., Bastieri, D., González, J. B., Bednarek, W., Berdyugin, A., Berger, K., Bernardini, E., Biland, A., Blanch, O., Bock, R. K., Boller, A., Bonnoli, G., Tridon, D. B., Braun, I., Bretz, T., Cañellas, A., Carmona, E., Carosi, A., Colin, P., Colombo, E., Contreras, J. L., Cortina, J., Cossio, L., Covino, S., Dazzi, F., Angelis, A. D., Caneva, G. D., del Pozo, E. D. C., Lotto, B. D., Mendez, C. D., Ortega, A. D., Doert, M., Domínguez, A., Prester, D. D., Dorner, D., Doro, M., Elsaesser, D., Ferenc, D., Fonseca, M. V., Font, L., Fruck, C., López, R. J. G., Garczarczyk, M., Garrido, D., Giavitto, G., Godinović, N., Hadasch, D., Häfner, D., Herrero, A., Hildebrand, D., Höhne-Mönch, D., Hose, J., Hrupec, D., Huber, B., Jogler, T., Kellermann, H., Klepser, S., Krähenbühl, T., Krause, J., Barbera, A. L., Lelas, D., Leonardo, E., Lindfors, E., Lombardi, S., López, M., López-Oramas, A., Lorenz, E., Makariev, M., Maneva, G., Mankuzhiyil, N., Mannheim, K., Maraschi, L., Mariotti, M., Martínez, M., Mazin, D., Meucci, M., Miranda, J. M., Mirzoyan, R., Miyamoto, H., Moldón, J., Moralejo, A., Munar-Adrover, P., Nieto, D., Nilsson, K., Orito, R., Oya, I., Paneque, D., Paoletti, R., Pardo, S., Paredes, J. M., Partini, S., Pasanen, M., Pauss, F., Perez-Torres, M. A., Persic, M., Peruzzo, L., Pilia, M., Pochon, J., Prada, F., Moroni, P. G. P., Prandini, E., Puljak, I., Reichardt, I., Reinthal, R., Rhode, W., Ribó, M., Rico, J., Rügamer, S., Saggion, A., Saito, K., Saito, T. Y., Salvati, M., Satalecka, K., Scalzotto, V., Scapin, V., Schultz, C., Schweizer, T., Shayduk, M., Shore, S. N., Sillanpää, A., Sitarek, J., Sobczynska, D., Spanier, F., Spiro, S., Stamatescu, V., Stamerra, A., Steinke, B., Storz, J.,

Strah, N., Surić, T., Takalo, L., Takami, H., Tavecchio, F., Temnikov, P., Terzić, T., Tescaro, D., Teshima, M., Tibolla, O., Torres, D. F., Treves, A., Uellenbeck, M., Vankov, H., Vogler, P., Wagner, R. M., Weitzel, Q., Zabalza, V., Zandanel, F., Zanin, R., Buson, S., Horan, D., Larsson, S., & D'Ammando, F. (2012). Pg 1553+113: Five years of observations with magic. *The Astrophysical Journal*, 748(1), 46.

Antonucci, R. (1993). Unified models for active galactic nuclei and quasars. *Annual Review of Astronomy and Astrophysics*, 31, 473–521.

Baade, W. & Minkowski, R. (1954). On the Identification of Radio Sources. *The Astrophysical Journal*.

Ball, G. H., Narayan, R., & Quataert, E. (2001). Spectral models of convection-dominated accretion flows. *The Astrophysical Journal*.

Bardeen, J. M., Press, W. H., & Teukolsky, S. A. (1972). Rotating black holes: Locally nonrotating frames, energy extraction, and scalar synchrotron radiation. *Astrophysical Journal*, 178, 347.

Barkov, M. V., Aharonian, F. A., & Bosch-Ramon, V. (2010). Gamma-ray flares from red giant/jet interactions in active galactic nuclei. *The Astrophysical Journal*, 724(2), 1517.

Beckmann, V. & Shrader, C. (2012). *Active Galactic Nuclei*. Wiley-VCH.

Begelman, M. C. & Meier, D. L. (1982). Thick accretion disks-Self-similar, supercritical models. *The Astrophysical Journal*.

Berestetskiĭ, V. B., Lifshitz, E. M., & Pitaevskiĭ, L. P. (1971). *Relativistic Quantum Theory*. Addison-Wesley Publishing Company, INC, 1 edition.

Beskin, V. S., Istomin, Y. N., & Parev, V. I. (1992). Filling the magnetosphere of a supermassive black-hole with plasma.

Blandford, R. D. & Payne, D. G. (1982). Hydromagnetic flows from accretion discs and the production of radio jets. *Monthly Notices of the Royal Astronomical Society*, 199, 883–903.

Blandford, R. D. & Znajek, R. L. (1977). Electromagnetic extraction of energy from kerr black holes. *Monthly Notices of the Royal Astronomical Society*, 179, 433–456.

Blażejowski, M., Blaylock, G., Bond, I. H., Bradbury, S. M., Buckley, J. H., Carter-Lewis, D. A., Celik, O., Cogan, P., Cui, W., Daniel, M., Duke, C., Falcone, A., Fegan, D. J., Fegan, S. J., Finley, J. P., Fortson, L., Gammell, S., Gibbs, K., Gillanders, G. G., Grube, J., Gutierrez, K., Hall, J., Hanna, D., Holder, J., Horan, D., Humensky, B., Kenny, G., Kertzman, M., Kieda, D., Kildea, J., Knapp, J., Kosack, K., Krawczynski, H., Krennrich, F., Lang, M., LeBohec, S., Linton, E., Lloyd-Evans, J., Maier, G., Mendoza, D., Milovanovic, A., Moriarty, P., Nagai, T. N., Ong, R. A., Power-Mooney, B., Quinn, J., Quinn, M., Ragan, K., Reynolds, P. T., Rebillot, P., Rose, H. J., Schroedter, M., Sembroski, G. H., Swordy, S. P., Syson, A., Valcarel, L., Vassiliev, V. V., Wakely, S. P., Walker, G., Weekes, T. C., White, R., Zweerink, J., Collaboration, T. V., Mochejska, B., Smith, B., Aller, M., Aller, H., Teräsranta, H., Boltwood, P., Sadun, A., Stanek, K., Adams, E., Foster, J., Hartman, J., Lai, K., Böttcher, M., Reimer, A., & Jung, I. (2005). A multiwavelength view of the tev blazar markarian 421: Correlated variability, flaring, and spectral evolution. *The Astrophysical Journal*, 630(1), 130.

Brenneman, L. W. & Reynolds, C. S. (2006). Constraining black hole spin via X-ray spectroscopy. *The Astrophysical Journal*.

Brenneman, L. W., Reynolds, C. S., Nowak, M. A., Reis, R. C., Trippe, M., Fabian, A. C., Iwasawa, K., Lee, J. C., Miller, J. M., Mushotzky, R. F., Nandra, K., & Volonteri, M. (2011). The spin of the supermassive black hole in ngc 3783. *The Astrophysical Journal*, 736(2), 103.

Chatterjee, R., Jorstad, S. G., Marscher, A. P., Oh, H., McHardy, I. M., Aller, M. F., Aller, H. D., Balonek, T. J., Miller, H. R., Ryle, W. T., Tosti, G., Kurtanidze, O., Nikolashvili, M., Larionov, V. M., & Hagen-Thorn, V. A. (2008). Correlated multi-wave band variability in the blazar 3c 279 from 1996 to 2007. *The Astrophysical Journal*, 689(1), 79.

Cravens, T. E. (1997). *Physics of Solar System Plasmas*. Cambridge University Press.

Curtis, H. D. (1920). Modern theories of the spiral nebulae. *Journal of the Royal Astronomical Society of Canada*.

Czerny, B. & Elvis, M. (1987). Constraints on quasar accretion disks from the optical/ultraviolet/soft X-ray big bump. *The Astrophysical Journal*.

Dermer, C. D. & Schlickeiser, R. (1994). On the location of the acceleration and emission sites in gamma-ray blazars. *The Astrophysical Journal, Supplement*, 90, 945–948.

Dokuchaev, V. I. (2015). Spin and mass of the supermassive black hole in the Galactic Center. *Physics of Atomic Nuclei*, 78(13), 1517–1519.

Fabian, A. C., Rees, M. J., Stella, L., & White, N. E. (1989). X-ray fluorescence from the inner disc in Cygnus X-1. *Monthly Notices of the Royal Astronomical Society*, 238, 729–736.

Fanaroff, B. L. & Riley, J. M. (1974). The morphology of extragalactic radio sources of high and low luminosity. *Monthly Notices of the Royal Astronomical Society*, 167(1), 31P.

Ford, A. L., Keenan, B. D., & Medvedev, M. V. (2017). Electron-positron cascade in magnetospheres of spinning black holes. *arXiv:1706.00542*.

Galeev, A. A., Rosner, R., & Vaiana, G. S. (1979). Structured coronae of accretion disks. *The Astrophysical Journal*, 229, 318–326.

Genzel, R., Hollenbach, D., & Townes, C. H. (1994). The nucleus of our Galaxy. *Reports on Progress in Physics*, 57(5), 417.

Georganopoulos, M. & Kazanas, D. (2003). Decelerating flows in TeV blazars: a resolution to the BL Lacertae-FR I unification problem. *The Astrophysical Journal*.

Giannios, D., Uzdensky, D. A., & Begelman, M. C. (2010). Fast tev variability from misaligned minijets in the jet of m87. *Monthly Notices of the Royal Astronomical Society*, 402(3), 1649.

Hayashida, M., Nalewajko, K., Madejski, G. M., Sikora, M., Itoh, R., Ajello, M., Blandford, R. D., Buson, S., Chiang, J., Fukazawa, Y., Furniss, A. K., Urry, C. M., Hasan, I., Harrison, F. A., Alexander, D. M., Baloković, M., Barret, D., Boggs, S. E., Christensen, F. E., Craig, W. W., Forster, K., Giommi, P., Grefenstette, B., Hailey, C., Hornstrup, A., Kitaguchi, T., Koglin, J. E., Madsen, K. K., Mao, P. H., Miyasaka, H., Mori, K., Perri, M., Pivovaroff, M. J., Puccetti, S., Rana, V., Stern, D., Tagliaferri, G., Westergaard, N. J., Zhang, W. W., Zoglauer, A., Gurwell, M. A., Uemura, M., Akitaya, H., Kawabata, K. S., Kawaguchi, K., Kanda, Y., Moritani, Y., Takaki, K., Ui, T., Yoshida, M., Agarwal, A., & Gupta, A. C. (2015). Rapid variability of blazar 3c 279 during flaring states in 20132014 with joint fermi-lat, nustar, swift, and ground-based multiwavelength observations. *The Astrophysical Journal*, 807(1), 79.

Henri, G. & Petrucci, P. O. (1997). Anisotropic illumination of AGN's accretion disk by a non thermal source. I. General theory and application to the Newtonian geometry. *Astronomy and Astrophysics*, 326, 87–98.

Hirotani, K. & Okamoto, I. (1998). Pair plasma production in a force-free magnetosphere around a supermassive black hole. *The Astrophysical Journal*, 497(2), 563–572.

Ho, L. C. (2002). On the relationship between radio emission and black hole mass in galactic nuclei. *The Astrophysical Journal*.

Hogan, B. S., Lister, M. L., Kharb, P., Marshall, H. L., & Cooper, N. J. (2011). Chandra dis-

covery of 10 new x-ray jets associated with fr ii radio core-selected agns in the mojave sample. *The Astrophysical Journal*, 730(2), 92.

Hoyle, F. & Fowler, W. A. (1963). Nature of Strong Radio Sources. *Nature*, 197(4867), 533–535.

Hubble, E. P. (1926). Extragalactic nebulae. *Astrophysical Journal*, 64, 321–369.

Hughes, S. A. & Blandford, R. D. (2003). Black Hole Mass and Spin Coevolution by Mergers. *The Astrophysical Journal Letters*, 585(2), L101.

Ichimaru, S. (1977). Bimodal behavior of accretion disks - Theory and application to Cygnus X-1 transitions. *The Astrophysical Journal*, 214, 840–855.

Igumenshchev, I. V., Abramowicz, M. A., & Narayan, R. (2000). Numerical Simulations of Convective Accretion Flows in Three Dimensions. *The Astrophysical Journal Letters*, 537, L27–L30.

Johnson, M. D., Fish, V. L., Doeleman, S. S., Marrone, D. P., Plambeck, R. L., Wardle, J. F. C., Akiyama, K., Asada, K., Beaudoin, C., Blackburn, L., Blundell, R., Bower, G. C., Brinkerink, C., Broderick, A. E., Cappallo, R., Chael, A. A., Crew, G. B., Dexter, J., Dexter, M., Freund, R., Friberg, P., Gold, R., Gurwell, M. A., Ho, P. T. P., Honma, M., Inoue, M., Kosowsky, M., Krichbaum, T. P., Lamb, J., Loeb, A., Lu, R.-S., MacMahon, D., McKinney, J. C., Moran, J. M., Narayan, R., Primiani, R. A., Psaltis, D., Rogers, A. E. E., Rosenfeld, K., SooHoo, J., Tilanus, R. P. J., Titus, M., Vertatschitsch, L., Weintroub, J., Wright, M., Young, K. H., Zensus, J. A., & Ziurys, L. M. (2015). Resolved magnetic-field structure and variability near the event horizon of sagittarius a*. *Science*, 350(6265), 1242–1245.

Kant, I. (1755). *Universal Natural History and Theory of the Heavens, ed. and trans.*

Kaspi, S., Brandt, W. N., Maoz, D., Netzer, H., Schneider, D. P., & Shemmer, O. (2007).

Reverberation Mapping of High-Luminosity Quasars: First Results. *The Astrophysical Journal*, 659, 997–1007.

Kino, M., Takahara, F., Hada, K., & Doi, A. (2014). Relativistic electrons and magnetic fields of the m87 jet on the 10 schwarzschild radii scale. *The Astrophysical Journal*, 786(1), 5.

Koratkar, A. & Blaes, O. (1999). The Ultraviolet and Optical Continuum Emission in Active Galactic Nuclei: The Status of Accretion Disks. *Publications of the Astronomical Society of the Pacific*, 111(755), 1.

Kovalev, Y. Y., Lister, M. L., & Homan, D. C. (2007). The inner jet of the radio galaxy M87. *The Astrophysical Journal*.

Krawczynski, H. & Treister, E. (2013). Active galactic nuclei—the physics of individual sources and the cosmic history of formation and evolution. *Frontiers of Physics*.

Krennrich, F., Bond, I. H., Bradbury, S. M., Buckley, J. H., Carter-Lewis, D. A., Cui, W., De la Calle-Perez, I., Fegan, D. J., Fegan, S. J., Finley, J. P., Gaidos, J. A., Gibbs, K., Gillanders, G. H., Hall, T. A., Hillas, A. M., Holder, J., Horan, D., Jordan, M., Kertzman, M. P., Kieda, D. B., Kildea, J., Knapp, J., Kosack, K., Lang, M. J., Le Bohec, S., Moriarty, P., Müller, D., Ong, R. A., Pallassini, R., Petry, D., Quinn, J., Reay, N. W., Reynolds, P. T., Rose, H. J., Sembroski, G. H., Sidwell, R., Stanton, N., Swordy, S. P., Vasilev, V., Wakely, S. P., & Weekes, T. C. (2002). Discovery of Spectral Variability of Markarian 421 at TeV Energies. *Astrophysical Journal*, 575, L9–L14. 24 p.

Landau, L. D. & Lifshitz, E. M. (1960). *Electrodynamics of Continuous Media*. Pergamon Press.

Levinson, A. (2007). On the Origin of Rapid Flares in TeV Blazars. *The Astrophysical Journal Letters*.

Macdonald, D. A. (1984). Numerical models of force-free black-hole magnetospheres. *Monthly Notices of the Royal Astronomical Society*, 211(2), 313.

Malzac, J., Jourdain, E., Petrucci, P. O., & Henri, G. (1998). Anisotropic illumination in AGNs. The reflected component. Comparison to hard X-ray spectra from Seyfert Galaxies. *Astronomy and Astrophysics*, 336, 807–814.

Matsuda, Y., Smail, I., Geach, J. E., Best, P. N., Sobral, D., Tanaka, I., Nakata, F., Ohta, K., Kurk, J., Iwata, I., Bielby, R., Wardlow, J. L., Bower, R. G., Ivison, R. J., Kodama, T., Yamada, T., Mawatari, K., & Casali, M. (2011). An Hα search for overdense regions at z = 2.23*. *Monthly Notices of the Royal Astronomical Society*, 416(3), 2041.

McLure, R. J. & Jarvis, M. J. (2004). The relationship between radio luminosity and black hole mass in optically selected quasars. *Monthly Notices of the Royal ....*

Mucke, A. & Protheroe, R. J. (2001). A Proton synchrotron blazar model for flaring in Markarian 501. *Astropartical Physics*, 15, 121–136.

Narayan, R., Igumenshchev, I. V., & Abramowicz, M. A. (2000). Self-similar Accretion Flows with Convection. *The Astrophysical Journal*, 539, 798–808.

Narayan, R., Quataert, E., Igumenshchev, I. V., & Abramowicz, M. A. (2002). The Magneto-hydrodynamics of Convection-dominated Accretion Flows. *The Astrophysical Journal*, 577, 295–301.

Narayan, R. & Yi, I. (1994). Advection-dominated accretion: A self-similar solution. *The Astrophysical Journal Letters*, 428, L13–L16.

Netzer, H. (2006). Active galactic nuclei: basic physics and main components. *Physics of Active Galactic Nuclei at All Scales*.

Perlman, E. S. & Kazanas, D. (2005). Is the core of M87 the source of its TeV emission? implications for unified schemes. *The Astrophysical Journal*.

Peterson, B. M. (1997). *An Introduction to Active Galactic Nuclei.* Cambridge University Press.

Peterson, B. M. (2007). The Masses of Black Holes in Active Galactic Nuclei. *The Central Engine of Active Galactic Nuclei*, 373, 3.

Prieto, M. A. & Fernández-Ontiveros, J. A. (2016). The central parsecs of M87: jet emission and an elusive accretion disc. *Monthly Notices of Royal Astronomy*.

Quataert, E. & Gruzinov, A. (2000). Convection-dominated accretion flows. *The Astrophysical Journal*, 539, 809–814.

Rees, M. J., Begelman, M. C., Blandford, R. D., & Phinney, E. S. (1982). Ion-supported tori and the origin of radio jets. *Nature*, 295(5844), 17–21.

Reimer, A., Protheroe, R. J., & Donea, A. C. (2004). M87 as a misaligned synchrotron-proton blazar. *Astronomy & Astrophysics*, 419(1), 89–98.

Reynolds, C. S. & Nowak, M. A. (2003). Fluorescent iron lines as a probe of astrophysical black hole systems. *Physics Reports*, 377, 389–466.

Rieger, F. M. & Aharonian, F. (2012). Probing the central black hole in M87 with gamma-rays. *Modern Physics Letters A*.

Ross, R. R. & Fabian, A. C. (2007). X-ray reflection in accreting stellar-mass black hole systems. *Monthly Notices of the Royal Astronomical Society*, 381, 1697–1701.

Rusinek, K., Sikora, M., Kozieł-Wierzbowska, D., & Godfrey, L. (2017). On the efficiency of jet production in fr ii radio galaxies and quasars. *Monthly Notices of the Royal Astronomical Society*, 466(2), 2294.

Rybicki, G. B. & Lightman, A. P. (1979). *Radiative Processes in Astrophysics.* Wiley-Interscience, 1 edition.

Ryu, D. & Goodman, J. (1992). Convective instability in differentially rotating disks. *The Astrophysical Journal*, 388, 438–450.

Salpeter, E. E. (1964). Accretion of Interstellar Matter by Massive Objects. *Astrophys. J.*, 140, 796–800.

Seyfert, C. K. (1943). Nuclear Emission in Spiral Nebulae. *The Astrophysical Journal*.

Shakura, N. I. & Sunyaev, R. A. (1973). Black holes in binary systems. Observational appearance. *Astronomy and Astrophysics*, 24, 337–355.

Shapiro, S. L. & Teukolsky, S. A. (1983). *Black Holes, White Dwarfs, and Neutron Stars: The Physics of Compact Objects*. Wiley-VCH.

Slipher, V. M. (1913). The radial velocity of the Andromeda Nebula. *Lowell Observatory Bulletin*.

Stawarz, L. (2010). Radio-Quiet Versus Radio-Loud AGN: What Makes the Difference? *Accretion and Ejection in AGN: a Global View*.

Stone, J. M. & Balbus, S. A. (1996). Angular Momentum Transport in Accretion Disks via Convection. *The Astrophysical Journal*, 464, 364.

Stone, J. M., Pringle, J. E., & Begelman, M. C. (1999). Hydrodynamical non-radiative accretion flows in two dimensions. *Monthly Notices of Royal Astronomy*, 310, 1002–1016.

Thorne, K. S. & MacDonald, D. (1982). Electrodynamics in curved spacetime: 3 + 1 formulation. *Monthly Notices of the Royal Astronomical Society*, 198(2), 339–343.

Thorne, K. S., Price, R. H., & Macdonald, D. A., Eds. (1986). *Black Holes: The Membrane Paradigm*. Yale University Press.

Urry, C. M. & Woo, J.-H. (2002). AGN Black Hole Masses and Bolometric Luminosities. *Astrophysical Journal*, 579, 530–544. 43 p.

Véron-Cetty, M. P. & Véron, P. (2000). The emission line spectrum of active galactic nuclei and the unifying scheme. *The Astronomy and Astrophysics Review*, 10, 81–133.

Wang, J.-M., Li, Y.-R., Wang, J.-C., & Zhang, S. (2008). Spins of the supermassive black hole in m87: New constraints from tev observations. *The Astrophysical Journal Letters*, 676(2), L109.

Wilson, A. S. & Colbert, E. J. M. (1995). The difference between radio-loud and radio-quiet active galaxies. *The Astrophysical Journal*, 438, 62–71.

Woltjer, L. (1959). Emission Nuclei in Galaxies. *The Astrophysical Journal*.

Wright, T. (1750). *An original theory or new hypothesis of the universe : founded upon general phaenomena of the visible creation; and particularly the Via the laws of nature, and solving by mathematical principles*.

Zel'dovich, Y. B. & Novikov, I. D. (1964). *Mass of Quasi-Stellar Objects*. Doklady Akademii Nauk SSSR.

Appendix A

Angular Fits

This appendix contains the fits for Equations 11.9, 11.10, 11.11, and 11.12. The data used to make all of that fits are $M = 10^8 M_\odot$, $M = 10^7 M_\odot$, and $M = 10^6 M_\odot$ holding **B** constant at 10^4 G, U_b at 10^6 ergs/cm^3, and spin at 1; **B** = 10^2 G, **B** = 10^3 G holding M constant at $10^7 M_\odot$, U_b at 10^6 ergs/cm^3, and spin at 1; $U_B = 10^5$ ergs/cm^3 holding M constant at $10^7 M_\odot$, **B** constant at 10^4 G, and spin at 1; spin= 0.1, spin= 0.2, spin= 0.3, spin= 0.4, spin= 0.5, spin= 0.6, spin= 0.7, spin= 0.8, spin= 0.9 holding M constant at $10^7 M_\odot$, **B** constant at 10^4 G, and U_b at 10^6 ergs/cm^3. Figure A.1 shows the normalized half width of the gap versus θ with the fit overlaid on the data. Figure A.2 shows the normalized peak Lorentz factor versus θ with the fit overlaid on the data. Figure A.3 shows the normalized peak electric field versus θ with the fit overlaid on the data. Figure A.4 shows the normalized outgoing energy flux from the up-scattered photons versus θ with the fit overlaid on the data.

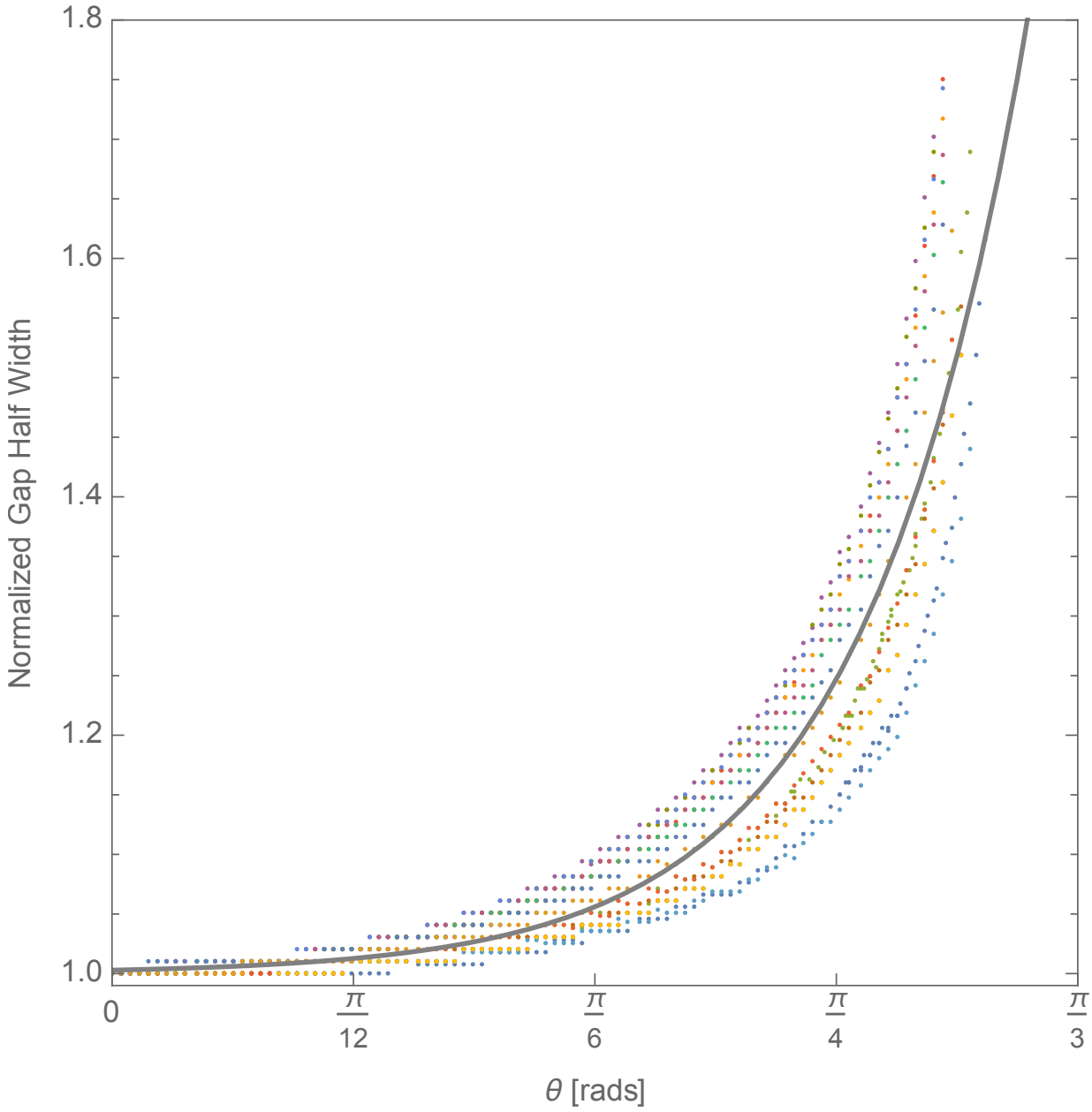

Figure A.1: The exponential fit for the gap half width normalized to 1 at $\theta = 0$ as a function of θ is $2.9\times10^{-3}e^{5.7x}+1$. The data includes $M = 10^8 M_\odot$, $M = 10^7 M_\odot$, and $M = 10^6 M_\odot$ holding **B** constant at 10^4 G, U_b at 10^6 ergs/cm^3, and spin at 1; **B**= 10^2 Ga, **B**= 10^3 G holding M constant at $10^7 M_\odot$, U_b at 10^6 ergs/cm^3, and spin at 1; $U_B = 10^5$ ergs/cm^3 holding M constant at $10^7 M_\odot$, **B** constant at 10^4 G, and spin at 1; spin= 0.1, spin= 0.2, spin= 0.3, spin= 0.4, spin= 0.5, spin= 0.6, spin= 0.7, spin= 0.8, spin= 0.9 holding M constant at $10^7 M_\odot$, **B** constant at 10^4 G, and U_b at 10^6 ergs/cm^3.

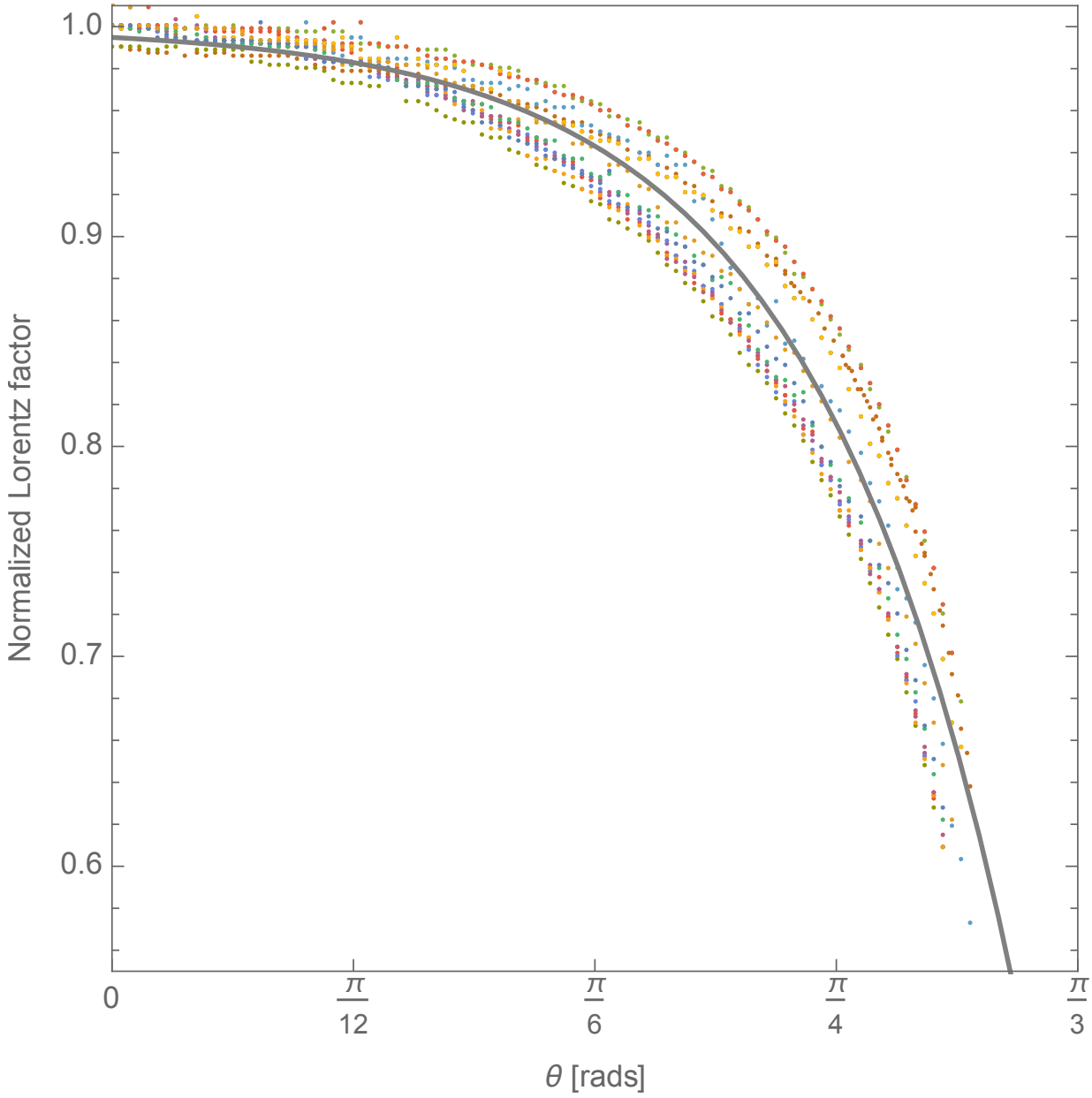

Figure A.2: The exponential fit for the Lorentz factor, normalized to 1 at $\theta = 0$ as a function of θ is $1 - 5.1 \times 10^{-3} e^{4.6\theta}$. The data includes $M = 10^8 M_\odot$, $M = 10^7 M_\odot$, and $M = 10^6 M_\odot$ holding **B** constant at 10^4 G, U_b at 10^6 ergs/cm^3, and spin at 1; **B**= 10^2 Ga, **B**= 10^3 G holding M constant at $10^7 M_\odot$, U_b at 10^6 ergs/cm^3, and spin at 1; $U_B = 10^5$ ergs/cm^3 holding M constant at $10^7 M_\odot$, **B** constant at 10^4 G, and spin at 1; spin= 0.1, spin= 0.2, spin= 0.3, spin= 0.4, spin= 0.5, spin= 0.6, spin= 0.7, spin= 0.8, spin= 0.9 holding M constant at $10^7 M_\odot$, **B** constant at 10^4 G, and U_b at 10^6 ergs/cm^3.

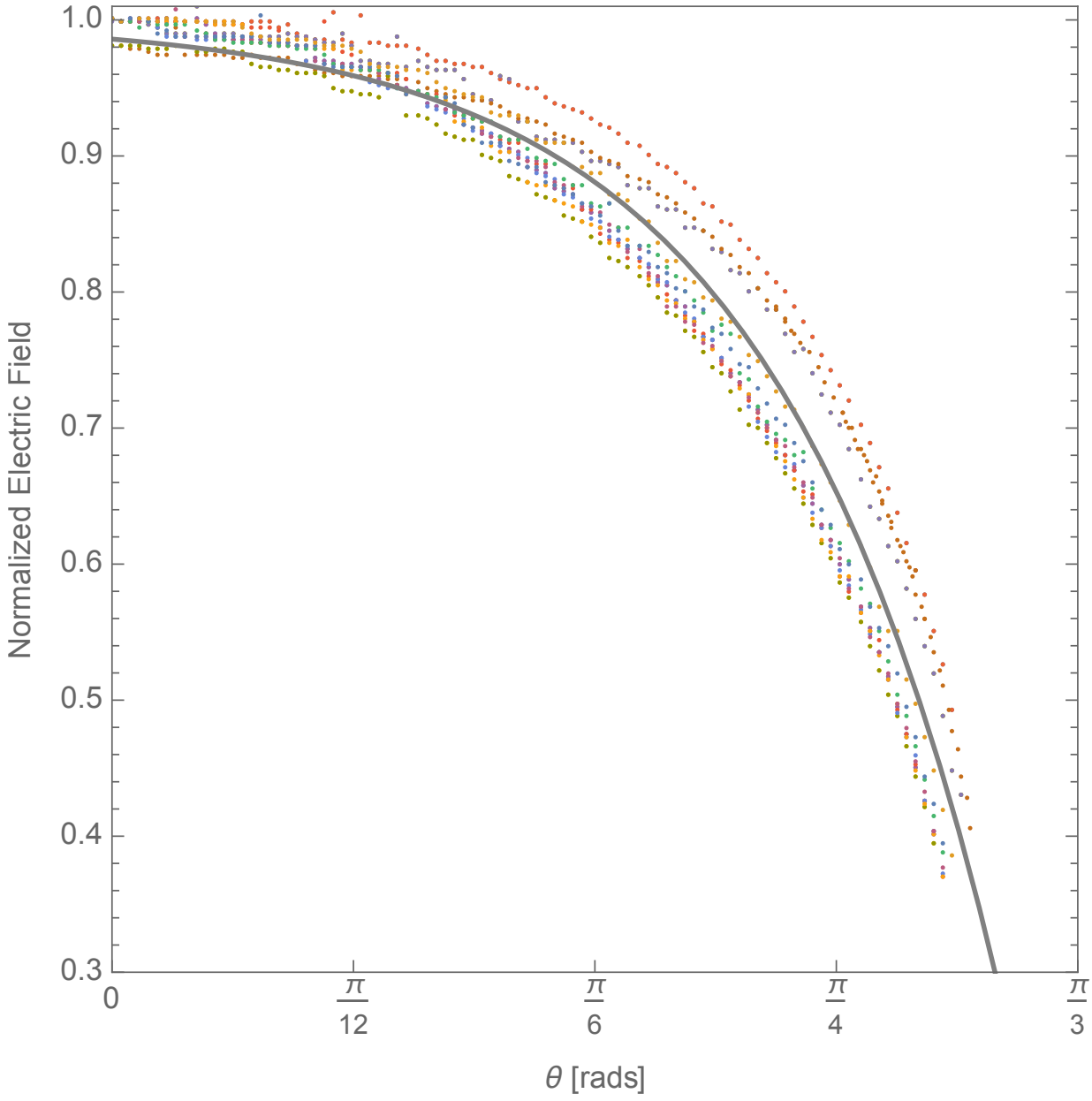

Figure A.3: The exponential fit for the electric field strength, normalized to 1 at $\theta = 0$ as a function of θ is $1 - 0.014e^{4.1\theta}$. The data includes $M = 10^8 M_\odot$, $M = 10^7 M_\odot$, and $M = 10^6 M_\odot$ holding **B** constant at 10^4 G, U_b at 10^6 ergs/cm^3, and spin at 1; **B**= 10^2 Ga, **B**= 10^3 G holding M constant at $10^7 M_\odot$, U_b at 10^6 ergs/cm^3, and spin at 1; $U_B = 10^5$ ergs/cm^3 holding M constant at $10^7 M_\odot$, **B** constant at 10^4 G, and spin at 1; spin= 0.1, spin= 0.2, spin= 0.3, spin= 0.4, spin= 0.5, spin= 0.6, spin= 0.7, spin= 0.8, spin= 0.9 holding M constant at $10^7 M_\odot$, **B** constant at 10^4 G, and U_b at 10^6 ergs/cm^3.

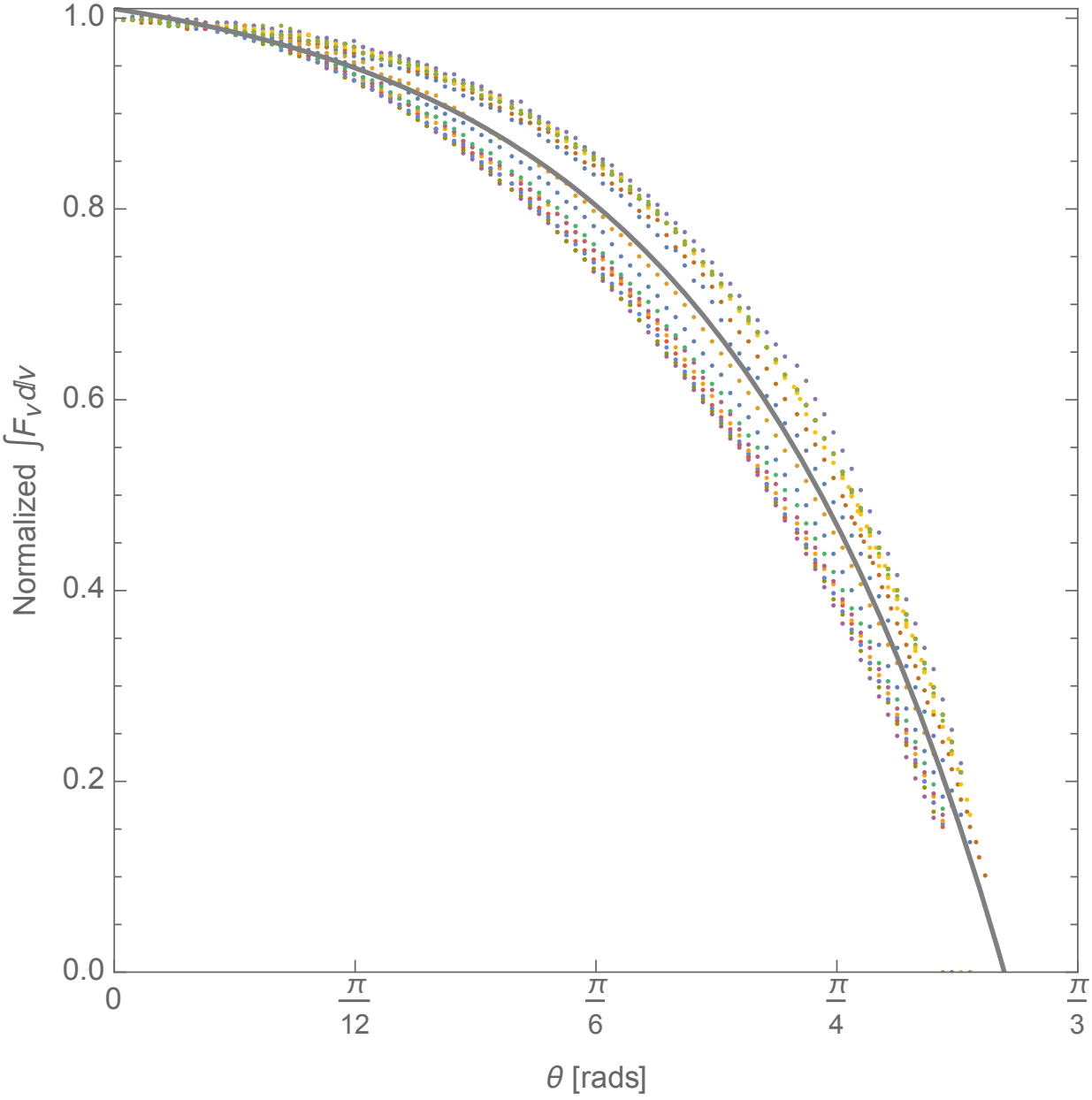

Figure A.4: The exponential fit for the total outgoing energy flux from the up-scattered photons, normalized to 1 at $\theta = 0$ as a function of θ is $1.1 - 0.047e^{3.2\theta}$. The data includes $M = 10^8 M_\odot$, $M = 10^7 M_\odot$, and $M = 10^6 M_\odot$ holding **B** constant at 10^4 G, U_b at 10^6 ergs/cm^3, and spin at 1; **B**= 10^2 Ga, **B**= 10^3 G holding M constant at $10^7 M_\odot$, U_b at 10^6 ergs/cm^3, and spin at 1; $U_B = 10^5$ ergs/cm^3 holding M constant at $10^7 M_\odot$, **B** constant at 10^4 G, and spin at 1; spin= 0.1, spin= 0.2, spin= 0.3, spin= 0.4, spin= 0.5, spin= 0.6, spin= 0.7, spin= 0.8, spin= 0.9 holding M constant at $10^7 M_\odot$, **B** constant at 10^4 G, and U_b at 10^6 ergs/cm^3.

Normalized Parameter	Equation of the Fit
Gap Half Width	$2.9\times10^{-3}e^{5.7\theta}+1$
Peak Lorentz factor	$1-5.1\times10^{-3}e^{4.6\theta}$
Peak Electric Field	$1-0.014e^{4.1\theta}$
Outgoing Photon Flux	$1.1-0.047e^{3.2\theta}$

Table A.1: Fits with respect to polar angle for normalized outgoing spectral energy flux, peak Lorentz factor, peak electric field, and the gap half width.